Synergy of multiple satellite observations in the study of cloud thermodynamics of tropical deep convection

By

Chunpeng Wang

A dissertation submitted in partial fulfillment
of the requirements for the degree of
Doctor of Philosophy
(Atmospheric, Oceanic, and Space Sciences)
In The University of Michigan
2014

Doctoral Committee:

Associate Professor Xianglei Huang, Chair
Assistant Professor Mark G. Flanner
Associate Professor Valeriy Y. Ivanov
Assistant Professor Eric A. Kort
Associate Professor Zhengzhao J. Luo

2014

Acknowledgement

Throughout the years there have been numerous people who have helped bring this thesis to fruition. I am indebted to all the kindly help I received!

I would like to express my heartfelt gratitude to my advisor, Professor Xianglei Huang. It is his support, patience and generosity that guided me to this thesis. Professor Huang has also shown me an excellent example of righteousness and professionalism that would take my lifetime to learn and practice.

I would also like to other thanks to my other dissertation committee members: Professors Johnny Luo, Mark Flanner, Eric Kort, and Ivanov Valeriy for their time to evaluate my research work. I also greatly appreciate Drs. Wei-Kuo Tao, Xiping Zeng for their support and guidance in my research.

A special mention goes to all the friends I have met at the University of Michigan, who have made for many enjoyable experiences both inside and outside the office. I would like to say a thank-you out loud to my friends in AOSS who make my PhD life much more delightful. I would like to give my thanks to the University of Michigan Table Tennis Club who instills me the Michigan sportsmanship and to the University of Michigan Amateur Radio Club where I am encouraged by the genuine pursuit of professionalism.

Last by not least, I would to thank my family. It is their unconditional supports that help me through the trough of my research. It is their happiness that magnifies mine. Without their confidence in me, I wouldn't have been here today. I love you.

Table of Content

List of Figures

Abstract

Tropical convection lies at the heart of atmospheric research, especially for global weather and climate predictions; satellite measurements with large spatial coverage provide valuable information to deepen and broaden our scientific understandings of this subject. This thesis is motivated to utilize satellite measurements with assistance of modeling tools in a synergistic way to study tropical deep convection.

First a generic parallax correction method is proposed to remove the biases resulting from the mismatch of satellite footprints due to different sensor viewing angles targeting the same object. Second a non-blackbody correction is proposed to better estimate cloud top temperature utilizing the vertical structure within the cloud top layer probed by CloudSat and CALIPSO. The distance between the physical cloud top and the effective emission level is shown to have a linear dependence on cloud top fuzziness (CTF; difference between cloud top and 10dBz radar echo) when CTF is less than ~2km. Beyond this threshold, the effective emission level remains 0.74km below the cloud top due to the saturation of IR absorption and emission. This relationship clearly improves simulated MODIS radiances comparing with the observed counterparts.

The distribution of cloud top buoyancy for tropical deep convections derived using cloud top and ambient condition indicates that convective development is sensitive to both land-ocean contrast and diurnal cycle. Under certain assumptions, vertical

velocity inside the convective core is derived and the result is consistent with typical vertical velocity profiles observed by air-bone Doppler radars for tropical deep convections, such as the altitude for the maximum vertical velocity and the existence of a weak detrainment layer in the mid-troposphere.

GCM simulations indicate that overshooting deep convection could be responsible for the vertical transport of black carbon into the stratosphere especially over the India subcontinent during South Asia summer monsoon, and that black carbon in the stratosphere is transported upward at as large as twice the speed of water vapor transport. To explore a possible observational strategy for such injection of black carbon into the stratosphere, a limb-view infrared detection method is proposed based on forward modeling of radiative transfer and the simulated profiles.

Chapter 1

Introduction

Clouds are easily identifiable from the space (Figure 1.1). Its brightness in the visible part of the spectrum leads to effective reflection of solar radiation back to space and its optical thickness gives rise to effective emission and absorption in the infrared part of the spectrum, therefore casting the cloud in a critical role in the climate system. Clouds scatter all over the globe and are apparently morphologically multi-scale: the size of cloud could be ranging from a few kilometers such as an isolated convection to thousands of kilometers such as a squall line or a hurricane. Clouds materialize and dissipate irregularly with time scale spanning from minutes to days, which is governed by the underlying dynamic, microphysics and radiative processes. Such broad spatial and temporal scale span makes the understanding and simulating clouds an intellectually and computationally demanding job. For example, the representation of cloud processes in climate models has long been recognized as the major source of uncertainty in understanding the climate system (e.g., *Cess et al.* [1989] and *Randall et al.* [2003]). With

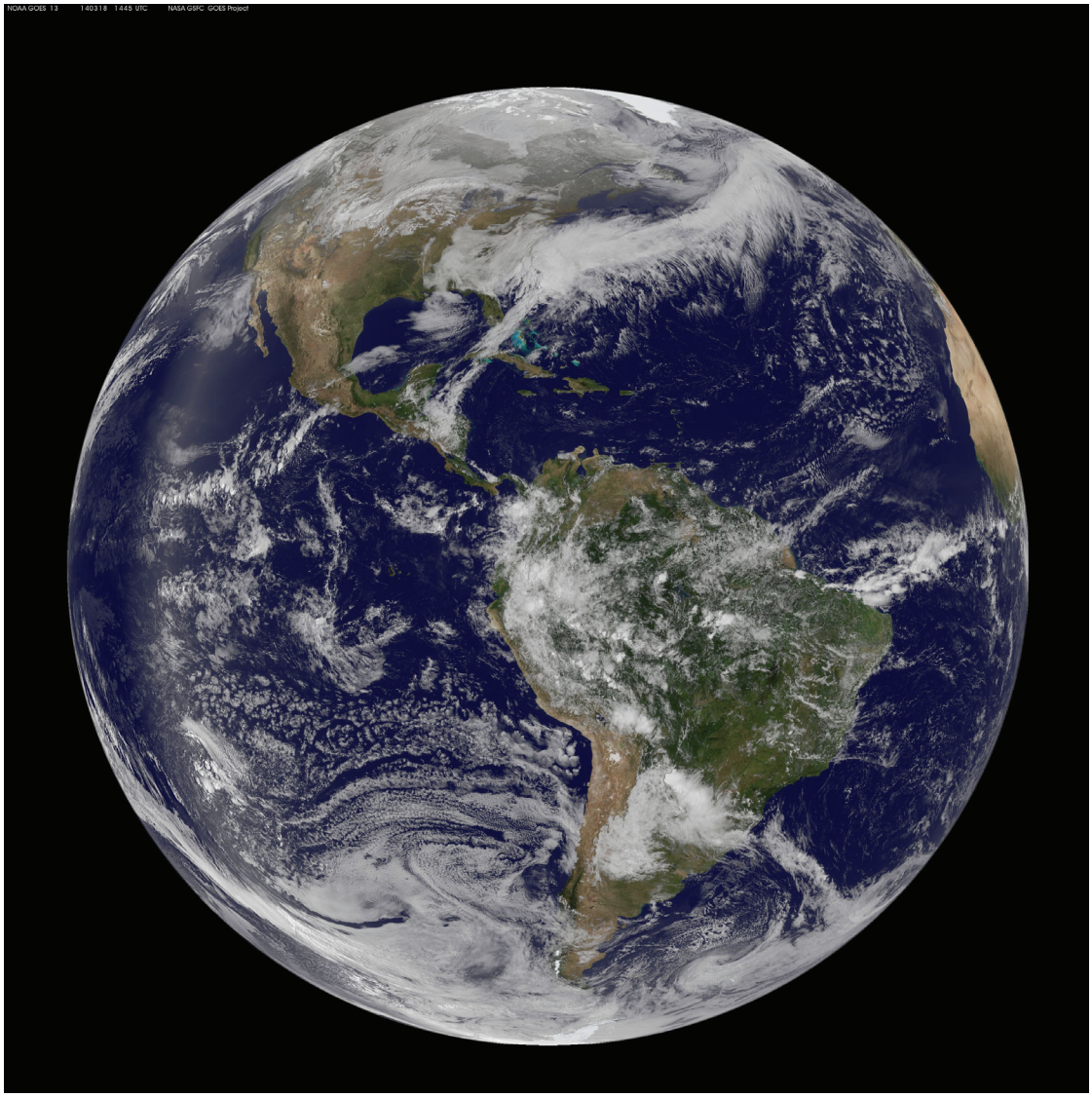

Figure 1.1 Cloud field taken by GEOS-13 satellite on March 18, 2014 1445 UTC overlay on true-color background. The data is available at NASA GSFC GOES Project website (http://goes.gsfc.nasa.gov/).

enormous effort invested into this issue, some of the fundamental details of the microphysical processes are still poorly understood (e.g., mixed-phase cloud) and cloud feedback [*Stephens*, 2005] remains one of the largest sources of uncertainty in climate simulation, undermining the confidence in climate projections.

Faithful representation of cloud process in models relies on accurate cloud parameterization and strong computational power. Recently, cloud-resolving models (CRM) have demonstrated increasing ability in direct parameterization of cloud microphysics, precipitation and aerosol interactions [*Iguchi et al.*, 2012; *Zeng et al.*, 2013], enhancing the understanding of cloud processes [*Ackerman et al.*, 2004; *Fridlind et al.*, 2007]. With growing computational power, there have been attempts to replace the traditional cumulus parameterization in general circulation models (GCMs) with CRMs and the new model configuration is called global CRM (GCRM) [*Tomita et al.*, 2005; *Putman and Suarez*, 2011]. GCRM is run with grid sizes as small as 3.5 km but still cannot simulate long-time climate because of the enormous computational demand. Nevertheless, GCRMs have been shown to perform better than conventional GCMs, for example, in simulating precipitation diurnal cycle [*Sato et al.*, 2009] and summer Asian monsoon [*Oouchi et al.*, 2009].

In the effort of improving model representation of clouds, cloud observation lays the cornerstone for model calibration to ensure maximum consistency between model representations and real clouds. Traditionally, it heavily relies on intensive field campaigns such as the Global Atmospheric Research Program (GARP) Atlantic Tropical Experiment (GATE) in 1974 [*Thompson et al.*, 1979] and the Tropical Ocean Global Atmosphere Coupled Ocean-Atmosphere Research Experiment in 1992-1993 [*Webster & Lukas*, 1992]. However, field campaigns are limited by spatial and temporal coverages and thus can only provide case-by-case datasets rather than a global long-time survey of

cloud behaviors. This is perfectly complemented by satellite measurement by virtue of its global coverage and continuous sampling. In fact, a recent field campaign, the Year of Tropical Convection (YOTC) [*Waliser and Moncrieff*, 2008], has taken advantage of the synergy of field campaign and satellite measurement and has successfully identified major issues in simulating tropical convection and its interactions across space and time scales [*Moncrieff et al.*, 2012].

In this study, A-Train, a state-of-the-art meteorological satellite constellation, is used. A-Train has a series of satellites flying in close formation, providing unprecedented global monitoring of clouds and atmospheric conditions. The wide variety of space-borne instruments onboard different satellites observe the same scene almost simultaneously using multiple remote sensing techniques and different spectral frequency, enabling A-Train to depict the multiple aspects of clouds and the ambient atmosphere. Available since 2006, the A-Train observations offer a large dataset to quantify the statistical characteristics of clouds [*Mace et al.*, 2007; *Sassen et al.*, 2008; *Austin et al.*, 2009] and to assess model performances [*Kay et al.*, 2012].

Driven by the stunning future of unraveling the complexity of cloud, a number of similar studies take advantage of the unique combination of instruments in A-Train and have greatly deepened the insight of cloud fields. For example, vertical profiles of cloud properties are critical for calculating the radiative flux divergence within and at the top of the atmosphere [*Barker et al.*, 2003]. However, multi-layer cloud information generally cannot be retrieved from passive sensor data and would cause biases in cloud top height

retrieval. *Kato et al.* [2010] used active sensors in A-Train, namely, the CloudSat cloud profiling radar [*Stephens et al.*, 2002] and the Cloud-Aerosol Lidar and the Infrared Pathfinder Satellite Observation (CALIPSO) Lidar [*Winker et al.*, 2007] to identify multi-layer cloud top and base heights and has derived a relationship that can be used to estimate the influence caused by cloud fraction, uppermost cloud top, and cloud thickness vertical profile differences.

Previous studies using space-borne infrared imagers (such as MODIS) had difficulties in distinguishing different kinds of clouds (like cumulus clouds and thick stratus cloud) because optically thick cloud with similar cloud top heights tend to have very similar brightness temperatures in the IR window region. *Luo et al.* [2008; 2009] demonstrated the idea that cloud inner structure profiled by CloudSat radar can be used to study cloud development. Similarly, *Posselt et al.* [2008] illustrates that CloudSat's measurement of cloud internal structure greatly benefits the research of cyclones and contributes to numerical model assessment.

This research is motivated to synergistically use multiple satellite data sets and focuses on the behavior of tropical convection.

Convection is a strong upward motion usually from the planetary boundary layer up. From the perspective of atmospheric thermodynamics, it is the consequence of unstable atmosphere and can be further sustained by the release of latent heat. The induced updraft continuously pumps moist air from the boundary layer, which feeds the diabatic heating and fuels the updraft. During the updraft process, water droplets begin to

freeze at 0^{o}C. However, freezing is not instantaneous and water may remain in liquid form beyond freezing level (at ~6 km with temperature of 0^{o}C). Therefore, some of the convection reaching the freezing level may not glaciate fast enough to sustain upward motion and then stop at the mid-troposphere. Deep convections are the strongest portion of convection with cloud tops near the tropopause with strong precipitation and large amount of water transported to the mid- and upper-troposphere [*Johnson et al.*, 1999; *Cotton et al.*, 2010].

During the developing phase of convection, cloud condensates are continuously pumped up to the cloud top by strong updraft. When the updraft is not strong enough to hold the large amount of condensates, downdraft gradually dominates and large condensates precipitate out leaving only tenuous cloud near the top. Therefore, the life cycle of convections could be derived from the cloud top condition. This research is thus motivated to use cloud top features to illustrate the statistical development pattern of tropical convection. Satellite measurements play a key role in this study due to their direct measurement of cloud top radiative features and continuous global sampling. Using correctly collocated multiple satellite data, reanalysis data, cloud resolving models and global climate models, and the state-of-the-art radiative transfer models, this research strives to address the following questions:

1. What is the optimal way to blend satellite observations? What insights could cloud radar and lidar provide to the study of convection?
2. How cloud top buoyancy can tell us about convective development?

3. Overshooting deep convection is responsible for the transport of black carbon to the stratosphere. How to possibly observe such events using remote sensing techniques?

The rest chapters in this thesis are organized as follows. Chapter 2 shows that parallax error is critical for the studies of tropical convection using satellite data and proposes a general solution for the parallax correction of all kinds of sensors on different platforms. Chapter 3 takes advantage of the CloudSat's unique probing ability to look inside cloud and constructs a relationship between the inner-structure of cloud top layer and the physical cloud top temperature. Chapter 4 analyzes the derived cloud top buoyancy dataset and illustrates the statistical pattern of convective development. Vertically composited cloud top buoyancy is then used to estimate the updraft velocity of convection, the gross features of which agree reasonably well with field measurements. Chapter 5 studies the transport of black carbon by overshooting deep convection and proposes a method to retrieve stratospheric black carbon. The thesis is briefly summarized in Chapter 6 along with proposed future work.

References:

Ackerman, A. S., M. P. Kirkpatrick, D. E. Stevens, and O. B. Toon (2004), The impact of humidity above stratiform clouds on indirect aerosol climate forcing, *Nature*, 432, 1014–1017.

Austin, R. T., A. J. Heymsfield, and G. L. Stephens (2009), Retrieval of ice cloud microphysical parameters using the CloudSat millimeter-wave radar and temperature, *J. Geophys. Res.*, 114, D00A23.

Barker, H. W., et al. (2003), Assessing 1D atmospheric solar radiative transfer models: interpretation and handling of unresolved clouds, *J. Clim.*, 16, 2676–2699.

Cess, R.D., et al. (1989), Interpretation of cloud-climate feedback as produced by 14 atmospheric general-circulation models, *Science*, 245, 513-516.

Cotton, W. R., G. Bryan, and S. C. van den Heever (2010), *Storm and Cloud Dynamics*, 820 pp., Academic Press, San Diego, Calif.Dufresne, J.-L., and S. Bony (2008), An assessment of the primary sources of spread of global warming estimates from coupled atmosphere-ocean models, *J. Clim.*, 21, 5135–5144.

Fridlind, A. M., et al. (2007), Ice properties of single-layer stratocumulus during the Mixed-Phase Arctic Cloud Experiment: 2. Model results, *J. Geophys. Res.*, 112, D24202.

Iguchi, T., T. Nakajima, A. P. Khain, K. Saito, T. Takemura, H. Okamoto, T. Nishizawa, and W.-K. Tao (2012), Evaluation of cloud microphysics simulated using a meso-scale model coupled with a spectral bin microphysical scheme through comparison with observation data by ship-borne Doppler and space-borne W-band radars, *J. Atmos. Sci.*, 69, 2566-2586.

Johnson, Richard H., Thomas M. Rickenbach, Steven A. Rutledge, Paul E. Ciesielski, Wayne H. Schubert (1999), Trimodal Characteristics of Tropical Convection, *J. Climate*, 12, 2397–2418.

Kato, S., S. Sun-Mack, W. F. Miller, F. G. Rose, Y. Chen, P. Minnis, and B. A. Wielicki (2010), Relationships among cloud occurrence frequency, overlap, and effective thickness derived from CALIPSO and CloudSat merged cloud vertical profiles, *J. Geophys. Res.*, 115, D00H28.

Kay, J. E., et al. (2012), Exposing Global Cloud Biases in the Community Atmosphere Model (CAM) Using Satellite Observations and Their Corresponding Instrument Simulators, *J. Climate*, 25, 5190–5207.

Luo, Z., G. Y. Liu, and G. L. Stephens (2008), CloudSat adding new insight into tropical

penetrating convection, *Geophys. Res. Letts.*, 35, L19819.

Luo, Z., G. Y. Liu, G. L. Stephens, and R. H. Johnson (2009), Terminal Vs transient cumulus congestus: A CloudSat perspective, *Geophys. Res. Letts.*, 36, L05808, doi:10.1029/2008GL036927.

Mace, G. G., R. Marchand, Q. Zhang, and G. Stephens (2007), Global hydrometeor occurrence as observed by CloudSat: Initial observations from summer 2006, *Geophys. Res. Lett.*, 34, L09808.

Moncrieff, M. W., D. E. Waliser, M. J. Miller, M. A. Shapiro, G. R. Asrar, J. Caughey (2012), Multiscale Convective Organization and the YOTC Virtual Global Field Campaign, *Bull. Amer. Meteor. Soc.*, 93, 1171–1187.

Oouchi, K., A. T. Noda, M. Satoh, B. Wang, S. P. Xie, H. G. Takahashi, and T. Yasunari, (2009), Asian summer monsoon simulated by a global cloud-system-resolving model: Diurnal to intra-seasonal variability, *Geophys. Res. Lett.*, 36, L11815.

Posselt, D. J., G. L. Stephens, M. Miller (2008), CLOUDSAT: Adding a New Dimension to a Classical View of Extratropical Cyclones, Bull. Amer. Meteor. Soc., 89, 599–609.

Putman, W. M., and M. Suarez (2011), Cloud-system resolving simulations with the NASA Goddard Earth Observing System global atmospheric model (GEOS-5), *Geophys. Res. Lett.*, 38, L16809.

Randall, D., M. Khairoutdinov, A. Arakawa, and W. Grabowski (2003), Breaking the cloud parameterization deadlock, *Bull. Am. Meteor. Soc.*, 84, 1547–1564.

Sassen, K., Z. Wang, and D. Liu (2008), Global distribution of cirrus clouds from CloudSat/Cloud-Aerosol Lidar and Infrared Pathfinder Satellite Observations (CALIPSO) measurements, *J. Geophys. Res.*, 113, D00A12.

Sato, T., H. Miura, M. Satoh, Y. N. Takayabu, and Y. Q. Wang (2009), Diurnal cycle of precipitation in the Tropics simulated in a global cloud-resolving model, *J. Clim.*, 22, 4809–4826.

Stephens, G. L., et al. (2002), The CloudSat mission and A-Train, *Bull. Am. Meteorol. Soc.*, 83, 1771–1790.

Stephens, Graeme L. (2005), Cloud Feedbacks in the Climate System: A Critical Review, *J. Climate*, 18, 237–273.

Thompson, R. M., S. W. Payne, E. E. Recker, and R. J. Reed (1979), Structure and properties of synoptic-scale wave disturbances in the intertropical convergence zone

of the eastern Atlantic, *J. Atmos. Sci.*, 36, 53-72.

Tomita, H., H. Miura, S. Iga, T. Nasuno, and M. Satoh (2005), A global cloud-resolvingsimulation: Preliminary results from an aqua planet experiment, *Geophys. Res. Lett.*, 32, L08805.

Waliser, D. and M. Moncrieff (2008), Year of Tropical Convection (YOTC): The YOTC Science Plan, A Joint WCRP – WWRP/THORPEX International Initiative, WMO/TD-No.1452; WCRP-130; WWRP/THORPEX- No. 9, 34.

Webster, P. J., and R. Lukas (1992), TOGA COARE: the Coupled Ocean-Atmosphere Response Experiment, *Bull. Amer. Meteor. Soc.*, 73, 1377-1416.

Winker, D. M., W. H. Hunt, and M. J. McGill (2007), Initial performance assessment of CALIOP, *Geophys. Res. Lett.*, 34, L19803.

Zeng, Xiping, Wei-Kuo Tao, Scott W. Powell, Robert A. Houze, Paul Ciesielski, Nick Guy, Harold Pierce, Toshihisa Matsui (2013), A Comparison of the Water Budgets between Clouds from AMMA and TWP-ICE, *J. Atmos. Sci.*, 70, 487–503.

Chapter 2

Parallax Correction in the Analysis of Multiple Satellite Data Sets

The material of this chapter was published in

Wang, C.P., Z. Luo, X.L. Huang (2011), Parallax Correction in Collocating CloudSat and MODIS Observations: Method and Application to Convection Study, *JGR-Atmospheres*, 116, D17201, doi:10.1029/2011JD016097.

Wang, C.P. and X.L. Huang (2014), Parallax Correction in the Analysis of Multiple Satellite Data Sets, *Geoscience and Remote Sensing Letters*, 11(5), 965-969, doi:10.1109/LGRS.2013.2283573.

2.1 Introduction

With the accumulation of A-Train satellite data [*Stephens et al.*, 2002] that observe various components of the climate system in a nearly simultaneous way, more and more studies have been conducted to exploit the synergistic value among these different measurements. Clouds are one of the primary interests for A-Train satellite

measurements given their central role in the weather and climate system. A number of instruments have been deployed on the A-Train constellation for this purpose including two active sensors (CloudSat and CALIPSO) and a suite of passive sensors (e.g., MODIS, AIRS, TES, and MLS). Several recent studies have exploited such synergy to gain new insights into cloud structure, climatology and the underlying physical/chemical processes using satellites that not only fly in close formation [e.g., *Kahn et al.*, 2008; *Luo et al.*, 2008, 2009, 2010; *Kato et al.*, 2010; *Hong et al.*, 2010; *Martin et al.*, 2013] but also in different kinds of orbits whose ground tracks intersect regularly, like CloudSat & TRMM (Tropical Rainfall Measuring Mission) [*Liu et al.*, 2008]. The virtue of this technique is

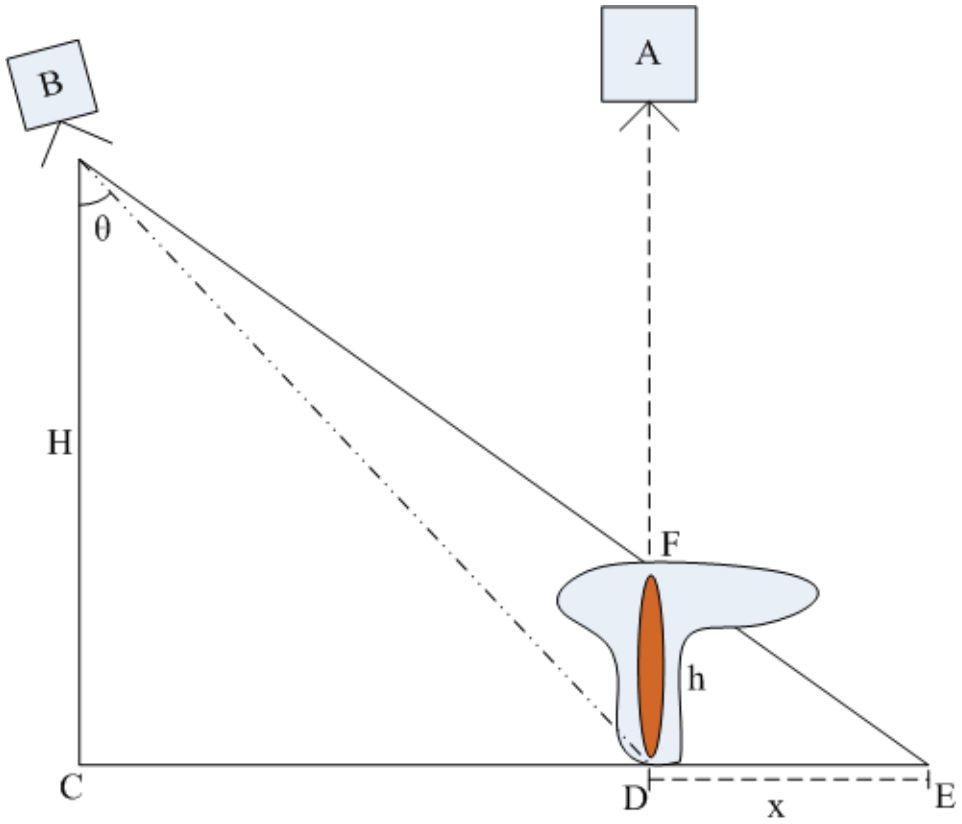

Figure 2.1. A schematic showing the viewing geometries of two satellites to illustrate the parallax problem. Note this drawing is for illustration only so horizontal and vertical dimensions are not in scale.

that a collection of variables could be constructed for an object using a variety of observing methods, which cannot be done by a single satellite. In a series of studies, *Luo et al.* [2008, 2009, 2010] utilized CloudSat radar reflectivity, MODIS 11-μm brightness temperature (hereafter, 11-μm BT) and ambient temperature from ECMWF operational analysis to estimate the buoyancy of convective clouds, identify life stages in their whole life cycles, as well as to estimate the entrainment rates. *Kahn et al.* [2008] analyzed CloudSat and CALIPSO data to evaluate the accuracy of AIRS cloud retrievals for a wide range of cloud types and to quantify the biases and variability of cloud top height retrieved by AIRS operational algorithm as a function of cloud types.

However, in practice when dealing with satellite Level-1 & 2 swath measurements and retrievals, the parallax issue as the result of non-zero sensor viewing angle arises when multiple satellite data sets are used to study the same object at high elevation from different viewing angles. Level-3 & 4 products have variables mapped onto uniform space-time grid scales and the geolocation information of the footprints is not preserved so they are not considered in this study. A-Train constellation is designed to simplify the collocation problem by flying satellites in close formation. Therefore, a common approach for collocation is to simply ensure that the ground footprints of the two sensors match each other (this method has been used in producing the MODIS-AUX product, which matches each CloudSat profile with 3×5 grids of 1-km MODIS data centered on the CloudSat profile location). This issue may not be relevant for researchers when the target object is physically uniform over relatively large spatial scales compared with the size of satellite footprints (e.g., stratus covering hundreds of square kilometers) or when the satellite footprint is large enough that the parallax shift is within one

footprint; however, in the case that the viewing zenith angle is large, for example, 55^{o} for AMSR-E (the Advanced Microwave Scanning Radiometer for the Earth Observing System), or that the target spans only over a narrow horizontal scale (e.g., a convective plume or cumulus cloud with a horizontal width of several kilometers), or that the target is elevated in high altitude (e.g., cloud tops of tropical deep convection & polar stratospheric clouds), the corresponding error may not be trivial and could significantly affect the physical interpretation of the measurements.

To avoid introducing incorrect information into data fusion analyses, a parallax correction as a function of satellite viewing geometries and object heights should be specifically addressed. Figure 2.1 uses a sketch to illustrate this problem: instrument A observes the cloud in a nadir view with the ground footprint centered at point D while instrument B observes the same cloud top (centered point F) from a slantwise path with ground footprint centered at point E. If simply collocating the ground footprint, a different measurement from instrument B (the dash-dotting line in Figure 2.1) will be used whose viewing path does not intersect the cloud at all. Therefore, to ensure exact collocation in cloud observations, a shift in ground footprints for instrument B is required (in this case, it would be from point D to point E). This shift is hereafter called parallax correction. The parallax problem can also be exploited to retrieve useful information about clouds. For example, the stereoscopic technique that is often used to retrieve cloud top height [e.g., *Hasler*, 1981; *Diner et al.*, 1998] is based on the same parallax principle as illustrated in Figure 2.1.

Parallax issue is often encountered in the studies of convective clouds. *Nagle and Holz* [2009] and *Schreier et al.* [2010] describe the radiance agreement in infrared

brightness temperatures and show that when using a more rigorous spatial response, the variability and skewness in the agreement are significantly reduced; essentially, the parallax correction here improves the agreement further for heterogeneous cloud scenes observed from multiple platforms, especially for deep convection.

Consider now another example of using CloudSat and MODIS (aboard Aqua) to study convective clouds. CloudSat observes clouds in a nadir view while MODIS operates in cross-track scanning mode with zenith angle from -65^{o} to 65^{o}. Because both satellites are part of the A-Train constellation, they fly at an altitude ~700 km. The ground trajectories of the two satellites, however, are ~230 km apart in the tropics and cross over each other in Polar Regions. This situation is illustrated in Figure 2.1, with satellite A as CloudSat and satellite B as MODIS. In generating MODIS-AUX (a standard CloudSat data product), the collocation is done by matching the positions of CloudSat surface footprints with those of MODIS. As pointed out in the previous paragraph, such collocation strategy could introduce a parallax bias. To further illustrate this problem, Figure 2.2 shows a segment of CloudSat radar reflectivity (the upper panel) and its ground track (yellow line in the lower panel) overlapped with MODIS 11-μm BT. Each red dot represents a MODIS footprint corresponding to a CloudSat profile. Note that for computationally efficiency, only deep convective clouds are used for calculation so that there are only three red dots that lie away from the CloudSat ground footprint and that the parallax shift of a lower cloud could be anywhere between the red dots and the CloudSat track. For the convective plume between (126.70 ºE, 3.70 ºN) and (126.75 ºE, 3.89 ºN), if parallax error is not corrected, the "collocated" MODIS 11-μm BT is 272.3 K which poses a stark contrast with the cloud top height (CTH) at 15.18 km as measured by

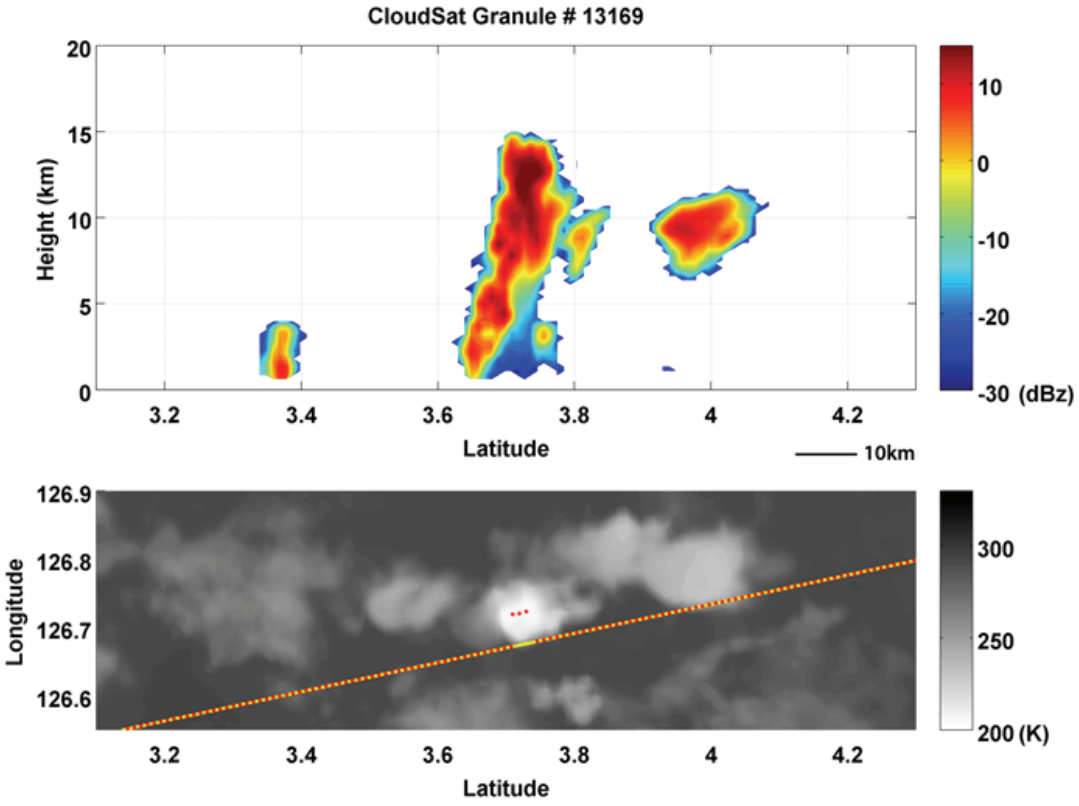

Figure 2.2 (Upper panel) CloudSat radar reflectivity (in dBz) observed at 17:21UTC on October 18, 2008. (Lower panel) Concurrent measurements of MODIS 11μm brightness temperature (BT, in kelvin). The yellow line is CloudSat ground track without parallax correction. The red dotted line segment represents the parallax correction.

CloudSat cloud profiling radar. According to ECMWF interim reanalysis [*Simmons et al.*, 2006; *Uppala et al.*, 2008], the ambient temperature at 15.18 km at this location was only 201.67 K. This considerable temperature contrast is clearly non-physical as the blackbody temperature of the cloud top should be close to the ambient condition. Meanwhile, Figure 2.2 indicates that the parallax displacement, although very small (~5 km), shifts the matched points from the edge to the center of the convective plume. Convective edge usually consists of thin cirrus anvil which allows a significant amount of the warm radiation from below the cloud deck to leak through resulting in a much higher

11-μm BT. When parallax correction is applied to this plume (red dots in the lower panel of Figure 2.2), the corresponding MODIS 11-μm BT for this tall and narrow convective tower becomes 206.3 K, significantly lower than the one without parallax correction and is in line with the ambient temperature at this height. This example is a good illustration and the statistical significance of the parallax correction will be discussed in section 2.4.

This parallax problem has been realized in previous studies by *Luo et al.* [2009, 2010]. Their tentative solution was to remove the smaller convective plumes by imposing a condition that the standard deviation of the 11-μm BT over neighboring MODIS pixels be less than 3 K for CTH within 3~9 km and less than 1 K for CTH above 12 km. Such a stringent condition effectively filtered out scenes with non-uniform cloud tops and retained only those with relatively flat cloud tops (which we call "flat-top" condition hereafter), making parallax correction less of an issue. However, the selected samples under this condition will favor convective clouds at the mature and dissipative stages when plumes cease to grow but flatten out to form anvils, and will tend to exclude those in the incipient stage whose cloud tops are still "irregular". Since convective clouds in the incipient stage tend to have positive buoyancy near the cloud top, such a constraint can inadvertently affect the statistics related to convective top buoyancy, such as those shown in *Luo et al.* [2009; 2010]. Moreover, the microphysics of convective cloud top is distinct at different stages and exclusion of developing convection would intrinsically undermine the sampling strategy and final conclusion.

The objective of this study is to introduce a general solution to the parallax issue and to apply the method to two case studies: one is the parallax correction of CloudSat and MODIS, and the other one is the parallax correction of CloudSat and AMSR-E.

Additionally, we evaluate the impact of parallax correction on statistics collected about convective clouds and compare the results with *Luo et al.* [2009; 2010]. The rest of the section is organized as follows: section 2.2 describes the data sets and algorithm for parallax correction; some case studies are also presented. Statistical results and comparisons with analysis without parallax correction are presented in section 2.3. Discussion and conclusion are given in section 2.4.

2.2 Data description and methodology

2.2.1 CloudSat , MODIS, AMSR-E

Launched in 2006 as part of the A-Train constellation, CloudSat is a Sun-synchronous polar-orbiting satellite flying at the altitude of 705 km [*Stephens et al.*, 2002]; it carries a 94-GHz nadir-viewing Cloud Profiling Radar (CPR) with a vertical resolution of 480 m oversampled to 240 m and ground footprint of approximately 1.7 km along track and 1.3 km cross track. Unlike ground-based weather radars that use centimeter wavelengths to detect raindrop-size particles, CloudSat CPR is working at wavelength of 3 mm (94 GHz in frequency) and is able to detect the cloud hydrometeors of much smaller sizes. This frequency is the optimum compromise to maximize cloud detection because that the amount of power received by CPR is strongly influenced by the cloud reflectivity and atmospheric attenuation, that cloud reflectivity increases with increasing radar frequency, and that atmospheric attenuation becomes prohibitive at higher frequencies.

CloudSat plays a unique role in cloud study as its radar signal can penetrate cloud and profile the inner structure of cloud. This allow us to define convection morphologically which is more physically sound than solely using brightness temperature

in either IR and microwave band. Because the latter only indicates the path-integrated radiance, it may suffer from wrong identification of multi-layer cloud and non-convective thick cloud. CPR has limited sampling ability as it can only probe the atmospheric column nadir to the satellite.

In this study, CloudSat standard profile 2B-GEOPROF is used for cloud mask and radar reflectivity. Cloud mask is a parameter ranging from 0 to 40 assigned to each pixel. The value of zero indicates no cloud detected and increasing value increasing likelihood of cloud detected. The threshold of 10 is applied to filter out unconfident cloud detection with a lower probability of false detection. Radar reflectivity in the units of dBz indicates the amount of water content that reflects the radar signal. Specifics of the CloudSat mission and data products can be found in a recent publication by *Stephens et al.* [2008] and CloudSat Data Processing Center (www.cloudsat.cira.colostate.edu).

The moderate resolution imaging Spectroradiometer (MODIS) onboard Aqua satellite is a key instrument of the Earth Observing System (EOS). It was launched in 2002 and measures narrowband radiances in 36 spectral bands from 0.415 to 14.24 μm with wavelength-dependent nadir spatial resolutions of 250 m-1 km [*Barnes et al.*, 1998; *Parkinson*, 2003; *Platnick et al.*, 2003]. The collection of frequencies allows for a wealth of data product concerning land, cryosphere, ocean, and atmosphere, which paves the way for its wide application in the atmospheric science community. In this study, we specifically use 11-μm BT, a direct measurement of MODIS. The Bandwidth is from 10.78 to 11.28 μm with noise equivalent temperature of 0.05 K. This frequency is one of the most transparent channel in the atmospheric window region, and is least affected by the absorbing gases and therefore most sensitive to the cloud mass.

The advanced microwave scanning radiometer – EOS (AMSR-E) is one of the six sensors aboard Aqua satellite. AMSR-E provides passive measurements of microwave brightness temperatures 6 frequencies ranging from 6.9 to 89.0 GHz with independent horizontal and vertical polarization measurement at each frequency. Operating at the altitude of 705 km, it measures the upwelling scene BT over an angular sector of $\pm 61^{o}$ about the sub-satellite track, resulting in a swath width of 1445 km. The half cone angle at which the reflector is fixed is 47.4^{o} which result in an Earth incidence angle of 55.0^{o}. It is often used to retrieve parameters such as precipitation rate and cloud water content [*Nesbitt et al.*, 2000] partially because *Spencer* [1986] introduced a correction method that leads to a strong correlation between polarization corrected microwave BT and raining rate. BT in difference frequencies gives information of cloud water content at different regions of cloud. High frequencies like 89.0 GHz are sensitive to cloud top and lower frequencies like 10.65 GHz are sensitive to cloud bottom. As a conclusion, AMSR-E could greatly contribute to the understanding of precipitation features of convective study.

2.2.2 Selection of convective clouds

We analyze all data collected within the tropics (30°S-30°N) during the entire year of 2008. Following *Luo et al.* [2009], CloudSat reflectivity profiles are used to obtain CTH while MODIS imageries of 11-μm BT are used to estimate cloud top temperature (CTT). Shallow convection is not the center of our interest and there are technological difficulties in using such an approach to study shallow convection, such as misidentification of low cloud by CloudSat and a higher likelihood of contamination in 11-μm BT by overlying sub-visible thin cloud. Moreover, the parallax correction for

shallow convective cloud can be smaller than 1km (refer to Section 2.3.4 for a discussion on this), i.e., within the same MODIS 1-km pixel. Meanwhile, convections penetrating the tropical tropopause are rare and we are only interested in overall statistics. Therefore, we limit our analysis to CTH between 6 km and 18 km. The corresponding geolocation coordinates, solar zenith angle and sensor viewing geometry of each MODIS 1-km pixel are extracted from the MODIS/Aqua 1km 5-minute wide swath along CloudSat, normally known as MAC03S1.002 product. The ambient temperature is obtained from temporal interpolation of six-hourly ECMWF interim reanalysis temperature fields. ECMWF interim is the latest reanalysis product by ECMWF [*Simmons et al.*, 2006; *Uppala et al.*, 2008] with a horizontal resolution of 1.5°×1.5°.

For cloud decks, it is believed that 11-μm BT represents approximately the temperature at an emission level where cloud IR optical thickness ($\Delta\tau_{cld}$=1) is about one. This statement is to be evaluated in Chapter 3. So, 11-μm BT is always warmer than the CTT (except for some cases of overshooting to the stratosphere). *Luo et al.* [2010] utilized collocated CALIPSO lidar and CloudSat radar data to estimate the correction for 11-μm BT case by case. Here, the empirical relationship from Chapter 3 is adopted and a justification will be provided later. The basic idea is to link the CloudSat fuzziness to the level where 11-μm IR emission weighting function peaks. The idea is that a "packed" cloud top (which will show up as a larger vertical gradient in radar reflectivity) needs a smaller correction because the emission level is close to the physical cloud top whereas a fuzzy cloud top needs a larger correction. This correction distance is the multiplied by local moist adiabatic lapse rate, the product of which is then deducted from 11-μm BT, leading to the CTT estimate. Once CTT is determined, convective buoyancy is derived

from the difference between CTT and ambient temperature at the same altitude, as is done in *Luo et al.* [2010].

Another modification to *Luo et al.* [2010] is the way statistics is constructed. In *Luo et al.* [2010], each selected CloudSat convective profile is counted equally in calculating the histogram of buoyancy. But since larger convective clouds contain more radar profiles, the statistics may be biased in favor of larger systems. Here instead, we treat each convective cloud (defined as neighboring CloudSat profiles satisfying the "convective core" condition as defined in *Luo et al.* [2010]) as one entity and use the highest CTH to define buoyancy for the whole plume in an effort to use the profile closer to the convective core. Sometimes a separate layer of cirrus can be seen on top of a convective plume. We exclude such cases since the upper cirrus layer affects the MODIS 11-μm BT and makes it a difficult task to calculate the corresponding CTT for the convective tower.

2.2.3 Parallax correction

Consider Figure 2.1: assume instrument A is the CloudSat Cloud profiling radar (CPR) and instrument B is MODIS aboard Aqua. In order to match the cloud observation in the field of view, the ground footprint of MODIS should be at point E. Given the similarity of triangle BCE and triangle FDE and the MODIS viewing zenith angle at point D, i.e. $\angle CBD$), the length of the displacement vector from point D to point E, $\vec{r}$, can be written as

$$\left|\vec{r}\right| = hH\tan\theta/(H-h) \sim h\tan\theta \qquad (2.1)$$

where H is the operational altitude of satellite sensor B; θ denotes the viewing zenith angle of sensor B with ground footprint at point D; h is the CTH derived from satellite A (thus h<<H). The direction of $\vec{r}$ is given by viewing azimuth angle (φ), defined as the angle between vector $\overrightarrow{DC}$ and local geodetic north [*Nishihama et al.*, 1997].

Denote the latitude and longitude of point D as Y_D and X_D, respectively. Then the latitude and longitude of point E can be written as

$$Y_E = Y_D + \left|\vec{r}\right| \cos\phi / R_E \tag{2.2}$$

$$X_E = X_D + \left|\vec{r}\right| \sin\phi / (R_E \cos Y_D) \tag{2.3}$$

where all angles and coordinates are in radians and R_E is the radius of the Earth (~6371 km).

For some of the satellite data products, the sensor viewing azimuth angle is not given. In such case, spherical trigonometry can be used to calculate the viewing azimuth angle. The minor arc of a great circle between two points (for example, A and B) on a great circle of a sphere can be expressed as

$$\widehat{AB} = arc\cos(\sin Y_A \sin Y_B + \cos Y_A \cos Y_B \cos(X_A - X_B)) \tag{2.4}$$

The overhead arc over two letters is used to denote this distance hereafter. Figure 2.3 is an illustration of the plan view for Figure 2.1. The two arrows indicate the tracks of satellite A and B. The circle at D is the cloud to be sampled and C is the sub-satellite point of satellite B, whose three adjacent swaths are shown by three thick dashed lines.

Point G is the intersection between the satellite track and the swath where the cloud is identified. $\Delta\phi$ is the viewing angle that deviates from the bearing of the satellite

(ϕ_0; moving direction east of the geodetic north; $\widehat{CG}$ in this case for satellite B). Using the cosine rule of the angles on a sphere, we have,

$$\cos\widehat{GD} = \cos\widehat{CG}\cos\widehat{CD} + \sin\widehat{CG}\sin\widehat{CD}\cos\Delta\phi \tag{2.5}$$

Then, we obtain,

$$\Delta\phi = \arccos\left(\frac{\cos\widehat{GD} - \cos\widehat{CG}\cos\widehat{CD}}{\sin\widehat{CG}\sin\widehat{CD}}\right) \tag{2.6}$$

The bearing of a satellite's trajectory (from C to G) relative to geometric North is obtained following that

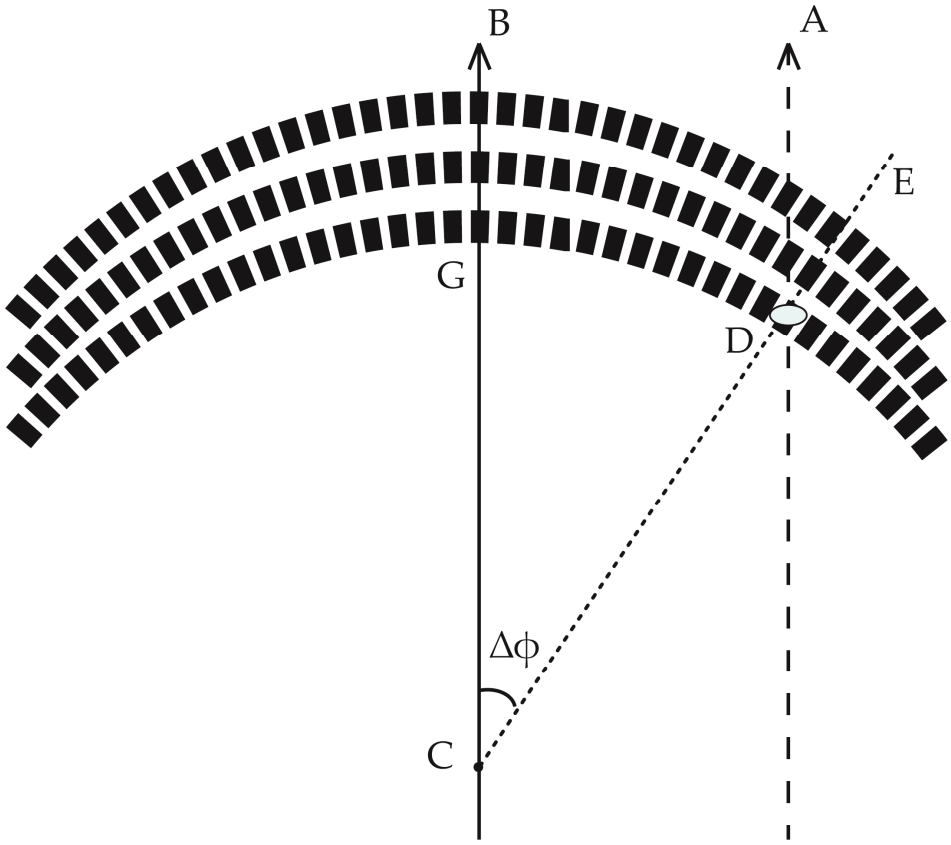

Figure 2.3 Three swaths of markers denote the ground footprints of satellite B whose ground track is CG. The dash line denotes the ground track of satellite A. The deviation of viewing zenith angle ($\Delta\phi$) is calculated based on the location of ground footprint and the cloud object is identified at point D.

$$\phi_0 = \arctan 2[\sin(\mathrm{X}_G - \mathrm{X}_C)\cos \mathrm{Y}_G, \cos \mathrm{Y}_C \sin \mathrm{Y}_G - \sin \mathrm{Y}_C \cos \mathrm{Y}_G \cos(\mathrm{X}_G - \mathrm{X}_C)], \phi_0 \in (-\pi, \pi] \tag{2.7}$$

where $\arctan 2(\mathrm{y}, \mathrm{x})$ is a function that returns the angle between east and the point (x, y), which is measured clockwise. This function is available in many programming languages.

Thus, the viewing azimuth angle from satellite sensor is,

$$\phi = \phi_0 \pm \Delta\phi \tag{2.8}$$

The plus-minus sign is determined by the relative position of two satellite tracks. For the ascending-node example depicted in Figure 2.3, $\phi = \phi_0 + \Delta\phi$ applies. For its descending-node case, $\phi = \phi_0 - \Delta\phi$ would apply.

The effect of the non-spherical shape of the Earth is neglected in this study given the flattening factor of the Earth being around (a-b)/a=1/298 where a and b are equatorial and polar radii, respectively. For instance, take the polar orbit satellites of A-Train. Assuming a spherical Earth has a radius of actual polar radius, and then arcs on the great circle are approximately elongated by at most a factor of 1/298. Let $x = \widehat{CG} / 298$ in radians, given that $\widehat{CG}$ and $\widehat{CD}$ are approximately equal, we rewrite Equation 2.5, do the expansion, and only keep the first-order terms of x since x<<$\widehat{CG}$. Then we have,

$$\Delta\phi = \arccos\left(\frac{\cos\widehat{GD} - \cos^2\widehat{CG} + \cos 2\widehat{CG} \cdot x}{\sin^2\widehat{CG} + \cos 2\widehat{CG} \cdot x}\right) \tag{2.9}$$

For a $\widehat{CG}$ ~7.6 degrees, the influence of a non-spherical Earth assumption contributes about 1.2% relative error to the azimuth angle calculation. For a parallax shift

of 5 km, the corresponding difference is 60 meters, which is much smaller than actual size of the satellite footprints that we consider here.

2.3 Case studies

We illustrate the usage of the general solutions derived in Section 2.2 with two examples related to cloud remote sensing, both drawn from the A-Train constellation observations.

2.3.1 CloudSat and MODIS

For this case study, the CloudSat overpass is collocated with MODIS MAC03S1.002 products acquired from the NASA Goddard Earth Sciences Data and Information Services Center (GES DISC). This product is the subset of MODIS/Aqua dataset along CloudSat track with swath width of 200 km. For the sake of computational efficiency, this product is used instead of the standard MODIS Level-1 product. The sensor viewing geometry of each MODIS 1-km pixel is given in terms of the viewing azimuth angle, which is the direction from the target object to the sensor (equivalently, $\overrightarrow{DC}$ in Figure 2.1). To be consistent with the aforementioned definition of sensor azimuth angle (ϕ), π is added to ϕ in order to obtain the angle between vector $\overrightarrow{DC}$ and local geodetic north. Then we have,

$$Y_E = Y_D + \left|\vec{r}\right| \cos(\phi + \pi) / \mathrm{R}_E \tag{2.10}$$

$$X_E = X_D + \left|\vec{r}\right| \sin(\phi + \pi) / (\mathrm{R}_E \cos \mathrm{Y}_D) \tag{2.11}$$

We present two cases to further illustrate the parallax problem. The first case has been briefly discussed in the introduction section (Figure 2.2). The convective cloud is located near 3.7°N and 126.7°E: red dots represent points E in Figure 2.1 (with parallax correction) and yellow dots correspond to points D (without parallax correction). The shift from the yellow dots to the red dots is about 5.1 km, however resulting in a change of 11-μm BT by 66 K (from 272 K to 206 K)! Such a large temperature gradient is also reflected in a large standard deviation of 25 K for the 11-μm BT from the 3×5 grids of 1-km MODIS data centered on the CloudSat profile location. Clearly, parallax correction is

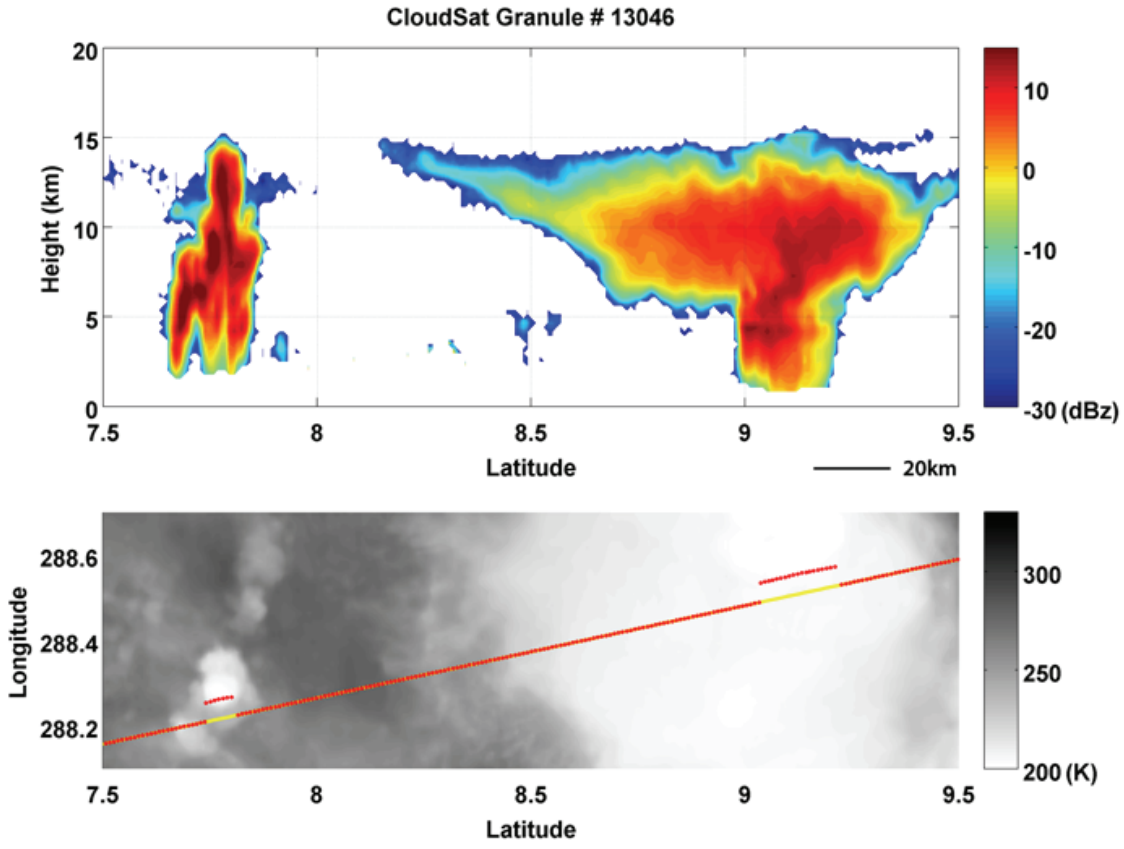

Figure 2.4. Similar to Figure 2.2 except for the observations made at 06:37 UTC on Oct 10, 2008.

critical for the correct estimation of CTT associated with this convective plume.

Another example is shown in Figure 2.4 wherein two convective clouds are identified: one is an isolated deep convection (~7.8°N and 288.3°E) and the other is a much larger convective system (~9.1°N and 288.4°E). The former case is just like the one in Figure 2.2 – an isolated, small scale, and vigorous deep convection. Small parallax shift translates to a large difference in the 11-μm BT (~30 K). The latter case, in contrast, possesses some very different characteristics such as having a well-defined anvil cloud extending over 100 km, as shown in the vertical cross section of CloudSat radar reflectivity. Most likely it is a convective system at its mature stage or perhaps even heading toward dissipation (once the plume rains out the precipitating particles). The anvil is rather "flat" and homogeneous as the standard deviations of the 3×5 11-μm BT measurements surrounding the convective cores are only about 0.28 K. Parallax correction makes little difference to this case, as far as CTT is concerned. It should be noted that the former case, i.e., the small deep convective plume, would have been filtered out if the "flat-top" criteria in *Luo et al.* [2010] were used but the latter case will remain.

These cases help illustrate the scenarios where parallax correction will make a difference (smaller systems) and where it will not (larger systems with a flat top). The next section focuses on statistical analysis (based on tens of thousands of cases) to examine the effects of parallax correction on estimation of CTT and convective buoyancy, as well as how these effects depend on cloud height, cloud size, etc.

2.3.2 CloudSat and AMSR-E

Knowing that the half cone angle (47.4°) at which the reflector is fixed and the Earth incidence angle (55.0°), the length of $\widehat{CG}$ on the great circle can be computed and is ~7.6°. Since $\Delta\phi$ is small (~11°) and shape of the swath is close to part of a circle, we assume $\widehat{CG}$ and $\widehat{CD}$ are of the same length. Then we have,

$$\Delta\phi = \arccos\left(\frac{\cos\widehat{GD} - \cos^2\widehat{CG}}{\sin^2\widehat{CG}}\right) \tag{2.12}$$

Only the 89GHz brightness temperature is considered here because of its fine spatial resolution and its high sensitivity to small ice particles near the cloud top. The gray scale color contour in Figure 2.5 shows the AMSR-E horizontally polarized 89GHz

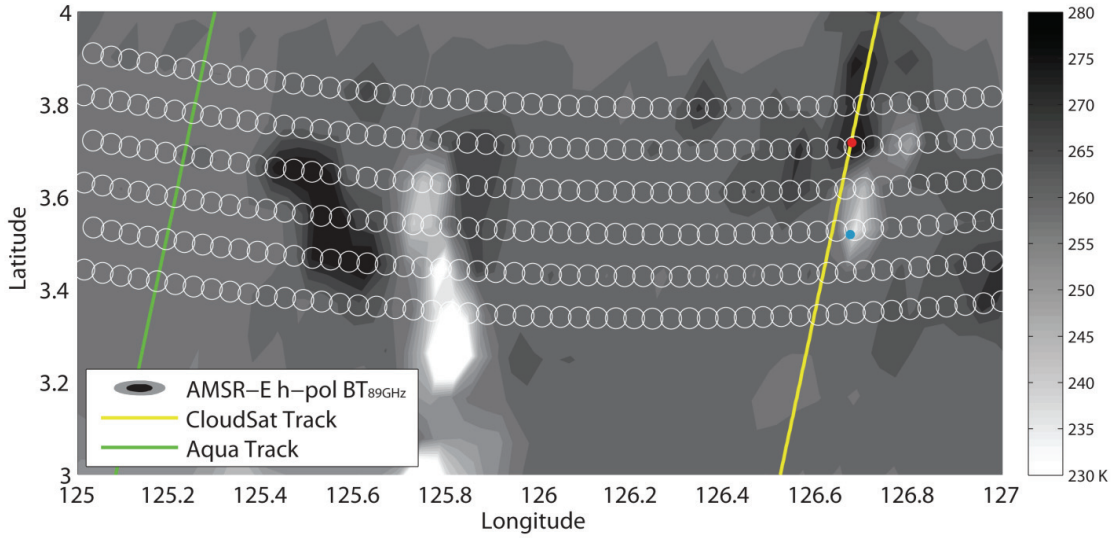

Figure 2.5. The gray scale map shows the same scene as in Figure 2.4 but with the AMSR-E horizontal-polarized 89GHz BT. Six swaths of AMSR-E footprints are marked with white circles for illustration use. The yellow and green lines show the ground tracks of CloudSat and Aqua satellites, respectively. The red dot represents a profile of CloudSat measurement of the same convective cloud in Figure 2.4. With parallax correction applied, the blue dot shows the location of the actual BT from the cloud top.

brightness temperature collocated for the same case shown in Figure 2.4. The green line is the AMSR-E ground track which is later used to get the satellite local bearing. Similar to Figure 2.4, the CloudSat track is plotted in yellow and the red dot shows the location of the same convective cloud. This snapshot was taken in a descending node when the satellites were flying from the North Pole to the equator. Figure 2.4 clearly demonstrates that CloudSat and AMSR-E aboard Aqua are flying in two close orbits[1]. Spatial separation between the two orbits reaches its maximum over the equator and minimum near the pole [*Savtchenko et al.*, 2008]. As shown in the figure, ϕ equals the satellite bearing minus $\Delta\phi$. Then, the displacement vector is projected onto latitude and longitude coordinates and marked with a blue dot, which can help locate the correct AMSR-E measurement that should be used. Though the instantaneous field of view (IFOV) of AMSR-E at 89GHz band (4km×6km, cross and along track, respectively) is much larger than that of MODIS (1km×1km), the large viewing zenith angle of AMSR-E leads to a parallax error difference that is non-negligible. The nearest AMSR-E 89GHz BT measurements decrease from 285 K at the red dot to 237 K at the blue one with a decrease of 48 K.

2.3.3 When nadir-view satellite is not available

It should be noted that, as for parallax corrections for cloud remote sensing, cloud top height is a prerequisite for solutions described in Section 2.2. These case studies use the CloudSat to provide such estimates of cloud top height. Other cloud top height estimation methods such as CO_2 slicing are equally applicable. Additionally, when nadir-

[1] CloudSat has experienced an orbit shift in 2001 and 2012 due to a significant battery degradatio n since April 2011. Details can be found at [*Witkowski et al.*, 2012].

viewing satellites are absent and when the cloud top is located by its radiative feature, the actual latitude and longitude coordinates of the cloud would need to be derived by inversely using the parallax correction solution in Section 2.2 (i.e., obtaining coordinates of X_D and Y_D based on known values of X_E and Y_E). One notable application is the study of clouds in the polar region [*Chan et al.*, 2013; *Key et al.*, 2003]. Sun-synchronous satellites overpass the polar region and provide a dense sampling pattern over the Polar Regions. The nature of sun-synchronous satellite determines that measurements from different viewing directions and large viewing zenith angles [*Chan et al.*, 2013] will be collocated. The rotation of the Earth would not complicate the issue significantly unless the time interval between two satellite observations is very large. Due to the nature of satellite polar overpasses, different satellites view the object from different directions. The different viewing directions are already considered in our equations as the parallax shift will be projected along the viewing direction.

2.3.4 Applicability of parallax correction

As mentioned above, such parallax correction is most noticeable for targets in high elevations and in narrow horizontal widths. In studies such as remote sensing of surface conditions (e.g., surface temperature, soil moisture) or near-surface conditions (e.g., boundary layer conditions, shallow convective clouds), simple collocation by ground footprints would be sufficient for almost all the cases.

Another consideration is the size of satellite footprint. Still using Figure 2.1 for illustration, if satellite sensor B has a footprint which is large enough to encompass both points D and E, and the cloud top is homogeneous enough, then no parallax correction is needed. To generalize the discussion, let a and b denote the length of a satellite footprint

along and across a swath. Then parallax correction is only needed when $\left|\vec{r}\right| > L = \sqrt{ab}$, where L is the mean spatial resolution. As an example, for the footprint of AMSR-E 89GHz measurements, a = 4 km and b = 6 km thus L_{89GHz} is 4.9 km. Take the case in Section 3 for an example, the parallax correction shift for the convective cloud (~21.4 km) is over four times of L_{89GHz}. In contrast, $L_{23.8GHz}$ (~23.6 km) outnumbers the parallax shift, which means parallax correction for this channel is unnecessary.

At a given spatial resolution, the minimum elevation of target that needs parallax correction is $L / \tan\theta$. No parallax correction is needed when the cloud top height is below this level since the corrected viewing angle still falls into the same IFOV. For AMSR-E 89GHz channel, this threshold is 3.4 km, which warrants the necessity of parallax correction for this channel as long as the convective cloud top height is above this level. In comparison, the threshold becomes 16.5 km for its 23.8GHz channel, an elevation that few convective cloud tops can reach.

2.4 Results and Interpretations

Following the method described in Section 2.2, 16,218 convective clouds are identified from CloudSat data over the tropics (30°S-30°N) for the entire year of 2008. Herein, the influence of parallax correction to deep convection studies is illustrated through the statistical relations between CloudSat CTH and MODIS 11-μm BT before and after the correction. For clouds of our interests, i.e., single deep-convective cloud cell, its 11-μm BT is well correlated with its physical cloud top temperature. Meanwhile, temperature change with altitude is nearly linear. Therefore, a good linear relation between CloudSat CTH and MODIS 11-μm BT can be expected when a large size of

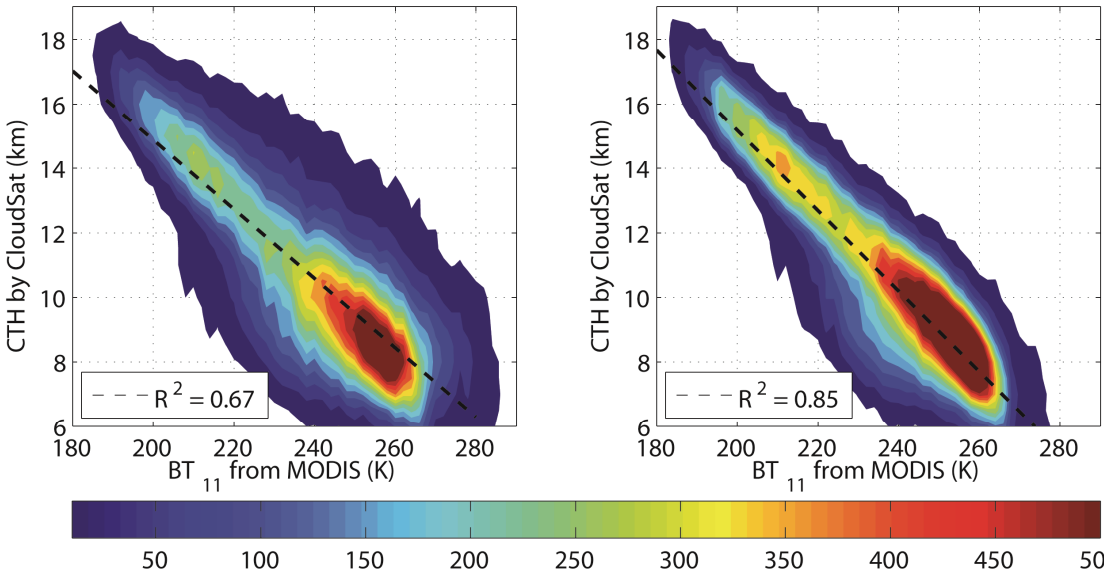

Figure 2.6. Left panel: the 2-D histogram of collocated CloudSat CTH and MODIS 11-μm BT before the parallax correction. Only convective cloud cases are selected according to the criteria used in Section 2.2.2. The R-square is labeled. Right panel: same as the left one after the parallax correction.

such cases are examined. Figure 2.6 shows two 2-D histograms of CloudSat CTH and MODIS 11-μm BT with an identical set of contour colors, one before the parallax correction and one after it. It is obvious that the parallax correction significantly reduces the spread of the 2-D histogram and yet only modestly changes the peaks of the histograms. It improves the correlation between CloudSat CTH and MODIS 11-μm BT from 0.82 to 0.92 (i.e., R-square from 0.67 to 0.85).

Figure 2.7 shows the mean MODIS 11-μm BT as well as the standard deviation as a function of CTH. Two curves are shown: one with parallax correction (blue) and the other without (red). The bin size for CTH is 1 km. Several findings deserve discussion.

1) *The mean BT values become smaller after the parallax correction* (the blue curve is consistently lower than the red curve). This can be understood as follows: some

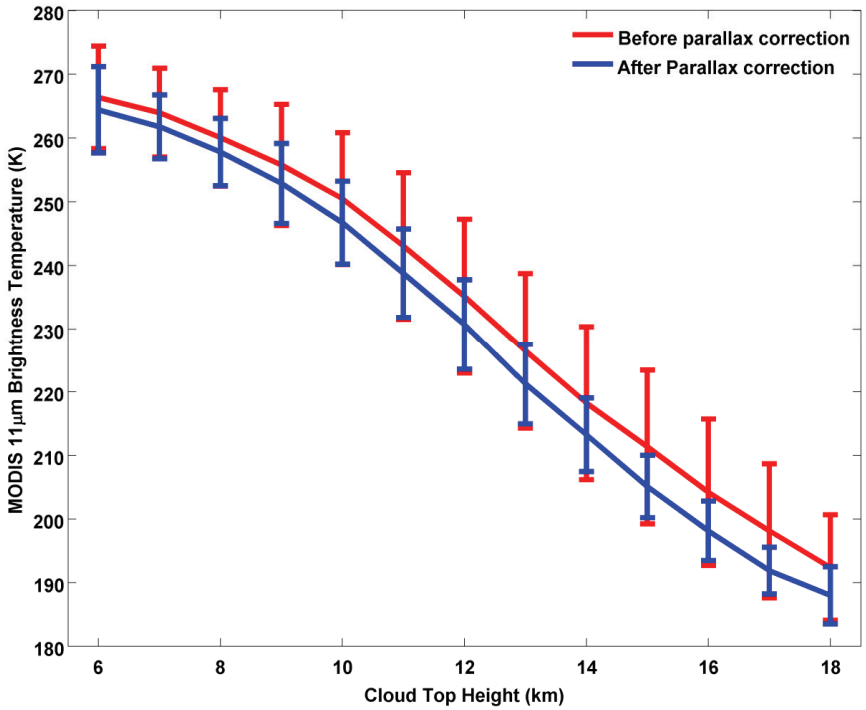

Figure 2.7. Mean and standard deviation of MODIS 11-μm BT as a function of cloud top height (CTH). A total of 16,218 cases over the year of 2008 are used to compute the statistics. The bin size of CTH is 1km. Red and blue lines show the results before and after the parallax correction, respectively.

of the BT reading without parallax correction includes the contribution from both convective plume and atmospheric layers or surface below it as demonstrated in Figure 2.2. It is most likely that the neighborhood of the convective plume consists of clouds with lower height and warmer BT, or even clear-sky scenes, since convective plumes usually bulge out from the cloud deck (our selection of the highest-reaching CloudSat profile as the representative CTH for each convective cloud also contributes to this difference). Figure 2.7 also shows that the parallax-induced difference in BT increases with CTH. For example, the mean values differ by 2 K at CTH of 7 km and it increases to 7.2 K at 15 km. This is because the surrounding of a taller convective plume is less likely

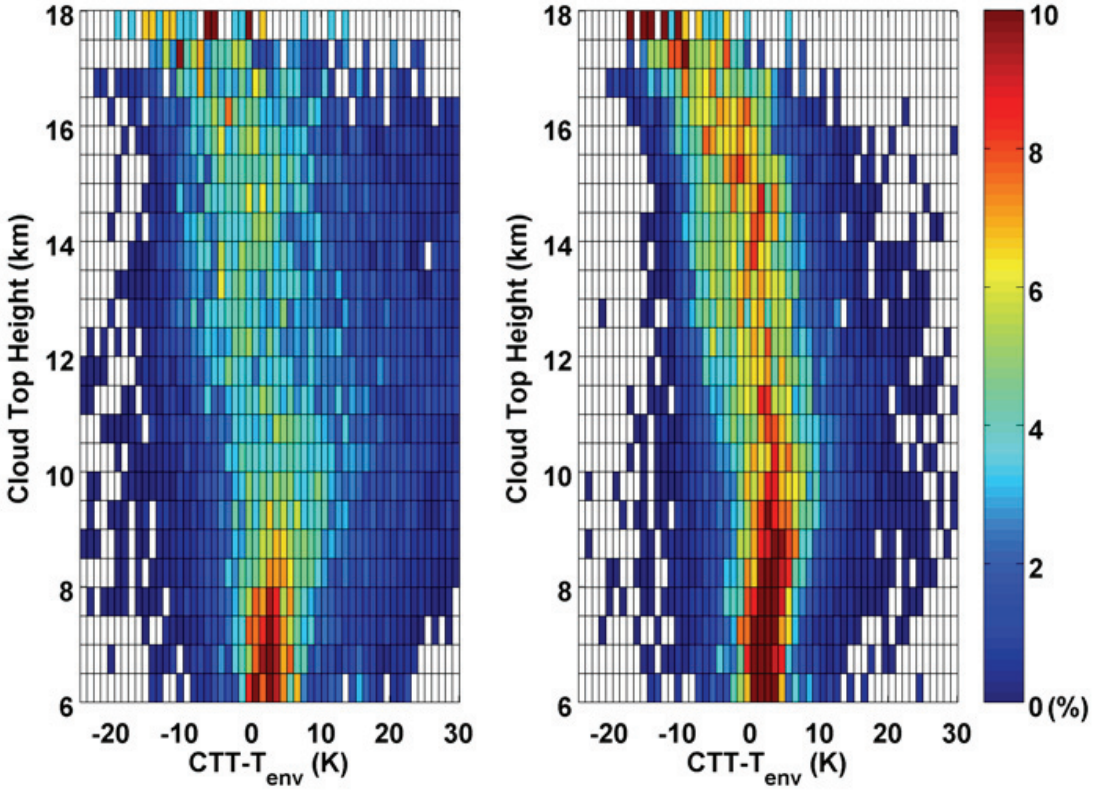

Figure 2.8. Histograms of $\Delta T \equiv CTT - T_{env}$ as a function of CTH (2-D histogram). Left and right panels are results from before and after parallax correction, respectively. The bin size of CTH is 0.5km and that of CTT-T_{env} is 1K. The histograms are normalized at each CTH interval so that the total occurrence adds up to 100% at each CTH level.

to be colder and higher than the plume itself (e.g., it is more likely for a 7-km convective plume to be sandwiched by taller neighbors than a 15-km plume). Therefore, BT without parallax correction tends to come from a scene warmer than the convective plume (as illustrated in Figures 2.2 and 2.4).

2) *The standard deviations of the BT after the parallax correction are consistently smaller than those before the correction*. Such a reduced spread can be understood as reflecting an overall improved collocation of CTH (from CloudSat) and BT (from

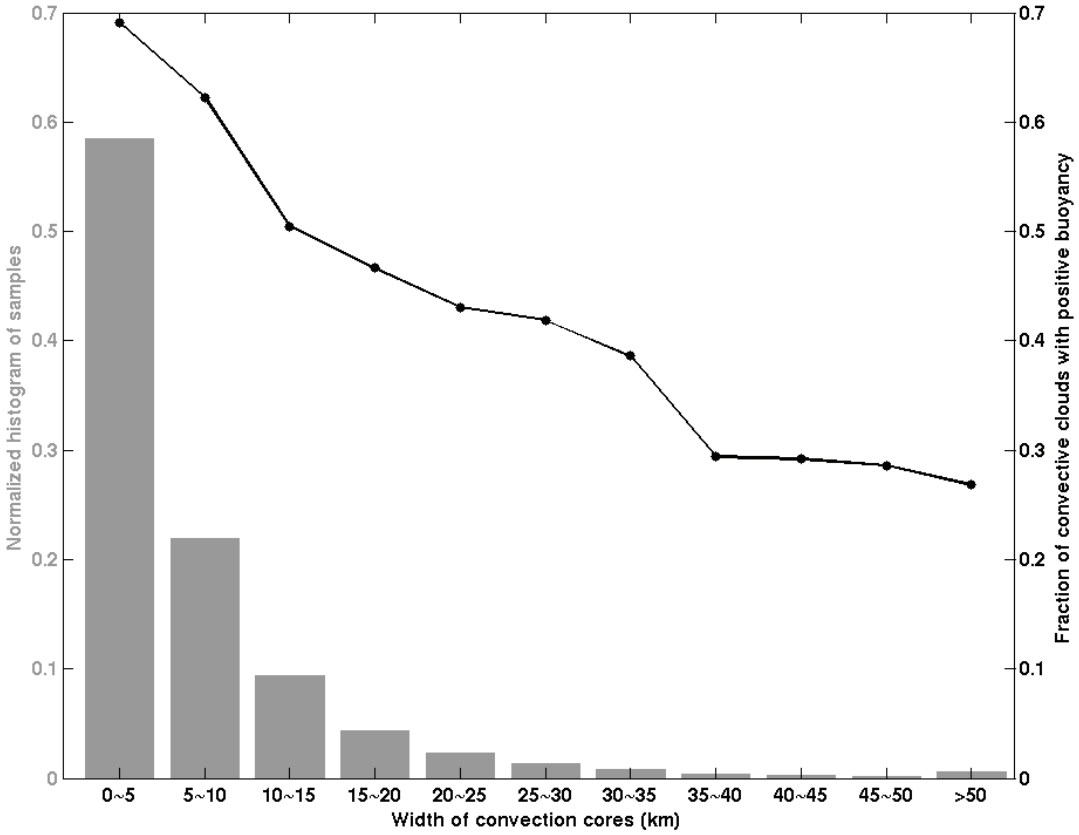

Figure 2.9. The black curve shows the fraction of convective clouds with positive buoyancy sorted by horizontal span of the core of convective cloud as observed by CloudSat. The gray bar is the normalized number of observations falling into each bin of horizontal span. Normalization is with respect to the total number of observations.

MODIS). In other words, the estimated BT is now more closely clustered around the "true" value for that height level (e.g., no more 272.3 K for 15.18 km, as shown in Figure 2.2). The decrease in spread is more pronounced for taller convection than for lower one. Together with (1), these changes suggest that parallax correction is particularly important for studying deep convection.

After MODIS 11-μm BT is converted to CTT, we calculate the difference between CTT and the ambient temperature (T_{env}) obtained from ECMWF reanalysis data: $\Delta T \equiv CTT - T_{env}$, which is used in *Luo et al.* [2010] as an indicator of convective

buoyancy. Our focus is again placed on contrasting the statistics before and after parallax correction. Figure 2.8 shows the histograms of ΔT as a function of CTH (2-D histograms). The histograms are normalized at each CTH interval so that the total occurrence adds up to 100% at each CTH level. Consistent with the 11-μm BT statistics in Figure 2.7, the histogram before parallax correction shows a larger spread than that after the correction, especially for CTH > 8km. Figure 2.8 also shows that, for the cases with CTH above 12 km, negative buoyancy is dominant. This is consistent with the fact that 12 km happens to correspond to the mean level of neutral buoyancy (LNB) for the tropics as estimated from the Air Force Laboratory reference tropical profile [*Ellingson et al.*, 1991]; convection ascending beyond the LNB will likely have colder top than the environment, thus negative buoyancy.

In addition to examining the statistics at different cloud top heights, it is also informative to composite the positive buoyancy statistics with respect to the horizontal size of the core of a convective cloud as observed by the CloudSat radar reflectivity. One cautious note is that the horizontal size deduced from CloudSat may be somewhat different from the real size as inferred from geostationary imageries which are capable of capturing a plan view of the entire convective systems. Results are shown in Figure 2.9 in terms of the fraction of convective clouds with positive buoyancy sorted by the horizontal span of these clouds. Generally, the fraction of positive-buoyancy cases decreases with the size of connective core (Figure 2.2). So does the mean of temperature difference between cloud top and ambient environment (not shown here), which drops from 2.8 K for the 0-5km bin to -3.4 K for the 35-40km bin. These results suggest that smaller convective plumes are more likely to be actively growing (positive buoyancy).

This is consistent with our understanding of the convective life cycle and with previous studies (see, for example, *Luo et al.* [2008]). The positive-buoyancy fraction levels off after ~ 35 km. As shown by the histogram on the same figure, the number of cases with horizontal span >35 km only consist of 1.39% of total observations. Moreover, such large convective core occupies a considerable portion of the 1.5º×1.5º grid box. Hence it might not be a good approximation any more to assume the ERA-interim temperature of that grid box being the cloud-free ambient temperature. Therefore, such level off beyond 35km may not be statistically robust.

2.5. Conclusion

Parallax problem affects collocation of satellite measurements from different platforms. This problem is especially pronounced for cloud observations. Here, we describe a parallax correction method for collocating CloudSat and MODIS data for the study of tropical convective clouds. The impact of the parallax correction on the statistics of convective cloud properties, such as cloud-top temperature (CTT) and buoyancy, is examined. Comparisons are also made with previous studies of tropical convection using the same data sets that avoided the parallax problem by imposing a "flat-top" condition on selection of convective clouds. Although effectively avoiding the parallax problem, the "flat-top" condition biases the statistics toward convection at mature or dissipating stages when convective plumes tend to flatten out to form cirrus anvils. Analysis of a whole year (2008) of data is conducted over the tropical region (30°S-30°N). The main findings are summarized as follows:

1) *Parallax correction reduces the CTT of convective clouds; the magnitude of the reduction increases with cloud-top height (CTH).* This is because without parallax

correction, the satellite views the surrounding area of a convective plume which is likely to be warmer than the plume (to visualize this, just imagine that a convective plume usually bulges up from the nearby clouds). This effect is more pronounced for higher CTH because a taller convective plume is less likely to be sandwiched by still taller (and colder) neighbors.

2) *Parallax correction reduces the spread or standard deviation of CTT.* This can be understood as reflecting an overall improved collocation of CTH (from CloudSat) and BT (from MODIS). In other words, the estimated BT is now more closely clustered around the "true" value for that height level (e.g., without parallax correction, we see a CTT of 272.3 K that belongs to a convective cloud with CTH of 15.18 km, as shown in Figure 2.2). The decrease in spread is more pronounced for taller convection than for lower ones for the same reason that the parallax correction on CTT increases with CTH. Together, these changes suggest that parallax correction is particularly important for studying deep convection.
3) As a natural consequence of the decrease in CTT, the fraction of convection with positive buoyancy decreases after parallax correction. Again, the effect is greater for deep convection (with CTH > 10-12 km). Comparisons with previous studies, which had no parallax correction but imposed a "flat-top" condition, show that indeed the fraction of positive buoyancy is smaller when only mature and dissipating convection is selected.

This study is part of an ongoing activity that seeks to understand the underlying convective processes through synergistic measurements from the A-Train constellation.

In a broader sense, this research underscores the subtlety of matching satellite observations from different platforms, even when these satellites fly in close formation like the A-Train constellation. Hopefully, this study can be helpful for refining algorithms used to collocate A-Train data products for the study of clouds (and probably aerosols as well). It would also be useful for any future efforts on coordinating cloud observations from different satellite platforms.

2.6 Acknowledgements

We wish to thank Drs. W.-K. Tao and Dr. X. Zeng at NASA GSFC for helpful discussions and feedbacks. We also thank two reviewers for their useful comments and suggestions. The CloudSat data was obtained from CloudSat Data Processing Center. The MODIS data was obtained from the Goddard Level 1 and Atmosphere Archive and Distribution System (LAADS). The ECMWF interim data used in this study was obtained from http://data.ecmwf.int/data/. This research is supported by NASA MAP project under grant NNX09AJ46G awarded to the University of Michigan and NASA CloudSat/CALIPSO Science Team under grant NNX10AM31G awarded to City University of New York (CUNY).

References

Barnes, W. L., T. S. Pagano, and V. V. Salomonson (1998), Prelaunch characteristics of the Moderate Resolution Imaging Spectroradiometer (MODIS) on EOS-AM1, *IEEE Trans. Geosci. Remote Sens.*, *36*, 1088–1100.

Chan, Mark Aaron, Josefino C. Comiso (2013), Arctic Cloud Characteristics as Derive from MODIS, CALIPSO, and CloudSat. *J. Climate*, 26, 3285–3306.

Ellingson, R. G., J. Ellis, and S. Fels (1991), The intercomparison of radiation codes used in climate models: Longwave results, *J. Geophys. Res.*, *96*, 8929-8953.

Diner, D.J., Beckert, J.C., Reilly, T.H., Bruegge, C.J., Conel, J.E., Kahn, R.A.,Martonchik, J.V., Ackerman, T.P., Davies, R., Gerstl, S. A W, Gordon, H.R.;, Muller, J-P, Myneni, R.B., Sellers, P.J., Pinty, B., Verstraete, M.M (1998), Multi-angle imaging spectroradiometer (MISR) instrument description and experiment overview, *IEEE Transactions on Geoscience and Remote Sensing*, *36*, 1072-1087.

Hasler, A. F. (1981), Stereographic observations from geosynchronous satellites: An important new tool for the atmospheric sciences, *Bull. Am. Meteor. Soc.*, *62*, 194-212.

Holz, R. E., S. A. Ackerman, F. W. Nagle, R. Frey, S. Dutcher, R. E. Kuehn, M. A. Vaughan, and B. Baum (2008), Global Moderate Resolution Imaging Spectroradiometer (MODIS) cloud detection and height evaluation using CALIOP, *J. Geophys. Res.*, 113, D00A19.

Hong, G., P. Yang, A. K. Heidinger, M. J. Pavolonis, B. A. Baum, and S. E. Platnick (2010), Detecting opaque and nonopaque tropical upper tropospheric ice clouds: A trispectral technique based on the MODIS 8–12 μm window bands, *J. Geophys. Res.*, *115*, D20214.

Kahn, B. H., M.T. Chahine, G.L. Stephens, G.G. Mace, R.T. Marchand, Z. Wang, C.D. Barnet, A. Eldering, R.E. Holz, R.E. Kuehn, D.G. Vane (2008), Cloud type comparisons of AIRS, CloudSat, and CALIPSO cloud height and amount, *Atmos. Chem. Phys.*, *8*, 1231-1248.

Kato, S., S. Sun-Mack, W. F. Miller, F. G. Rose, Y. Chen, P. Minnis, and B. A. Wielicki (2010), Relationships among cloud occurrence frequency, overlap, and effective thickness derived from CALIPSO and CloudSat merged cloud vertical profiles, *J. Geophys. Res.*, *115*, D00H28.

Key, J.R.; Santek, D.; Velden, C.S.; Bormann, N.; Thepaut, J.-N.; Riishojgaard, L.P.; Yanqiu Zhu; Menzel, W.P. (2003), Cloud-drift and water vapor winds in the polar regions from MODISIR, *Geoscience and Remote Sensing, IEEE Transactions on* , vol.41, no.2, pp.482,492.

Liu, C., E. Zipser, G. Mace, and S. Benson (2008), Implications of the differences between daytime and nighttime CloudSat observations over the tropics, *J. Geophys. Res.*, *113*, D00A04, doi: 10.1029/2008JD009783.

Luo, Z. J., G. Y. Liu, and G. L. Stephens (2010), Use of A-Train data to estimate convective buoyancy and entrainment rate, *Geophys. Res. Lett.*, *37*, L09804.

Luo, Z., G. Y. Liu, G. L. Stephens, and R. H. Johnson (2009), Terminal versus transient cumulus congestus: A CloudSat perspective, *Geophys. Res. Lett.*, *36*, L05808.

Luo, Z., G. Y. Liu, and G. L. Stephens (2008), CloudSat adding new insight into tropical penetrating convection, *Geophys. Res. Lett.*, *35*, L19819.

Martin Setvák, Kristopher Bedka, Daniel T. Lindsey, Alois Sokol, Zdeněk Charvát, Jindřich Šťástka, Pao K. Wang (2013), A-Train observations of deep convective storm tops, *Atmospheric Research*, 123, 229-248, 0169-8095.

Nagle, Frederick W., Robert E. Holz (2009), Computationally Efficient Methods of Collocating Satellite, Aircraft, and Ground Observations, *J. Atmos. Oceanic Technol.*, 26, 1585–1595.

Nesbitt, Stephen W., Edward J. Zipser, Daniel J. Cecil (2000), A Census of Precipitation Features in the Tropics Using TRMM: Radar, Ice Scattering, and Lightning Observations, *J. Climate*, 13, 4087–4106.

Nishihama, M., Wolfe, R., Solomon, D., Patt, F., Blanchette, J., Fleig, A., & Masuoka, E. (1997), *MODIS level 1A Earth location: Algorithm theoretical basis document version 3.0*, MODIS Science Data Support Team, NASA Goddard Space Flight Center, Greenbelt, MD.

Parkinson, C. L. (2003), Aqua: An earth-observing satellite mission to examine water and other climate variables, *IEEE Trans. Geosci. Remote Sens.*, *41*, 173–183.

Platnick, S., M.D. King, S.A. Ackerman, W.P. Menzel, B.A. Baum, J.C. Riedi, R.A. Frey (2003), The MODIS cloud products: Algorithms and examples from Terra , *IEEE Trans. Geosci. Remote Sens.*, *41*(2), 459 – 473.

Savtchenko, A., R. Kummerer, P. Smith, A. Gopalan, S. Kempler, and G. Leptoukh (2008), A-train data depot: Bringing atmospheric measurements together, *IEEE Trans. Geosci. Remote Sens.*, 46, 2788–2795.

Schreier, M. M., B. H. Kahn, A. Eldering, D. A. Elliott, E. Fishbein, F. W. Irion, T. S. Pagano (2010), Radiance Comparisons of MODIS and AIRS Using Spatial Response Information, *J. Atmos. Oceanic Technol.*, 27, 1331–1342.

Spencer, R. W. (1986), A satellite passive 37-GHz scattering-based method for measuring oceanic rain rates, *J. Appl. Meteor.*, 25, 754–766.

Simmons, A., S. Uppala, S. Dee, and S. Kobayashi (2006), ERA_Interim: New ECMWF reanalysis products from 1989 onwards, *ECMWF Newsletter*, *110*, 25–35.

Stephens, G.L., D.G. Vane, R.J. Boain, G.G. Mace, K. Sassen, Z. Wang, A.J. Illingworth, E.J. O'Connor, W.B. Rossow, S.L. Durden, S.D. Miller, R.T. Austin, A. Benedetti, C. Mitrescu, and CloudSat Science Team (2002), The CloudSat mission and the A-Train:

A new dimension of space-based observations of clouds and precipitation, *Bull. Am. Meteorol. Soc.*, *83*, 1771–1790.

Stephens, G. L., et al. (2008), CloudSat mission: Performance and early science after the first year of operation, *J. Geophys. Res.*, 113, D00A18.

Tian, B., B. J. Soden, and X. Wu (2004), Diurnal cycle of convection, clouds, and water vapor in the tropical upper troposphere: Satellites versus a general circulation model, *J. Geophys. Res.*, *109*, D10101.

Uppala, S., S. Dee, S. Kobayashi, P. Berrisford, and A. Simmons (2008), Toward a climate data assimilation system: status update of ERA-Interim, *ECMWF Newsl.*, *115*, 12 – 18.

Witkowski, Mona, et al., "CloudSat Anomly Recovery and Operational Lessons Learned," in The 12th International Conference on Space Operations: SpaceOps 2012.

Yang, G.-Y., and J. M. Slingo (2001), The diurnal cycle in the tropics, *Mon. Weather Rev.*, *129*, 784 – 801.

Chapter 3

A physically based algorithm for non-blackbody correction of cloud top temperature and application to convection study

The material of this chapter is published in:

Wang, C., Z. J. Luo, X. Chen, X. Zeng, W.-K. Tao, and X. Huang, 2014: A physically based algorithm for non-blackbody correction of cloud top temperature and application to convection study, *J. Appl. Meteor. Climatol.*, in press, doi: http://dx.doi.org/10.1175/JAMC-D-13-0331.1.

3.1. Introduction

Cloud top temperature and cloud top height are two important parameters to retrieve in the remote sensing of clouds. Passive IR remote sensing techniques are sensitive to a finite layer near cloud tops. The thickness of the layer varies from case to case. Thus, solely using IR measurement is not enough to accurately locate the physical cloud top and to estimate the corresponding cloud-top temperature. Yet, precise

knowledge of cloud-top temperature (CTT[1]) and cloud-top height (CTH) is crucial for analyzing certain cloud processes. For example, estimation of convective buoyancy and entrainment rates as described by *Luo et al.* [2010] requires a high accuracy of simultaneous measurements of CTT and CTH. Several attempts have been made in the past to address the problem. *Minnis et al.* [1990] assumed a linear relationship between visible cloud top and infrared cloud emission level and derived an empirical relationship to estimate physical cloud-top temperature using emittance derived from equivalent radiating temperature. In a follow-up study, *Minnis et al.* [2008] analyzed observations from the Cloud-Aerosol Lidar and Infrared Pathfinder Satellite Observation (CALIPSO) Lidar and thermal infrared satellite imagery of Moderate-Resolution Imaging Spectroradiometer (MODIS), and concluded with an expression for the cloud top altitude of optically thick ice clouds as a function of the emission level. Along a similar line, *Sherwood et al.* [2004] examined the relationship between thermal cloud top heights derived from geostationary satellite infrared imageries and direct measurements using air-borne lidar observations and showed that the thermal cloud top is consistently ~1 km lower than the lidar cloud top. The aforementioned studies heavily rely on Lidar and infrared brightness temperature. Lidar cannot penetrate deep into clouds. Although it can accurately determine the cloud top, lidar has difficulties in probing the in-cloud structure, especially for the convective core and thick anvils. Including simultaneous radar measurements will be helpful because radar can better profile thick clouds. Therefore, we pursue radar-lidar synergy in this study.

[1] Hereafter CTT refers to the physical temperature at cloud top, not the brightness temperature as commonly used in the literature.

A common approach to infer the cloud top temperature of opaque clouds from IR passive remote sensing is to use the brightness temperature in the IR window region, typically over the 11-μm band (BT_{11}). BT_{11} is a function of the temperature at cloud top as well as temperatures within a layer below due to the non-blackbody effect of clouds. However, the vertical structure of cloud microphysics (such as cloud water content or CWC) near the cloud top varies from one cloud to another, affecting the depth of the layer over which IR measurements can penetrate. Some cloud tops are fuzzy with small cloud water content (moderate vertical gradient in optical depth) while others are compact with large cloud water content (large vertical gradient in optical depth). CloudSat, a space-borne 94GHz radar in operation since July 2006, is able to profile cloud structure with high vertical resolution and is also able to directly determine the cloud top. Its inability to detect small cloud particles near the top is complemented by the two-wavelength polarization-sensitive lidar aboard CALIPSO [*Winker et al.*, 2009]. Furthermore, CloudSat, CALIPSO, and MODIS aboard Aqua as part of the A-Train constellation [*Stephens et al.*, 2002] make almost simultaneous observations. These facts motivate this study to explore how the vertical structure near cloud top is related to BT_{11} and how passive and active remote sensing measurements (namely, CloudSat, CALIPSO, and MODIS) can be used together to estimate CTT for optically thick clouds.

The motivation articulated in the previous paragraph is illustrated by two convective clouds in Figure 3.1 with CloudSat radar reflectivity (in unit of dBZ) profiles in color scale and the natural logarithm of ice water content (IWC) derived from the combination of CloudSat and CALIPSO in gray scale. The vertical profiles of optical depth for the MODIS 11-μm channel are calculated using vertical profiles of CWC

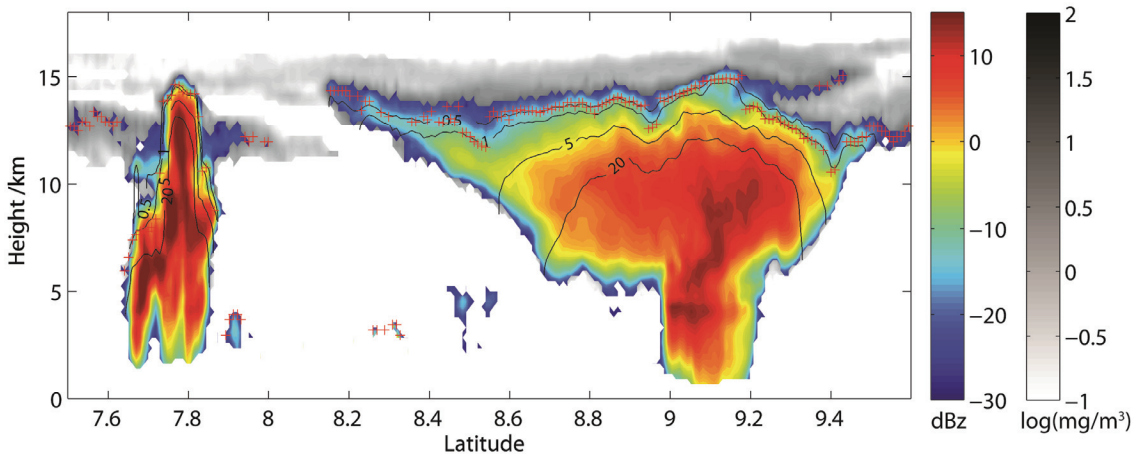

Figure 3.1. CloudSat radar reflectivity (in dBZ) observed at 06:37 UTC on 10 October 2008 is shown in color scale and the natural logarithm of cloud ice water (in mg m^{-3}) content in gray scale. The black contour lines (from the uppermost to the lowermost) are for IR optical depths of 0.5, 1, 5, and 20, respectively. The red plus signs mark the levels with maximum weighting functions (the effective emission levels). This is the same event as Figure 3 in *Wang et al.* [2011].

retrieved by CloudSat and CALIPSO (see Section 3.2 for calculation details). From top to bottom, the black contour lines show the 11-μm optical depth (τ_{11}) of 0.5, 1, 5, and 20, respectively. The red pluses mark the effective emission levels (EEL), which are defined as the altitudes corresponding to the peaks of the weighting functions of MODIS 11-μm channel. Both radar reflectivity and cloud optical depth in the figure suggest that the convective cloud on the left has a more compact top than the one on the right. For the convective cloud on the right, the cloud-top fuzziness (as measured by the vertical gradient of radar reflectivity or optical depth) varies across the cloud. Consequently, the distance between the EEL (the red plus signs) and the radar cloud top is larger where the cloud top layer is fuzzier and smaller where the cloud top layer is more compact. Hereafter, cloud tops are always defined as the altitude where the CloudSat radar

reflectivity first reaches its detection limit, ~-30dBZ. Such correlation between the vertical gradient of CloudSat radar reflectivity and the vertical gradient of 11-μm optical depth will be explored quantitatively in this study to better estimate physical cloud top temperature. Current space-borne cloud remote sensing provides the capability to capture the vertical profiles of radar reflectivity (e.g., CloudSat) and lidar backscatter (e.g., CALIPSO) but not the profiles of 11-μm optical depth; yet it is the latter quantity that is most directly related to the IR determination of cloud-top temperatures.

To complement the analysis of observational data, three-dimensional (3D) cloud resolving model simulations are used to provide a more complete understanding of the relationship. Specifically, the Goddard Cumulus Ensemble model (GCE) [e.g., *Zeng et al.*, 2009] is employed to simulate clouds and precipitation, driven by the large-scale forcing obtained from a field campaign. The GCE simulations are analyzed for studying detailed in-cloud structures that are elusive to satellite measurements (e.g., in-cloud temperature profile), aiming at a physically-based understanding of the relationship among cloud top temperature, BT_{11} and CloudSat radar reflectivity.

The rest of the chapter is organized as follows: Section 3.2 introduces the data sets, GCE model, and radiative transfer calculation used in the study. Section 3.3 describes results obtained by examining collocated CloudSat, CALIPSO, and MODIS observations and analyzing radiative transfer model simulations. Section 3.4 analyzes results from GCE model simulations. Section 3.5 discusses the application to the convective buoyancy study. Finally, Section 3.6 presents summary and conclusions.

3.2. Observations, Models, and Data Processing

3.2.1 Observations

3.2.1.1 CloudSat and CALIPSO

The potential benefits of combining cloud profiling radar and lidar together to probe the cloud have been well recognized [*Sassen et al.*, 2009; *Luo et al.*, 2010; *Luo et al.*, 2011; *Young et al.*, 2012]. Because the lidar on CALIPSO and the cloud profiling radar (CPR) on CloudSat utilize different wavelengths, they are sensitive to cloud particles of different sizes. The lidar is operating in the visible wavelength and is able to detect thin cirrus clouds and aerosols but its laser pulse is strongly attenuated by optically thick cloud. The CloudSat radar, on the other hand, can typically sense and penetrate non-precipitating cloud but can barely detect the thin cirrus with small particle sizes. Therefore, combining information from lidar and radar allows for a more complete description of the geometrical and microphysical parameters of clouds, given the wide varieties of size distribution of cloud particles within clouds [*McGill et al.*, 2004; *Minnis et al.*, 2012; *Okamoto et al.*, 2003]. For this reason, we use joint CloudSat-CALIPSO product, whenever possible, to study cloud top properties in this study. CloudSat and CALIPSO fly at an altitude of 705 km in a Sun-synchronous polar orbit and make equatorial passes at approximately 1:30am and 1:30pm local time. The 94-GHz nadir-viewing CPR onboard CloudSat profiles clouds with a vertical resolution of 480 meters oversampled to 240 meters and its ground footprint is approximately 1.7 km along track and 1.3 km cross track [*Stephens et al.*, 2008]. CALIPSO payload consists of an imaging infrared radiometer, a wide field camera, and a two-wavelength lidar with ability to

resolve the orthogonally polarized components of the 532-nm backscattered signal. The lidar backscatter signal can profile clouds up to an optical depth of about 3 with a resolution of 60 m in vertical and 333 m in horizontal.

The following CloudSat-CALIPSO data products are used, all obtained from the CloudSat Data Processing Center[2]. 1) 2B-GEOPROF provides the CPR radar reflectivity profiles and is used in this study to identify cloud tops and to quantify the fuzziness of cloud top layer. 2) 2B-CWC-RVOD and 2C-ICE provide cloud microphysics parameters such as CWC, which is used as the input for radiative transfer model calculations. 2C-ICE product is based on joint retrieval from collocated CloudSat and CALIPSO measurements and provides ice water content [*Deng et al.*, 2010]. 2B-CWC-RVOD product has both liquid water content (LWC) and ice water content (IWC), but the information content is largely derived from the CloudSat CPR and constrained by MODIS visible optical depth [*Wood* 2008]. *Deng et al.*, [2013] shows that 2C-ICE outperform 2B-CWC-RVOD in cloud ice microphysics retrieval, underscoring the importance of radar-lidar synergy in ice cloud property retrievals. To take advantage of the radar-lidar synergy, we used 2C-ICE product for IWC profiles. 2B-CWC-ROVOD data are used only for its LWC profiles.

We define a parameter that will later be used to measure near cloud-top condition, which we call cloud top fuzziness (CTF),

$$\mathrm{CTF} = \mathrm{CTH} - 10\mathrm{dBZ\ ETH} \tag{3.1}$$

[2] The CloudSat Data Processing Center can be accessed via http://www.cloudsat.cira.colostate.edu/

where CTH (cloud top height) is defined based on CloudSat CPR corresponding to the height of -30dBZ, and 10dBZ ETH (echo top height) is the highest altitude reached by 10 dBZ. 10dBZ echo is an indicator of the presence of large precipitation-size particles and thus 10dBZ ETH is a good proxy for convective strength [*Luo et al.*, 2008; *Luo et al.*, 2011]. CTF so defined thus measures the extent to which precipitation-sized particles are transported to near the cloud top. The smaller the CTF, the more compacted the cloud top is, and vice versa. It will be shown later that CTF is closely related to the correction for the IR non-blackbody effect.

3.2.1.2 MODIS

MODIS aboard Aqua flies in close formation with CloudSat, being separated from each other by a variable time interval but always less than 120 seconds. It measures narrowband radiances in 36 spectral bands from 0.415 μm to 14.24 μm with wavelength-dependent nadir spatial resolutions from 250 m to 1 km in a 2300-km-wide swath [*King et al.*, 1992; *Platnick et al.*, 2003]. The 11-μm brightness temperature, BT_{11}, from the Aqua-MODIS measurement is collocated to CloudSat observations after the correction of parallax shift following the method depicted in *Wang et al.* [2011].

3.2.1.3 Analysis of observational data

The ambient temperature and relative humidity are obtained from the CloudSat ECMWF-AUX data set and are inputted to the radiative transfer simulation. ECMWF-AUX is based on the European Center for Medium-Range Weather Forecasts (ECMWF) operational analysis, spatially and temporally interpolated to the CloudSat track. Note that the optical depth in CloudSat Level-2 product, the CloudSat 2B-TAU, is for 0.55 μm,

which is different from the 11-μm optical depth used throughout this study. We calculate the 11-μm optical depth using the PCRTM, a radiative transfer model to be described in Section 3.2.3.

All CloudSat data and 2C-ICE retrievals collected within the tropics (30^{o}S - 30^{o}N) in the year of 2008 are analyzed here. We choose convective clouds by the criteria that (1) CTF is less than 4km and (2) CTH is greater than 6 km such that boundary-layer convective clouds are excluded. As a result, 277,968 profiles (0.43% of total CloudSat observations in the tropics) meet our criteria. To best capture the behavior of the core of convection, for each strong convective cloud that has consecutive CloudSat radar echo profiles that meet our criteria, we only use the one with the highest CTH considering that it is likely to be closer to the actual convective core. This reduces our selected profiles to a total of 16,837 for the following analysis. Figure 3.1 shows two examples of the selected convective clouds. More details of selection of convective clouds can be found in *Wang et al.* [2011].

3.2.2 Goddard Cumulus Ensemble (GCE) Model

The GCE model is a cloud resolving model that has been developed at NASA Goddard Space Flight Center over the past decades (e.g., *Tao and Simpson* [1993]; *Tao et al.*, [2002]), and is extensively used to study cloud processes and their interactions with the environment. The model is non-hydrostatic and anelastic. Its subgrid-scale turbulent processes are parameterized with a scheme based on *Klemp and Wilhelmson* [1978] and *Soong and Ogura* [1980]. The model includes solar and infrared radiative transfer processes, and explicit cloud-radiation interaction processes. The model has five

prognostic hydrometeor variables: the mixing ratios of cloud water, rainwater, cloud ice, snow and graupel (see *Tao et al.* [1993; 2003] and *Lang et al.* [2003] for details).

In this study, GCE simulations are used as a surrogate of real convective cloud development processes. The model is driven by the large-scale tendencies observed in the Tropical Warm Pool – International Cloud Experiment (TWP-ICE) [*May et al.*, 2008], and uses 256×256 horizontal grid points at 1-km resolution. Its modeling results have been evaluated with C- and W-band radar data as well as satellite data [*Zeng et al.*, 2013].

The TWP-ICE simulation analyzed here lasts for six days (Feb 6^{th} ~ Feb 12^{th}, 2006) and 2429 simulated convective cores are identified in total. All information on those cores is fed into QuickBeam (see Section 3.2.3) to simulate 94-GHz radar reflectivity that mimics CloudSat CPR from a nadir view. In addition, PCRTM, a fast and accurate thermal radiative transfer model, is used to simulate MODIS BT_{11} as well as the vertical profile of optical thickness with the same the MODIS viewing zenith angle. The emission level is then derived by calculating the corresponding weighting function and by locating its peak.

Cloud selection method for observational data analysis is applied similarly to the model simulations. Specifically, convective clouds are selected for analysis if their CTH ranges from 6 to 18 km and is within 4 km of the simulated 10dBZ ETH. Similar to the data selection process for satellite measurement, simulated profile at one model grid is used to represent the core of a convective cloud. A convective core in the model is defined based on the following criteria: (1) grid points are classified as a convective region by GCE, (2) maximum upward velocity exceeds 2 m s^{-1}, (3) outgoing longwave

radiation is less than 210 W m^{-2}, (4) integrated water path is greater than 0.5 cm, and (5) simulated MODIS BT_{11} by PCRTM is less than 270 K. Each convective core is treated as one entity and for a cluster of neighboring cores, the one with the largest cloud water content is used to represent them for further analysis, similar to the analysis as described in Section 3.2.1.

3.2.3 QuickBeam, PCRTM, and model-to-satellite simulation strategy

GCE outputs such as mixing ratios of cloud hydrometeors are fed into QuickBeam simulator [*Haynes et al.*, 2007] to derive synthetic CloudSat radar reflectivity. This ensures consistent ways of defining the CTT and ETH between model simulations and observations. In this study, the mixing ratios of the five kinds of hydrometeor species in GCE are specified for the QuickBeam. To be consistent with the intrinsic size distribution of the GCE [*Tao and Simpson*, 1993], snow, graupel, and rainwater are assumed to have exponential size distribution; cloud water and cloud ice are assumed to be monodisperse in the QuickBeam simulator[3]. The scattering and absorption by atmospheric gases and thus gaseous attenuation of the radar beam are taken into account. Therefore, with the output of radar echo, CTT and ETH for clouds in GCE simulation can be similarly defined, bridging the gap between CloudSat observation and GCE simulation.

The Principal Component-based Radiative Transfer Model (PCRTM) [*Liu et al.*, 2006] is now becoming a widely used atmospheric radiative transfer model in IR remote sensing community for its computational efficiency and accuracy. Unlike channel-based

[3] These size distributions are applied to maximize consistency with GCE output. We note here that the size distribution of hydrometeors in reality could be much more complicated than the one assumed in the QuickBeam simulator.

radiative transfer models, PCRTM computes the principal component scores of channel radiance, which greatly improves computational efficiency. The benchmark comparison with line-by-line radiative transfer model also shows that PCRTM performs satisfactorily in terms of accuracy. Further technical details about the PCRTM can be found in *Liu et al.* [2006; 2009]. Multiple scattering is incorporated into PCRTM by including a pre-calculated look-up table of reflectance and transmission of clouds using the discrete-ordinate-method radiative transfer [*Stamnes et al.*, 1988]. Single scattering properties are obtained from *Yang et al.* [2001], *Wei et al.* [2004], and *Niu et al.* [2007] by averaging the single-scattering properties The complex refractive indexes of ice are taken from *Warren* [1984] with his 1995 update and that of water from *Segelstein* [1981].

The PCRTM is used here for two purposes: (1) calculating BT_{11} with inputs of vertical profiles of cloud water content, temperature, and humidity, and (2) calculating IR transmissivity of each discretized vertical layer. For simulating BT_{11} using CloudSat and CALIPSO observations, inputs to the PCRTM are IWC profile from CloudSat 2C-ICE product, and temperature and humidity profiles from ECMWF operational analysis. For simulating BT_{11} using GCE simulations, the GCE output of the same variables are directly fed into the PCRTM. PCRTM calculation is done at a spectral resolution of 1 cm^{-1} (full width at half maximum) and the result is then convolved with the spectral response function of the MODIS 11-μm band[4]. In this work, a sensor-viewing zenith angle is set to match those of collocated MODIS observations. To ensure enough vertical resolution to accurately identify the peak altitude of the weighting function, the transmissivity is calculated for every 50-meter interval in the troposphere. Temperature and humidity

[4] The spectral response function is available at http://mcst.gsfc.nasa.gov/calibration/parameters

profiles above the cloud top are taken from the ECMWF-AUX data products. The relative humidity was set to 100% whenever hydrometeors were present. For CloudSat-CALIPSO-MODIS related analysis, treatment of the in-cloud temperature profiles in the PCRTM modeling needs some further assumptions and will be described in detail in the next section. For the GCE simulation, no assumption is needed for in-cloud profiles since everything is available from the GCE direct output. BT_{11} at the top of atmosphere and the corresponding transmissivity at 50-meter vertical resolution are obtained from PCRTM calculations. The latter is then numerically differenced to derive the weighting function. As mentioned in Section 3.1, the effective emission level (EEL) is then defined as the altitude where the weighting function attains its maximum.

3.3. Non-blackbody correction for the tropical deep convection

3.3.1 Effective emission level (EEL) and relation to cloud-top fuzziness

We first numerically investigate the question "where is the peak of the weighting function for the IR window channel near 11 μm?". While it is often assumed that the peak of the IR weighting function is located at the altitude where optical depth τ=1, this exact statement is either based on the assumption that Planck function varies linearly with respect to optical depth with no scattering effect [*Sherwood et al.*, 2004] or based on other approximations about the absorption lines [*Stephens* 1994; *Goody and Yung*, 1995]. In this study, we use a full-fledged radiative transfer model, the PCRTM, to explicitly evaluate the peak of the weighting function in the presence of scattering inside cloud. Figure 3.2 shows the histogram of τ_{11} where the weighting function attains its maximum. Based on Figure 3.2, the expected value of τ_{11} is 0.72 with the standard deviation of 0.3.

Among all cases examined here, 99.4% of all cases examined here have the weighting functions peaking at $\tau_{11} < 2$. The histogram is largely symmetric except a small tail beyond $\tau_{11} > 2$, which is found to be caused by interpolation of the cloud optical depth in the presence of extremely large vertical gradient of cloud water content at the cloud top.

As shown in Figure 3.1, the distance from cloud top identified by CloudSat to the EEL changes with the fuzziness of the cloud top. Figure 3.3 further demonstrates this with a 2-D histogram showing the relationship between CTF and the distance from CTH

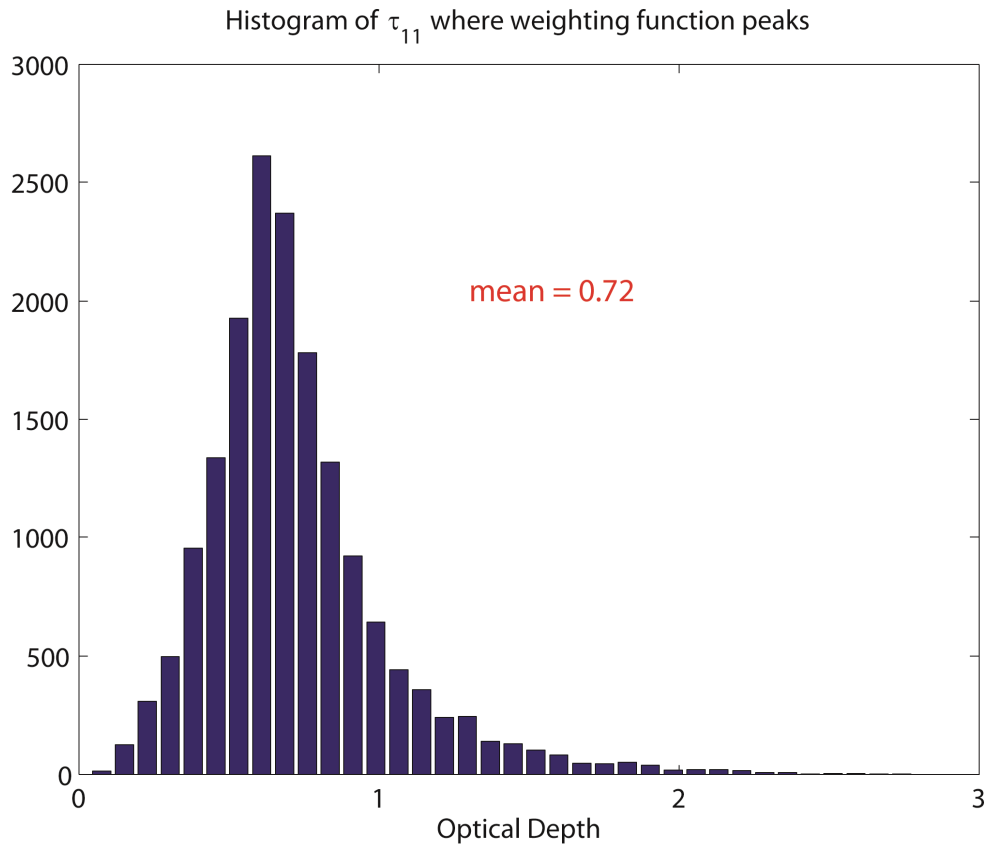

Figure 3.2. Histogram of the effective emission level (the peak of weighting function) expressed in the 11-μm optical depth. The histogram indicates mean effective emission level is at the IR optical depth of 0.72.

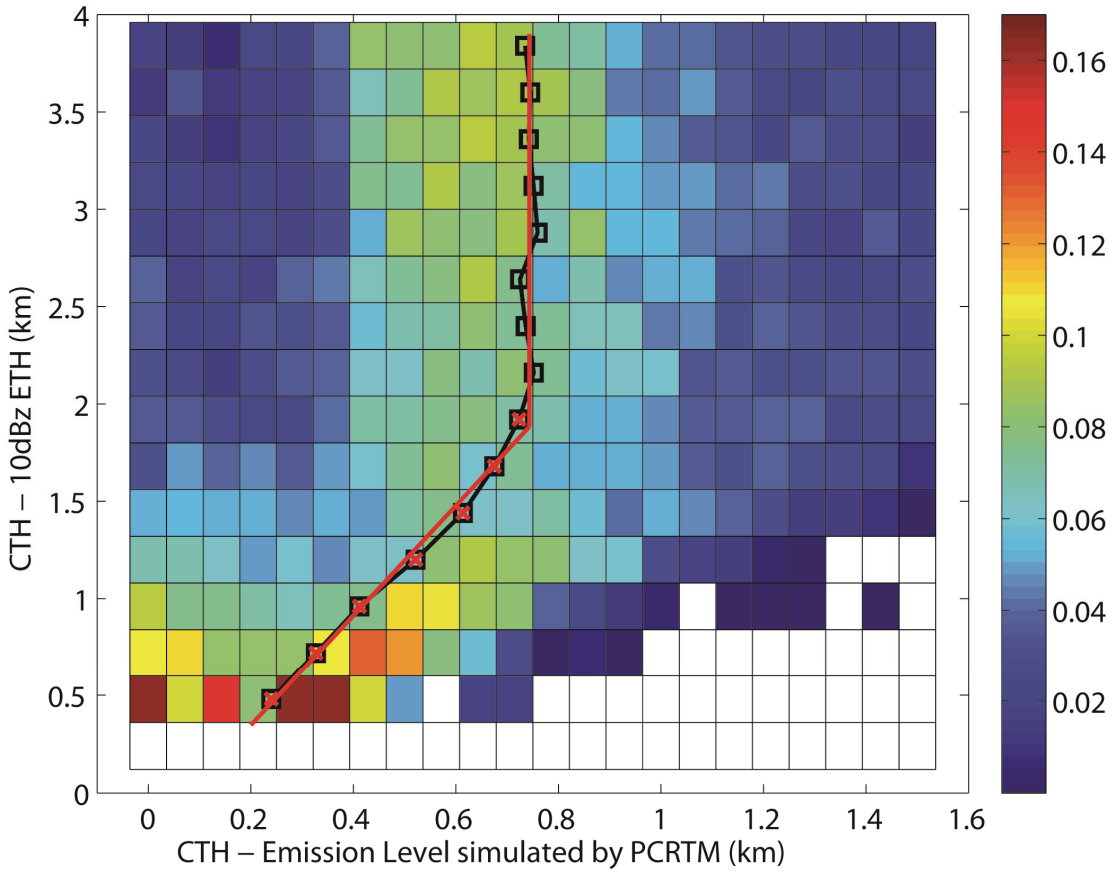

Figure 3.3. The 2-D histogram of the distance between CTH and the EEL computed by PCRTM (abscissa) versus the distance between CTH and 10dBZ echo top height (ETH) (ordinate). The figure is normalized for each CTH-10dBZ ETH interval. The black squares show the expected distance between CTH and EEL from such probability distributions. The red line is the regressed results.

to the EEL derived from the PCRTM calculation (denoted as x hereafter). The quantity x is critical to non-blackbody correction of the CTT. Figure 3.3 shows that it is related to CloudSat radar reflectivity profiles and thus can be parameterized using such measurements. The composite result $x=x(CTF)$ is shown in black line with squares. The composite in Figure 3.3 shows that, when *CTF* is smaller than ~2 km (i.e., relatively compact cloud top), x is nearly linearly proportional to *CTF* and, when *CTF* is more than

~2 km, *x* composite becomes constant at ~0.74 km. This can be expressed mathematically as,

$$x = \min(\frac{CTF + b}{a}, 0.74) \tag{3.2}$$

where the values of *a* and *b* are determined by the linear regression of the data. To assess the impact of the CloudSat 2C-ICE retrieval uncertainty on the values of *a* and *b*, we randomly perturb IWC and LWC profiles with random numbers that follow normal distributions in accordance with the corresponding 2C-ICE retrieval uncertainties. Such perturbed profiles are then fed to QuickBeam and PCRTM to generate figure similar to Figure 3.3, and then derive values of *a* and *b* for this set of perturbation. We repeat such random perturbation calculation for 20 times and use them to estimate the uncertainty due to retrieval uncertainty of IWC and LWC. By this way, a = 2.83 with a 1-σ uncertainty of 0.069 and b = 0.22 with a 1-σ uncertainty of 0.044.

3.3.2. Temperature at the effective emission level versus BT_{11}

To make the relation derived in Eq. (3.1) useful to estimating CTT, knowledge of the in-cloud temperature at the EEL (T_{EEL}) is needed. T_{EEL} is slightly different from the actual BT_{11} which is a weighted average of the in-cloud temperatures along a layer near cloud top. However, current remote sensing techniques cannot provide direct measurement of the vertical profile of in-cloud temperature; in-situ measurements inside cumulonimbus are rare. So, we used GCE model simulation to investigate the differences between T_{EEL} and BT_{11}.

Results based on GCE simulations are presented in Figure 3.4 as a number density plot with the ordinate representing the simulated CTF (=CTH–10dBZ ETH) and the abscissa representing the difference between T_{EEL} and BT_{11}. The figure shows that the T_{EEL}-BT_{11} difference has an appreciable spread largely independent from CTF. The mean of T_{EEL}-BT_{11} difference is 0.11 K with a standard deviation of 2.3 K. Such spread could be due to a variety of factors such as the inclusion of multiple scattering in our radiative transfer calculation, the subtle variations of hydrometeor profiles near the cloud top as simulated by the GCE model, etc. Based on the student's t-test, the 0.11-K mean

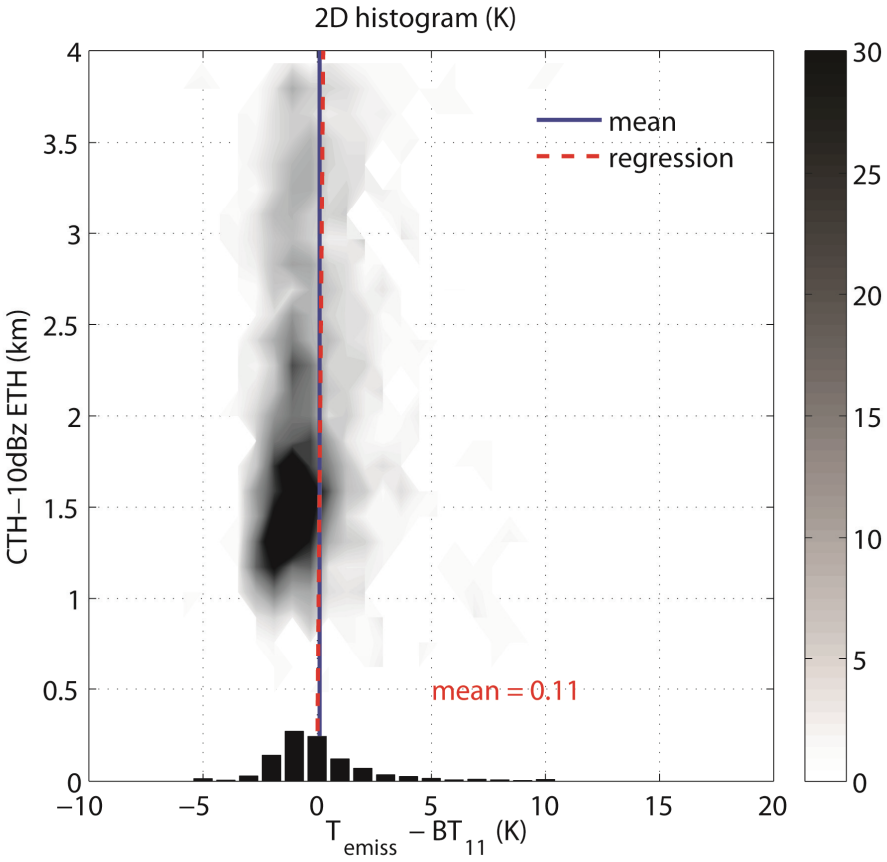

Figure 3.4. Number density plot of GCE-simulated cases. Outliers outside of 3-sigma range are not included. Histogram shows as black bars. The red dotted line is the regression result and the blue line is T_{EEL} –BT_{11}=0.11K.

difference is statistically different from zero at significance level of 0.04. This small positive difference can be understood in the following way: ideally assuming temperature decreases linearly with altitude, the weighting function, largely bearing the shape of a Chapman function [Chapter 6; *Goody and Yung*, 1995], is slightly skewed to its upper tail. Therefore, as long as the effective emission level resides well below the tropopause, which is true for most cases except overshooting convection, BT_{11} could be considered to be slightly smaller than the temperature at the emission level. Nevertheless, it should be noted that 0.11 K is such a small difference compared with the uncertainty of satellite measurement for cloud tops [*Paul et al.*, 2008] that for mostly practical reasons. Therefore, BT_{11} can be treated as a good approximation of the T_{EEL} for convective clouds.

Based on these calculations, we arrive at the following expression to estimate cloud top temperature based on MODIS BT_{11} and CloudSat measurements:

$$CTT = BT_{11} - \Gamma_m \min(\frac{CTF + 0.22}{2.83}, 0.74) + 0.11\text{K} \tag{3.3}$$

where *CTF* is cloud top fuzziness in kilometer and Γ_m is the moist adiabatic lapse rate around the top of the cloud in kelvin per km. Physically, Equation 3.3 states that the IR non-blackbody correction, namely the difference between CTT and BT_{11}, is proportional to the CTF parameter defined in Section 3.2.1: fuzzier the cloud top (larger CTF), greater the correction, and vice versa. It is also proportional to the in-cloud lapse rate, Γ_m.

As far as uncertainties in Equation 3.3 are concerned, the measurement uncertainty of BT_{11} is ~0.34 K [*Xiong et al.*, 2009]. For the second term on the right side of Equation 3.3, its uncertainty is ~4 K given Γ_m ~8 K km^{-1} at convective cloud top and

the standard deviation of emission level estimation ~0.5 km. The standard deviation of T_{EEL}-BT_{11} difference, i.e., the third term on the right side of Equation 3.3, is 2.3 K. Since the histograms in Figure 3.3 and Figure 3.4 can be viewed as empirical probability distribution functions (pdf), the uncertainty can be assessed in the following Monte-Carlo way: for any given *y* in Figure 3.3, obtaining an estimate of *x* in Figure 3.3 according to the empirical pdf determined by the histogram in Figure 3.3. Similar steps apply for the T_{EEL}-BT_{11} difference with the given standard deviation. Such estimate will be used in Equation 3.3 in lieu of the regression formula to get an estimate of CTT. By doing such estimate many times, an uncertainty for the CTT estimated by Equation 3.3 can be derived. Figure 3.7 will show the results using such Monte-Carlo approach.

3.4. Simulated versus observed BT_{11}

To gain more confidence in our non-blackbody correction for convective clouds, we compare BT_{11} from the PCRTM simulation with the observed BT_{11} from Aqua-MODIS. BT_{11} is simulated based on estimation of CTT. The approach adopted here is backward in comparison to Section 3.3, namely, we assume that CTT is known and then start from there to calculate BT_{11}. The rationale is to see if we can close the problem both ways.

We compare two approaches in terms of estimating the in-cloud temperature profiles. One approach assumes no *a priori* knowledge of CTT and uses the ambient air temperature at the cloud top level (taken from the ECMWF-AUX product) to represent the CTT and further assume moist adiabatic change of temperature inside the cloud. The color contours in Figure 3.5a show the 2-D histogram of the simulated and the observed

BT_{11} following this assumption. The second approach assumes BT_{11}+0.11 K as the temperature at the EEL and calculates CTT according to Equation 3.3. Note that the second approach does not require neutral cloud top buoyancy, i.e., CTT equal to the ambient temperature. Black contour lines in Figure 3.5a show the result from the second approach. The regressed slope of simulated BT_{11} vs. MODIS BT_{11} is 0.995 for the first approach with R^2 of 0.96 and 1.004 for the second approach with R^2 of 0.99. To better illustrate the improvement, panel (b) and (c) show the 2-D histogram of the differences between simulated and measured BT_{11} with respect to MODIS BT_{11}, without and with our non-blackbody correction method, respectively. In contrast to Figure 3.5b, Figure 3.5c with the correction demonstrates that the second approach yields tighter distribution and that the cases are better aligned at the zero-difference line, especially for the lower cloud. Therefore, we conclude that BT_{11} is better simulated when CTT is computed using our non-blackbody correction method, as opposed to assuming CTT equals the ambient air temperature. The small difference between CTT and the ambient air temperature is proportional to convective buoyancy, as will be discussed in Section 3.5.

Figure 3.5c shows that tropical convective clouds above the planetary boundary layer tend to cluster around two temperature ranges, namely, 250-265 K and 200-220 K. They correspond to two equally obvious modes of convective clouds [*Johnson et al.*, 1999]: cumulus congestus and deep convection, as noted in *Luo et al.* [2010]. Overall, Figure 3.5 suggest that the observed BT_{11} can be largely reproduced given knowledge of CWC and temperature profiles. This is encouraging and lends support to the validity of our method. There are also some noticeable biases. For example, there is a ~2-K warm bias for the black contours when BT_{11} is lower than 240 K (i.e., the deep convection

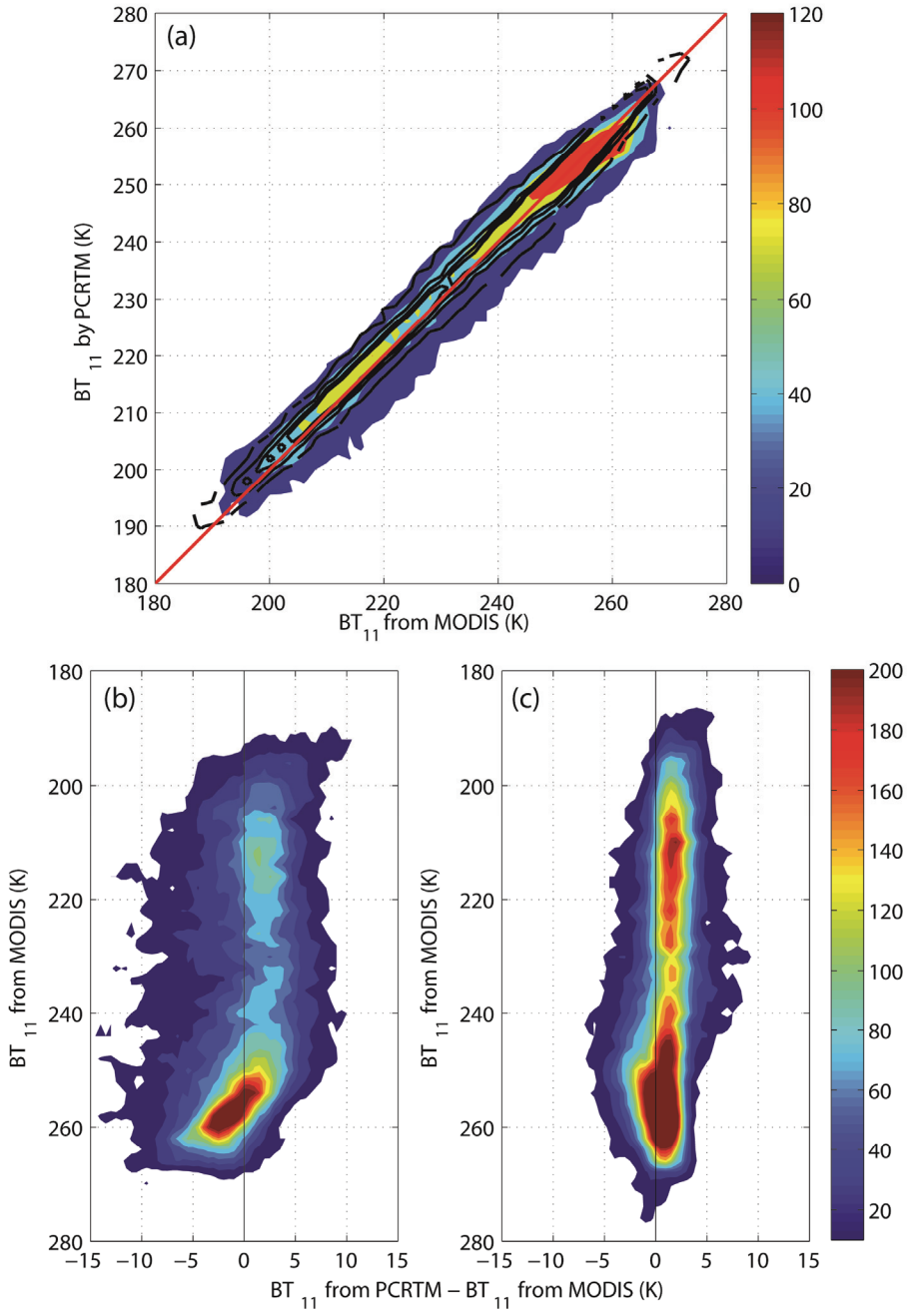

Figure 3.5. (a) 2-D histogram of numbers of occurrences of BT11 measured by MODIS (abscissa) and simulated using PCRTM with CloudSat cloud water profiles and temperature and humidity profiles as described in the context (ordinate). The red line with slope of 1:1 is plotted as a reference. Color filled contours are results assuming CTT equal to the ambient air temperature. The black contours are the result from updated estimation of CTT described in Section 3.4. Panel (b) and (c) show the difference between simulated BT_{11} and MODIS measurement with respect to MODIS BT_{11} with and without non-blackbody correction, respectively. Same set of color contours are used in (b) and (c).

mode). For BT_{11} > 240 K (i.e., the cumulus congestus mode), the simulated BT_{11} distributes closely along the red line with a warm bias of less than 0.5 K. The bias is larger for approach 1 (where CTT is assumed to equal that of the environment) than approach 2 especially for the cumulus congestus mode. A number of reasons could account for these biases. For example, the ECMWF analyses, which represent the large-scale environment, may not accurately capture the temperature profile near convective

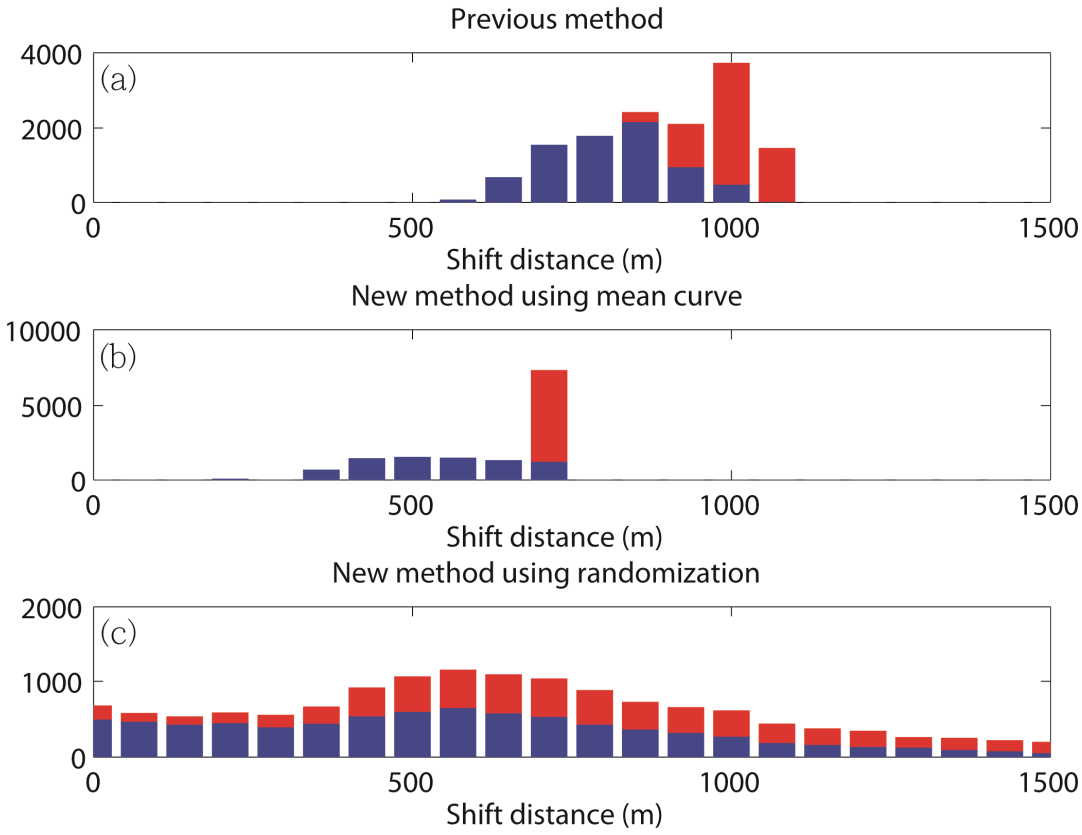

Figiure 3.6. Histogram of distance between cloud top and EEL for all cases examined here. Blue bars show the histogram of cases with CTH-10dBZ ETH less than 2 km. The red bars are for cases with CTH-10dBZ ETH within 2-4 km range. (a) Based on previous method used in *Luo et al.* [2008]. (b) Using Equation 3.2 to compute such distances. (c) The empirical PDF based on Figure 3.3 is used to estimate the distances (more details of this estimation can be found at the end of Section 3.4).

clouds especially when convection triggers local diabatic and adiabatic processes that could influence the vertical temperature profile at the spatial scale comparable to the MODIS footprint.

3.5. Comparison with previous study and application to studying convective buoyancy

An important reason why accurate knowledge of CTT is critical can be traced to a series of recent publications [*Luo et al.*, 2008 and 2010; *Wang et al.*, 2011] which utilize the synergy between CloudSat and MODIS measurements to estimate convective buoyancy. Convective buoyancy (B) is proportional to the difference between CTT and the ambient air temperature of the same height level. *Luo et al.* [2010] concluded through a sensitivity and uncertainty test that CTT is the major source of error in convective buoyancy estimation. Even a merely 1-2K error in CTT is large enough to affect the determination of the "fate" of some convective clouds, namely, whether they are bound to take further ascent or have already lost buoyancy.

In previous studies, Luo et al. (2010) and Wang et al. (2011) used a simple, empirical method to correct for non-black cloud-top emissivity as follows: since CALIPSO lidar signal cannot penetrate beyond an optical depth at visible wavelength (τ_{vis}) of ~3, this attenuation depth provides a means of estimating the correspondence between τ_{vis} and physical depth. It is further assumed that the effective IR emission level is located at $\tau_{IR} = 1$ and the relationship between τ_{vis} and τ_{IR} follows that provided by ISCCP (Rossow et al. 1996): $\tau_{vis}/\tau_{IR} = 2.56$ for water clouds and 2.13 for ice cloud. Clearly, this correction method is rather crude. For example, lidar penetration depth may deviate from τ_{vis} of 3 and τ_{vis} may not vary linearly with depth. Also, the effective IR

emission level may not always occur at $\tau_{IR} = 1$, as demonstrated in Fig. 2. Moreover, the visible-to-IR optical depth conversion is not a constant and may vary from one case to another. Nevertheless, it represented our first attempt to address the problem. Here, we compare results derived from the previous method with those from this study which is more physically-based.

Figure 3.6 shows the histograms of the distance from cloud top to the EEL, i.e., x in Equation 3.2, as derived using three different methods. The upper panel (Figure 3.6a) is based on the old method used in *Luo et al.* [2010] and *Wang et al.* [2011]. Since Figure 3.3 shows that the relationship changes from CTF < 2 km to CTF > 2 km due to the saturation of emission at that level, we divide the selected convective cases into two different groups: one has CTF less than 2 km and the other has CTF at 2~4 km. They are shown in blue and red bars in Figure 3.6, respectively. In Figure 3.6a, the blue histogram shows a peak around 0.8 km with a spread between 0.5 and 1 km. The red histogram reaches its maximum at around 1 km.

Figure 3.6b is based on Equation 3.2: the blue histogram has similar spread as the bar histogram in the upper panel but the peak of the histogram is now at 0.5 km. The expected emission level, as shown in Figure 3.2, is where τ is ~0.72 instead of exact one as assumed in the previous method. Therefore, the new non-blackbody correction should be smaller than that by *Luo et al.* [2010] and *Wang et al.* [2011], which leads to warmer CTTs than previous estimates.

Figure 3.6c is based on the estimates using the empirical PDF derived from Figure 3.3 instead of Equation 3.2, as explained in the last paragraph of Section 3.3. It shows wider spread for both groups than Figure 3.6b, but their peaks are at similar locations and the expectation of the red histogram corresponds to the red bar in the middle panel. This can be explained by the fact that Figure 3.6b is based on the regression values derived from Figure 3.3 while Figure 3.6c takes the entire spread in Figure 3.3 into account. Hereafter, the correction estimated from such empirical PDF is denoted as PDF-based

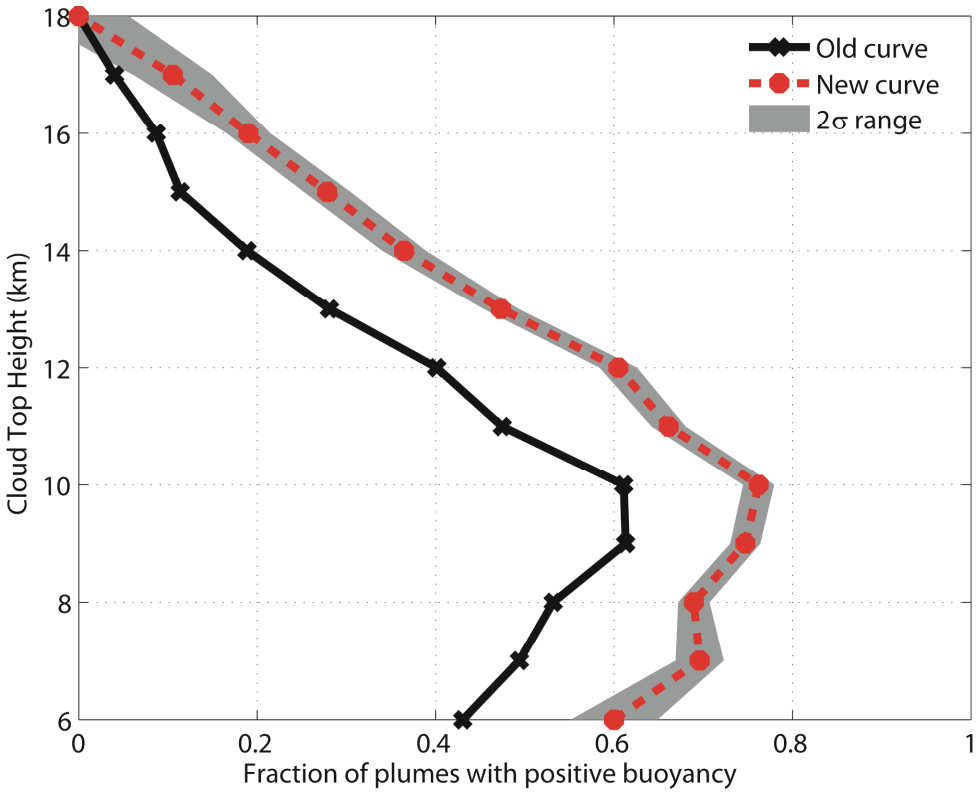

Figure 3.7. Fraction of convection clouds with positive buoyancy as a function of cloud top height. The bin size of cloud top height is 1 km. The black line corresponds to the black line in Figure 3.6 of *Wang et al.* [2011] with a small coding bug cleared. The red line is based on Equation (3.3) and shows the fraction for all cases. The shaded area indicates the 2-sigma range calculated based on Figure 3.3 and Figure 3.4.

correction and the correction using Equation 3.2 is referred to as regression-based correction.

As an application, the convective buoyancy as analyzed in *Luo et al.* [2010] and *Wang et al.* [2011] is re-examined. The convective cloud top buoyancy is represented by the difference between CTT and the ambient air temperature (T_{env}) of the same level: $\Delta T \equiv CTT - T_{env}$. Figure 3.7 presents the fraction of convection with positive buoyancy as a function of CTH from 6 km to 18 km for both new and old method[5]. Taking ΔT as a proxy showing how vigorous a convection is, Figure 3.7 suggests that tropical deep convection is statistically strongest when reaching 9-10 km and gradually loses momentum during further development due to the depletion of latent heat, entrainment of cold dry air, and overshooting the level of neutral buoyancy. These results can be explained by the observation of trimodal characteristics of tropical convection [*Johnson et al.*, 1999]. The smaller portion of positive buoyancy at CTH of 6 km is related to the existence of the weak stable layer, melting level at ~5 km. Many cumulus congestus do not glaciate fast enough and fail to gain enough thermal energy from latent heat release to sustain further upward motion. For the fast glaciating clouds, they are likely to gain the maximum apparent heat at 8 km [*Takayabu et al.*, 2010], get heated up during ascent, and achieve the strongest buoyancy at 9-10 km (~300 hPa). Because of this strong positive buoyancy, updraft motion is likely to continue and a local minimum of detrainment is thus expected, which is supported by Figure 3.6b in *Zuidema* [1998].

[5] The corresponding figure in *Wang et al*. [2011] included a programming error that lead to incorrect estimation of the ratio of positive buoyancy. That error has been fixed here.

The new IR non-blackbody correction method leads to more cases with positive cloud-top buoyancy for the very reason that the new correction is smaller than the old one thus resulting in warmer CTT estimates (Figure 3.6). Figure 3.7 shows that around 70% of the selected convective cores with tops lower than 10 km have positive buoyancy near cloud top, meaning that they will continue to accelerate. This result suggests that statistics collected from previous studies concerning convective clouds using polar-orbiting satellite data (i.e., snapshot observations) should be treated with caution. In particular, statistics on apparent cumulus congestus which have a lot of space to grow vertically (e.g., *Casey et al.* [2011]) should be reassessed in light of our study. Our results thus underscore the importance of interpreting satellite snapshot observations with the proper dynamic context, that is, convective life stages need to be considered. In parallel to *Wang et al.* [2011], further analysis was conducted that separates day-night overpasses and land-ocean cases. Four subgroups are shown in Figure 3.8: daytime over land, daytime over ocean, nighttime over land and nighttime over ocean. Qualitatively similar to the results in *Wang et al.* [2011], Figure 3.8 shows that larger diurnal cycle in convective buoyancy occurs over land than over ocean. The fraction of positive-buoyancy cases over land is larger at 1:30pm than that at 1:30am local time. This is consistent with our understanding of the diurnal cycle of tropical convection. The buoyancy achieves the maximum at ~10 km. The change of the ratio of positive buoyancy over ocean from 6 km to 10 km is smaller than that over land, possibly implying that melting level distributions over land and ocean and thus the distributions of latent heat release are different. *Yuan et al.* [2010] indicates that the levels where deep convective clouds are all in ice phase can be 2 km lower in altitude over ocean than over

land, suggesting that convective cloud could gain more latent heat in lower levels, shedding light on the smaller changes of the ratio from 6 to 10 km over ocean in Figure 3.8 especially the one at 1:30pm. For both 1:30am and 1:30pm curves in Figure 3.8, the increase of fraction of plumes with positive buoyancy from 6 km to 8 km CTH is much larger over ocean than over land. This is consistent with the previous findings by *Yuan et al.* [2010] that land convection seldom glaciates at -15^{o}C while ocean convection might do.

3.6. Conclusions

A new method is presented to estimate cloud top temperature of convective clouds by correcting for the non-blackbody effect based on a relationship between cloud-top fuzziness (CTF; defined as the vertical distance between CTH and 10dBZ ETH) and the distance from cloud top to the cloud IR effective emission level. Figures 3.3 and 3.4 show the dependences of cloud top radiative features on the CTF derived from both observations and radiative transfer model simulations. Using CTF measured by CloudSat cloud profiling radar together with the IR brightness temperature (BT_{11}) from MODIS, the algorithm provides an estimate of the temperature of cloud top. Comparisons are made with previous studies using the same data sets but a simple and less physically-based method to correct for the non-blackbody effect. The new method is shown to outperform the old one. The major findings are summarized as follows:

(1) Based on explicit radiative transfer model calculations, the mean effective emission level is at IR optical depth (τ_{11}) of 0.72, lower than often assumed in

atmospheric radiation lectures, which is 1. Among 16,837 cases examined, 99.4% of the effective emission level are in the range of τ_{11} at 0-2.

(2) A regression relationship is developed that can parameterize the non-blackbody correction as a function of cloud-top fuzziness measured by CloudSat radar reflectivity profiles.

(3) Using PCRTM, IWC and LWC retrievals from CloudSat and CALIPSO, and ECMWF reanalysis datasets, we can largely reproduce the observed BT_{11} by MODIS, lending support to the validity of our method.

This new non-blackbody correction was applied to re-evaluate convective cloud-top buoyancy as have previously been studied by *Luo et al.* [2010] and *Wang et al.* [2011]. Results show that ~70% of the convective clouds observed by CloudSat as snapshot in the height range of 6-10 km (i.e., apparent cumulus congestus) have positive buoyancy near cloud top, implying that they will continue to grow. This result underscores the importance of interpreting satellite snapshot observations as derived from polar-orbiting satellites with caution and proper dynamic context. Since apparent cumulus congestus have a lot of vertical space to grow, previous statistics on this cloud type using snapshot observations should be reassessed. It should be noted that the information on cloud development are inferred from thermodynamic analysis (buoyancy analysis). To rigorously validate such inferences, an independent observation with high temporal resolution would be needed. Possible candidates for such observations include, but not limited to, continuous ARM ground radar observations, geostationary imagery in the window channels, and multi-angle imaging spectroradiometer (MISR) measurements which observe the same cloud from different angles within a short time period. This

study is a proof-of-concept study and such thorough and rigorous validations are beyond the scope of it. However, the validation is a focus of our follow-up studies.

Finally, it is worth mentioning the uncertainties associated with our analysis. This new non-blackbody correction is based on fusion of multiple data sets, including satellite observations and retrievals as well as cloud-resolving model simulations. Thus, it is inevitably affected by the uncertainties and errors associated with these inputs. We described the uncertainties in the CloudSat retrievals and explained the choices we made in face of them. We estimated some aspects of the uncertainties using Monte-Carlo methods. However, to thoroughly and quantitatively pinpoint all uncertainties and to assess their impacts are beyond the scope of this study. This is especially true for the uncertainties of the parameters used in the cloud microphysics scheme of the GCE model. It would take tremendous computational effort to assess the full impact of the perturbations in these parameters. We acknowledge these limitations, but at the same time stress the improvement of the new non-blackbody correction method in helping estimate the cloud-top temperatures. The merit of data fusion in the cloud remote sensing and analysis is also noted.

3.7 Acknowledgement

The CloudSat data were obtained from the CloudSat Data Processing Center. The MODIS data were obtained from NASA Goddard DISC. The ECMWF interim data used in this study were obtained from http://data.ecmwf.int/data/. We thank all three reviewers for their insightful and thorough comments which greatly improve the clarity of the article. This research is supported by the NASA MAP project under grant NNX09AJ46G awarded to the University of Michigan and the NASA CloudSat/CALIPSO Science Team under grant NNX10AM31G and SEAC4RS Science Team under grant NNX12AC13G awarded to the City University of New York (CUNY).

References:

Casey, S. P. F., E. J. Fetzer, and B. H. Kahn (2012), Revised identification of tropical oceanic cumulus congestus as viewed by CloudSat, *Atmos. Chem. Phys.*, 12, 1587–1595.

Deng, M., G. G. Mace, Z. Wang, and H. Okamoto (2010), Tropical Composition, Cloud and Climate Coupling Experiment validation for cirrus cloud profiling retrieval using CloudSat radar and CALIPSO lidar, *J. Geophys. Res.*, 115, D00J15.

Deng, Min, Gerald G. Mace, Zhien Wang, R. Paul Lawson (2013), Evaluation of Several A-Train Ice Cloud Retrieval Products with In Situ Measurements Collected during the SPARTICUS Campaign, *J. Appl. Meteor. Climatol.*, 52, 1014–1030.

Goody, R. M., and Y. L. Yung (1989), *Atmospheric Radiation: Theoretical Basis*. Oxford University Press, 519 pp.

Haynes, J.M., R.T. Marchand, Z. Luo, A. Bodas-Salcedo, and G.L. Stephens (2007), A multi- purpose radar simulation package: QuickBeam, *Bull. Amer. Meteor. Soc.*, 88, 1723-1727.

Jensen, E. J., O. B. Toon, H. B. Selkirk, J. D. Spinhirne, and M. R. Schoeberl (1996), On the formation and persistence of subvisible cirrus clouds near the tropical tropopause, *J. Geophys. Res.*, 101, 21361–21375.

Johnson, R. H., T. M. Rickenbach, S. A. Rutledge, P. E. Ciesielski, W. H. Schubert (1999), Trimodal Characteristics of Tropical Convection, *J. Climate*, 12, 2397–2418.

King, M. D., Y. Kaufman, W. P. Menzel, and D. Tanré (1992), Remote sensing of cloud, aerosol, and water vapor properties from the moderate resolution imaging spectroradiometer (MODIS), *IEEE Trans. Geosci. Remote Sens.*, 30, 2–27.

Klemp J. B., and R. B. Wilhelmson (1978), The simulation of three-dimensional convective storm dynamics, *J. Atmos. Sci.*, 35, 1070–1096.

Lang, S., W.-K. Tao, J. Simpson, and B. Ferrier (2003), Modeling of convective–stratiform precipitation processes: Sensitivity to partitioning methods, *J. Appl. Meteor.*, 42, 505–527.

Liu, Guosheng, Judith A. Curry (1998), Remote Sensing of Ice Water Characteristics in Tropical Clouds Using Aircraft Microwave Measurements, *J. Appl. Meteor.*, 37, 337–355.

Liu, X., Zhou, D. K., Larar, A. M., Smith, W. L., Schluessel, P., Newman, S. M., Taylor, J. P., and Wu, W. (2009), Retrieval of atmospheric profiles and cloud properties from IASI spectra using super-channels, *Atmos. Chem. Phys.*, 9, 9121-9142.

Liu, X., W. L. Smith, D. K. Zhou, and A. Larar (2006), Principal component-based radiative transfer model for hyperspectral sensors: Theoretical concept, *Appl. Opt.*, 45, 201–209.

Luo, Y., R. Zhang, W. Qian, Z. Luo, X. Hu (2011), Inter-comparison of deep convection over the Tibetan Plateau-Asian Monsoon Region and subtropical North America in boreal summer using CloudSat/CALIPSO data, *J. Climate*, 24, 2164-2177.

Luo, Z., and W. B. Rossow (2004), Characterizing Tropical Cirrus Life Cycle, Evolution, and Interaction with Upper-Tropospheric Water Vapor Using Lagrangian Trajectory Analysis of Satellite Observations, *J. Climate*, 17, 4541–4563.

Luo, Z., G. Y. Liu, and G. L. Stephens (2008), CloudSat adding new insight into tropical penetrating convection, *Geophys. Res. Letts.*, 35, L19819.

Luo, Z., G. Y. Liu, and G. L. Stephens (2010), Use of A-Train data to estimate convective buoyancy and entrainment rate, *Geophys. Res. Letts.*, 37, L09804.

May, P. T., J. H. Mather, G. Vaughan, K. N. Bower, C. Jakob, G. M. McFarquhar, G. G. Mace (2008), The Tropical Warm Pool International Cloud Experiment, *Bull. Amer. Meteor. Soc.*, 89, 629–645.

McGill, M. J., L. Li, W. D. Hart, G. M. Heymsfield, D. L. Hlavka, P. E. Racette, L. Tian, M. A. Vaughan, and D. M. Winker (2004), Combined lidar-radar remote sensing: Initial results from CRYSTAL-FACE, *J. Geophys. Res.*, 109, D07203.

Minnis, P., P. W. Heck, and E. F. Harrison (1990), The 27–28 October 1986 FIRE IFO Cirrus Case Study, Cloudy parameter relationships derived from satellite and Lidar data, *Mon. Wea. Rev.*, 118, 2426–2447.

Minnis, P., C. R. Yost, S. Sun-Mack, and Y. Chen (2008) Estimating the top altitude of optically thick ice clouds from thermal infrared satellite observations using CALIPSO data, *Geophys. Res. Lett.*, 35, L12801.

Minnis, P., et al. (2012), Simulations of Infrared Radiances over a Deep Convective Cloud System Observed during TC4: Potential for Enhancing Nocturnal Ice Cloud Retrievals, *Remote Sens.*, 4, 3022-3054.

Niu, J. G., Y. Ping, H. L. Huang, J. E. Davies, J. Li, B. A. Baumc, and Y. X. Hu (2007), A fast infrared radiative transfer model for overlapping clouds, *J. Quant. Spectros. Radiat. Transfer*, 103, 447–459.

Okamoto, H., S. Iwasaki, M. Yasui, H. Horie, H. Kuroiwa, and H. Kumagai (2003), An algorithm for retrieval of cloud microphysics using 95-GHz cloud radar and lidar, *J. Geophys. Res.*, 108, 4226.

Paul, M. W., et al. (2008), MODIS Global Cloud-Top Pressure and Amount Estimation: Algorithm Description and Results, *J. Appl. Meteor. Climatol.*, 47, 1175–1198.

Platnick, S., M. D. King, S. A. Ackerman, W. P. Menzel, B. A. Baum, J. C. Riedi, and R. A. Frey (2003), The MODIS cloud products: Algorithms and examples from Terra, *IEEE Trans. Geosci. Remote Sens.*, 41, 459–473.

Fu, Qiang (1996), An Accurate Parameterization of the Solar Radiative Properties of Cirrus Clouds for Climate Models, *J. Climate*, 9, 2058–2082.

Rossow, W. B., A. W. Walker, D. E. Beuschel, and M. D. Roiter (1996), *International Satellite Cloud Climatology Project (ISCCP) Documentation of New Cloud Datasets*, WMO/TD 737, World Climate Research Programme, Geneva, Switzerland.

Sassen, K., Z. Wang, and D. Liu (2009), Cirrus clouds and deep convection in the tropics: Insights from CALIPSO and CloudSat, *J. Geophys. Res.*, 114, D00H06.

Segelstein, D. J. (1981), The complex refractive index of water, Master's thesis, University of Missouri-Kansas City.

Sherwood, S. C., J.-H. Chae, P. Minnis, and M. McGill (2004), Underestimation of deep convective cloud tops by thermal imager, *Geophys. Res. Lett.*, 31, L11102.

Skofronick-Jackson, Gail M., James R. Wang (2000), The Estimation of Hydrometeor Profiles from Wideband Microwave Observations*, J. Appl. Meteor.*, 39, 1645–1656.

Soong, S-T, Y. Ogura (1980), Response of trade wind cumuli to large-scale processes, *J. Atmos. Sci.*, 37, 2035–2050.

Stamnes, K., S. C. Tsay, W. Wiscombe, and K. Jayaweera (1988), A numerically stable algorithm for discrete-ordinate-method radiative transfer in multiple scattering and emitting layered media, *Appl. Opt.*, 27, 2502–2509.

Stephens, G. L. (1994), *Remote Sensing of the Lower Atmosphere: An Introduction*, Oxford University Press, 544 pp.

Stephens, G. L., et al. (2002), The CloudSat mission and the A-Train: A new dimension of space-based observations of clouds and precipitation, *Bull. Amer. Meteor. Soc.*, 83, 1771–1790.

Stephens, G. L., et al. (2008), CloudSat mission: Performance and early science after the first year of operation, *J. Geophys. Res.*, 113, D00A18.

Takayabu, Y. N., S. Shige, W.-K. Tao, N. Hirota (2010), Shallow and Deep Latent Heating Modes over Tropical Oceans Observed with TRMM PR Spectral Latent Heating Data, *J. Climate*, 23, 2030–2046.

Tao, W.-K., and J. Simpson (1993), Goddard Cumulus Ensemble model: Part I. Model description, *Terr. Atmos. Oceanic Sci.*, 4, 35–72.

Tao, W. K., et al. (2002), Microphysics, radiation and surface processes in the Goddard Cumulus Ensemble (GCE) model, *Meteorol. Atmos. Phys.*, 82, 97–137.

Wang, C., Z. J. Luo, and X. Huang (2011), Parallax correction in collocating CloudSat and Moderate Resolution Imaging Spectroradiometer (MODIS) observations: Method and application to convection study, *J. Geophys. Res.*, 116, D17201.

Warren, S. G. (1984), Optical constants of ice from the ultraviolet to the microwave, *Appl. Optics*, 23, 1206–1225.

Wei, H., P. Yang, J. Li, B. A. Baum, H.-L. Huang, S. Platnick, Y. Hu, and L. Strow (2004), Retrieval of semitransparent ice cloud optical thickness from Atmospheric Infrared Sounder (AIRS) measurements, *IEEE Trans. Geosci. Remote Sens.*, 42, 2254–2267.

Winker, D. M., M. A. Vaughan, A. H. Omar, Y. Hu, K. A. Powell, Z. Liu, W. H. Hunt, and S. A. Young (2009), Overview of the CALIPSO mission and CALIOP data processing algorithms, *J. Atmos. Oceanic Technol.*, 26, 2310–2323.

Wood, N. (2008), Level 2B Radar-Visible Optical Depth Cloud Water Content (2B-CWC-RVOD) Process Description Document. Version: 5.1, 23 October 2008.

Xiong, X., B. N. Wenny, A. Wu; W. L. Barnes (2009), MODIS Onboard Blackbody Function and Performance, *Geoscience and Remote Sensing, IEEE Transactions on* , 47, 4210-4222.

Yang, P., B. Gao, B. A. Baum, Y. X. Hu, W. J. Wiscombe, S. Tsay, D. M. Winker, and S. L. Nasiri (2001), Radiative properties of cirrus clouds in the infrared (8–13 μm) spectral region, *J. Quant. Spectrosc. Radiat. Transfer*, 70, 473–504.

Young, A. H., J. J. Bates, and J. A. Curry (2012), Complementary use of passive and active remote sensing for detection of penetrating convection from CloudSat, CALIPSO, and Aqua MODIS, *J. Geophys. Res.*, 117, D13205.

Yuan, T., J. V. Martins, Z. Li, and L. A. Remer (2010), Estimating glaciation temperature of deep convective clouds with remote sensing data, *Geophys. Res. Lett.*, 37, L08808.

Zeng, X., W.-K. Tao, M. Zhang, A. Y. Hou, S. Xie, S. Lang, X. Li, D. Starr, X. Li, and J. Simpson (2009), An indirect effect of ice nuclei on atmospheric radiation, *J. Atmos. Sci.*, 66, 41-61.

Zeng, X., W.-K. Tao, S. W. Powell, R. A. Houze, P. Ciesielski, N. Guy, H. Pierce, T. Matsui (2013), A Comparison of the Water Budgets between Clouds from AMMA and TWP-ICE, *J. Atmos. Sci.*, 70, 487–503.

Zuidema, P. (1998), The 600–800-mb Minimum in Tropical Cloudiness Observed during TOGA COARE, *J. Atmos. Sci.*, 55, 2220–2228.

Chapter 4

Interpretation of convective cloud top buoyancy derived from satellite observations

Part of the material in this chapter was published in

Wang, C.P., Z. Luo, X.L. Huang, Parallax Correction in Collocating CloudSat and MODIS Observations: Method and Application to Convection Study, *JGR-Atmospheres*, 116, D17201, doi:10.1029/2011JD016097, 2011.

Wang, C., Z. J. Luo, X. Chen, X. Zeng, W.-K. Tao, and X. Huang, 2014: A physically based algorithm for non-blackbody correction of cloud top temperature and application to convection study, *J. Appl. Meteor. Climatol.*, in press, doi: http://dx.doi.org/10.1175/JAMC-D-13-0331.1.

4.1 Introduction

A simple yet meaningful question to ask regarding observing convective clouds is whether the observed convective cloud will continue to rise or cease to grow after the measurement is made. This is not easy to answer given that no satellites so far are able to

provide measurements of the vertical motion of clouds at desired temporal resolutions. Geostationary satellite can provide limited information on this regard by high temporal-resolution imaging of the IR window channel [*Zuidema et al.*, 2012]. *Luo et al.* [2010] proposed to use a thermodynamic variable, cloud top buoyancy, to evaluate the tendency of convective development. Convections with positive buoyancy indicate positive acceleration and thus will continue to grow vertically, usually termed as "transient convections". Those with negative buoyancy will be decelerated and thus deemed as "terminal convections". Therefore, cloud top buoyancy, if available, can be used as a proxy for the evolution of convective clouds.

To illustrate this idea, Figure 4.1 presents nearly simultaneous snapshot by CloudSat, AIRS, and MODIS. CloudSat and MODIS have been introduced in Chapter 2. AIRS (Atmospheric Infrared Sounder) is an IR grating spectrometer, from which the temperature and humidity profiles can be retrieved at 1-km and 2-km vertical resolutions, respectively [*Chahine et al.*, 2006]. CloudSat radar reflectivity map in Figure 4.1a and MODIS visible-band image Figure 4.1b show four convective clouds along the CloudSat track. These two images are snapshots from which no conclusion can be drawn on the tendency of vertical motion. Figure 4.1c shows the AIRS-retrieved temperature map at 7-km altitude, roughly the top height of convective clouds shown in Figure 4.1a. Along the CloudSat track in Figure 4.1c, the retrieved temperature can tell whether convective cloud is warmer or colder than ambient at this altitude, which in turn can tell whether buoyancy is positive or negative and thus the vertical tendency is positive or negative. This example stresses how such study of thermodynamic variables can provide dynamic information based on the static measurements of multiple satellite sensors.

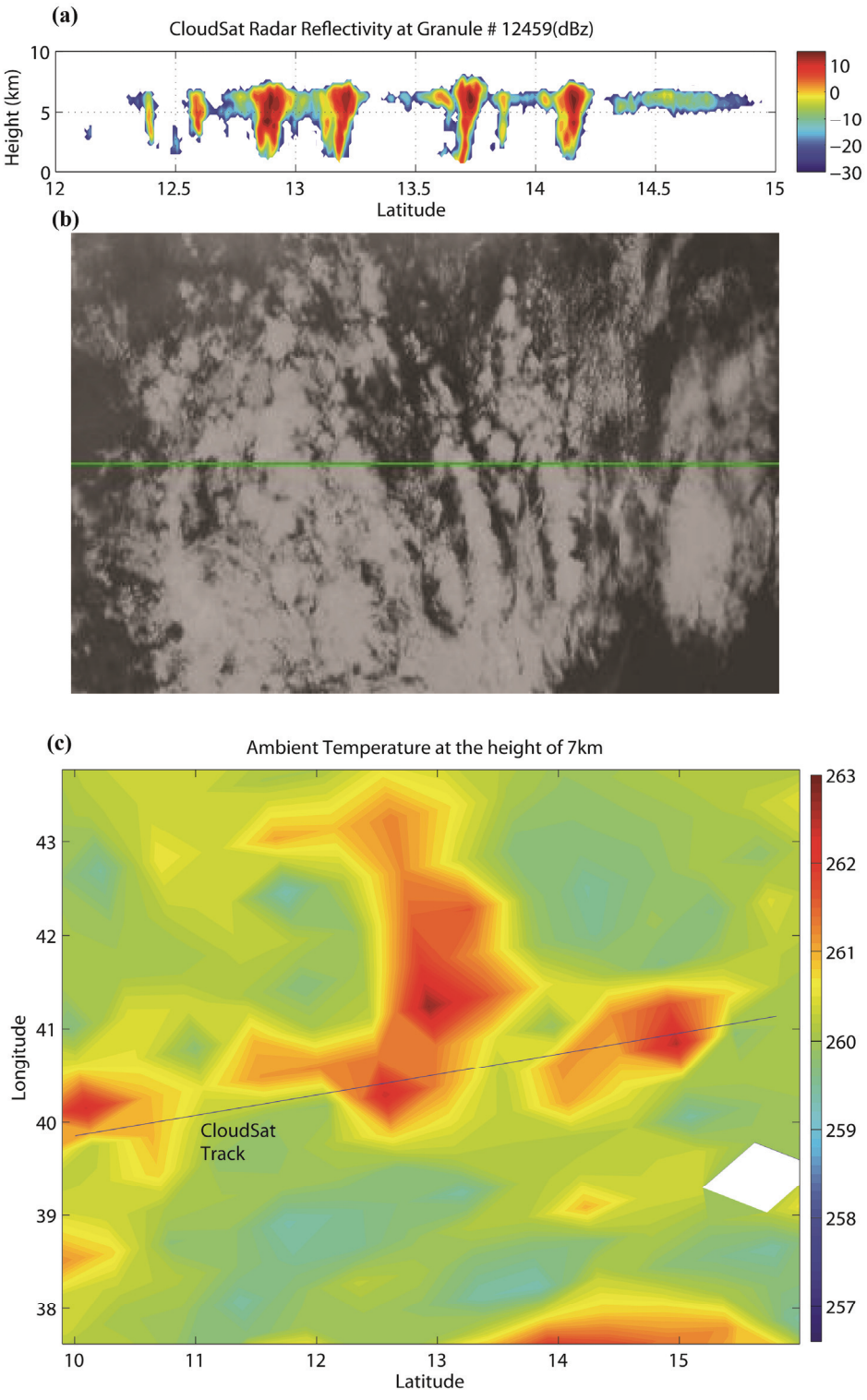

Figure 4.1. Observation at Sep 10, 2008 at 01:54UTC. (a) CloudSat radar reflectivity. (b) MODIS visible image. (c) 7-km temperature retrieval from AIRS aboard Aqua. The straight lines in (b) and (c) indicates the CloudSat track as in (a).

Ideally, the buoyancy force throughout the vertical extent of convective clouds should be studied in order to obtain a full view of the dynamic developments of convective clouds. Yet a practical limitation is that IR measurement such as those by AIRS and MODIS cannot penetrate optically thick clouds such as convective clouds. Thus, in this study we shall focus on cloud top buoyancy only and the vertical velocity at cloud top accordingly. As illustrated in Chapter 3, window-channel brightness temperature (e.g., BT_{11}) is related to temperatures within a vertical layer near the cloud top. Thickness of the layer roughly depends on the water content of the cloud top. A developing convection usually has a compact cloud top with large water content and a dissipating convection tends to have a relatively tenuous cloud top. Chapter 3 derives an empirical relationship between cloud top-layer vertical structure and the thickness of the layer by physically linking two quantities: cloud top fuzziness and cloud top emission level, from which the physical temperature of cloud top can be inferred. This physical cloud top temperature will be analyzed in this chapter in conjunction with ambient temperature to further exploit the possibility of deriving cloud top buoyancy.

Cloud top buoyancy can be derived once cloud top temperature and ambient temperature are known. According to the momentum equation, the vertical velocity (ω) is governed by,

$$\frac{d\omega}{dt} = -\frac{1}{\bar{\rho}}\frac{\partial p'}{\partial z} - g\left(\frac{\rho'}{\bar{\rho}}\right) \tag{4.1}$$

where P and ρ are air parcel pressure and density. As usual, overbars indicate the hydrostatic mean state and primes indicate deviation from the mean state. The first term on the right is non-hydrostatic pressure gradient acceleration that usually arises from

dynamical effects of forced motion. This term is pronounced only when the speed of the motion is comparable to or surpasses the speed of sound. The vertical velocity of convective updraft is usually no more than 20 m/s [*Guimond* 2010], one order of magnitude smaller than the speed of sound in the atmosphere. Therefore, this term is negligible in our analysis. The second term on the right is the buoyancy acceleration caused by density anomalies. Given that the pressure perturbation is small compared with temperature and density perturbation [*Emanuel*, 1994], the buoyancy term can be expressed as,

$$B = -g\left(\frac{\rho'}{\overline{\rho}}\right) \approx g\frac{T'}{T} \tag{4.2}.$$

To generalize this expression for moist air, the temperature is replaced by virtual temperature, T_v, which is defined as,

$$T_v = T(1 + 0.61\,\mathrm{q}_v) \tag{4.3}$$

where q_v is mixing ratio of water vapor. Then Equation 4.2 can be written as,

$$B = g\frac{T_v'}{T_v} \tag{4.4}$$

To evaluate the contribution of water vapor in this formula, Equation 4.4 is expanded into two terms: one only a function of temperature and the other only of moist content.

$$B \approx g\left(\frac{T'}{T} + 0.61 q_v'\right) \tag{4.5}$$

From the satellite remote sensing perspective, the first term $\left(T'/T\right)$ could be evaluated at the cloud top but not inside cloud due to the reasons mentioned above. The

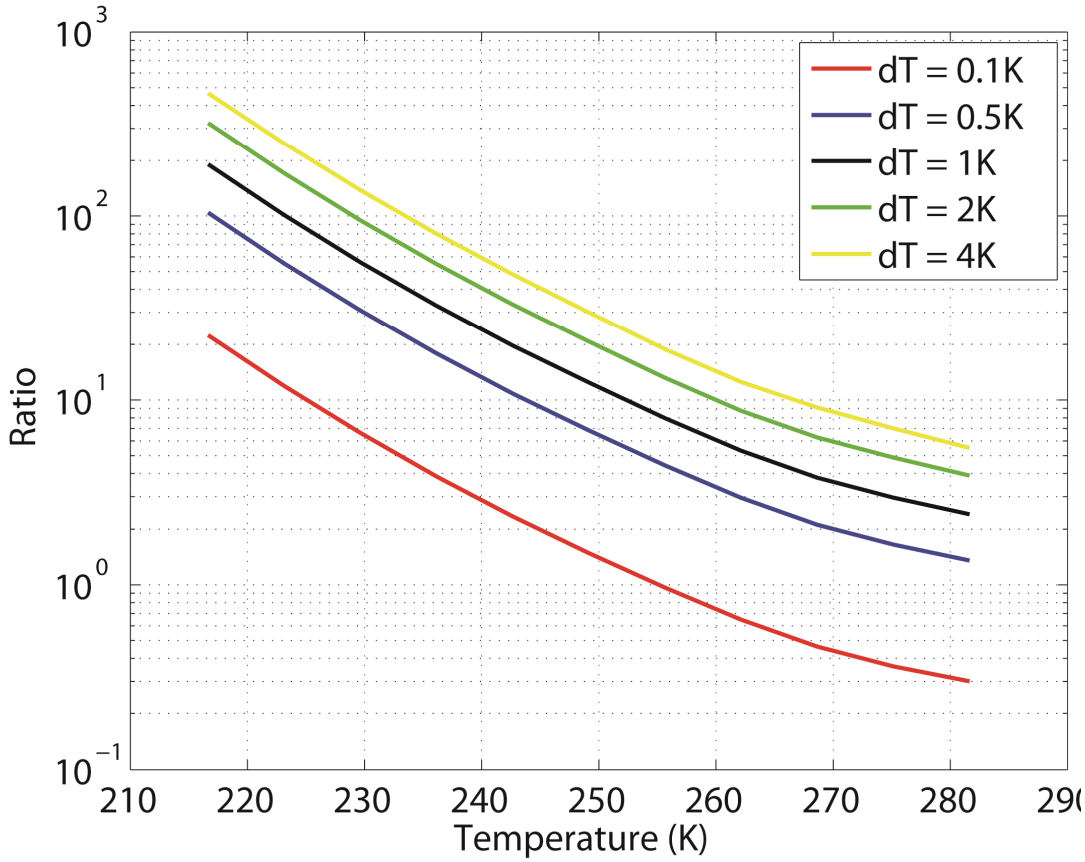

Figure 4.2. The figure shows the ratio of the first and second terms in Equation 4.1, $\frac{T'}{T}\Big/0.61q_v'$, for different cloud top temperature. The in-cloud and ambient temperature difference is assumed to be dT.

second term, $0.61q_v'$, is the perturbation to water vapor mixing ratio. The ratio between the first and second term, $\frac{T'}{T}\Big/0.61q_v'$, is computed using the 1976 US Standard Atmosphere [*National Oceanic and Atmospheric Administration et al.*, 1976] with different temperature perturbation (Figure 4.2). Air near cloud top is assumed saturated. Ambient relative humidity is empirically set to 80% at the altitude of 1 km and linearly decreases to 30% at the tropopause. For deep convection above the freezing level and temperature perturbation as large as 2 K, the buoyancy is dominantly determined by the

temperature perturbation. In comparison, the cloud-top buoyancy at the mid-troposphere is equally affected by both terms. Thus, cloud top buoyancy (CTB) is defined as,

$$CTB = CTT(1 + 0.61q_{v\_cld}) - T_{env}(1 + 0.61q_{v\_env}) \tag{4.5}$$

where CTT represents cloud top temperature, T_{env} is the environmental temperature at the same level of cloud top height (CTH), q_{v_cld} and q_{v_env} are water vapor mixing ratio inside and outside cloud, respectively. To be able to evaluate Equation 4.5, minimum observational requirements are independent, simultaneous measurements of CTT and CTH as well as ambient air sounding. CloudSat and MODIS aboard Aqua are flying in formation and separated by only ~2 min, making them an ideal combination for this purpose. Based on the results from Chapter 2 and 3, CTT is obtained by,

$$CTT = BT_{11} - \Gamma_m \min(\frac{CTF + 0.22}{2.83}, 0.74) + 0.11 \tag{4.6}$$

where BT_{11} is the MODIS 11-μm brightness temperature in kelvin, Γ_m is the local moist adiabatic temperature in kelvin per kilometer, CTF = CTH - 10dBZ ETH as defined in Chapter 3 is cloud top fuzziness in kilometer.

4.2 Data description and composite strategy

39,123 tropical (30^oS~30^oN) convective clouds have been identified by CloudSat measurements in 2008. As in previous chapters, shallow convection is not included in such identification. A convective cloud profile is defined as (1) cloud base below the height of 3 km, (2) at least one pixel with radar reflectivity great than 10dBZ, (3) vertical extent greater than 3 km. The cloud top heights of the convective cases are plotted in red histogram in Figure 4.3. The overlying black histogram is constructed by convective cases with high and relatively compact cloud tops (CTF < 4 km and CTH > 6km). This

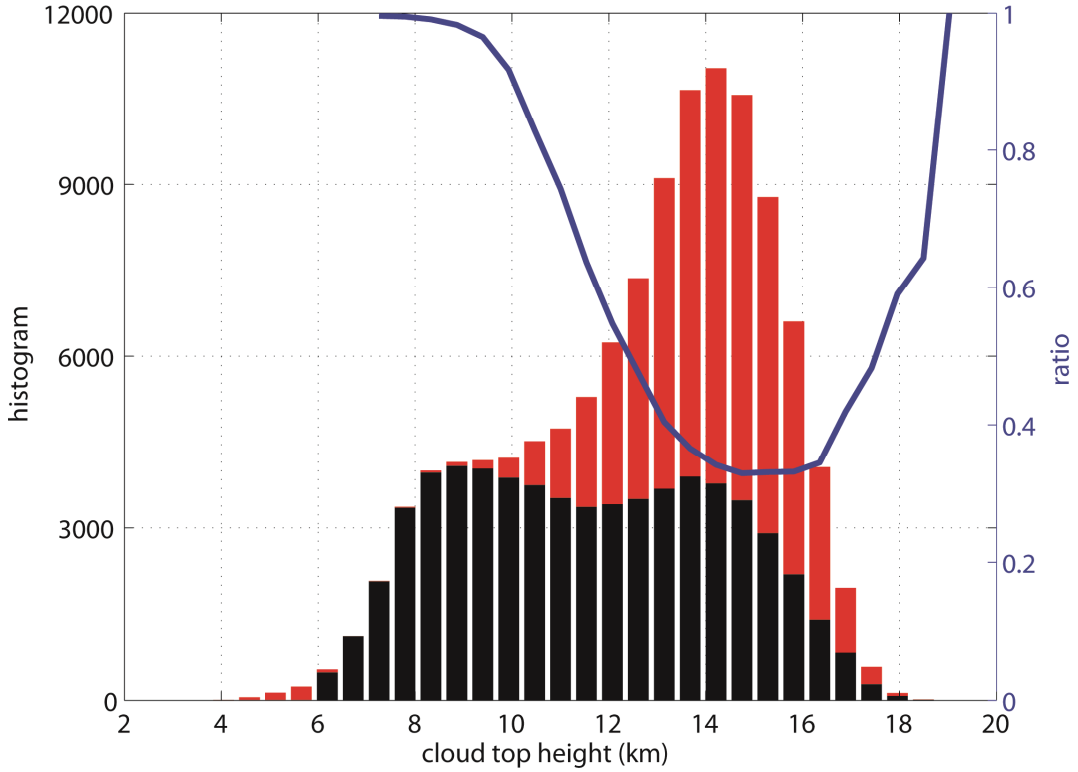

Figure 4.3. Histogram of tropical convective cloud top height observed by CloudSat in 2008 (red). Histogram of cloud top height of strong deep convection are shown in black. The blue curve is the ratio of the two.

subset of convection constitutes 54.4% of the total profiles identified by the CloudSat and represents relatively strong convection in its developing or mature phase instead of decay phase, hereafter, referred as active convection. The CTF criterion removes a large portion of identified profiles that have obviously fuzzy cloud tops with convective core well below saturated emission level (Chapter 3.3.1) and thus probably have lost upward momentum and quickly dissipating. This study attempts to illustrate cloud development using observations of cloud top condition, thus only the subset of active deep convection is used. A bimodal distribution is clearly identifiable in the black histogram with one

peak for cumulus congestus at 9 km and the other for deep convection at 14 km [*Johnson et al.*, 1999; the third mode of tropical convection, shallow convection, is excluded in such data filtering]. The blue curve shows the portion that is retained by the CTF criteria. The ratio remains close to unity until CTH reaches 9 km, quickly reduces to 0.33 at the CTH of 14.75~16.35 km where tropical tropopause lies, and then increases to one at the CTH of 19 km. There are 1,183, 1.9% of all identified cases, convective clouds with CTH beyond 16.35 km and the cloud top 8.2 K colder than the ambient air on average, indicating that this subset of clouds are likely the overshooting convections.

4.3 Observational result

4.3.1 Geographical distribution of tropical convective cloud top buoyancy observed by CloudSat

The aforementioned criteria are applied to dataset from 2007 to 2010 to get a long-term average of convective development at the time of CloudSat observations (i.e., local 1:30am/1:30pm). The numbers of occurrences in each 10^o by 10^o grid for the active convective clouds are plotted in Figure 4.4a. The Intertropical Convergence Zone (ITCZ), the South Pacific Convergence Zone (SPCZ), and the regions featured with marine stratus (thus with few deep convections) are all clearly identifiable.

Figure 4.4b shows the ratio of the number of cases at 1:30pm to that at 1:30am. Warm color lies mostly over land and cold color over ocean, illustrating the land-ocean contrast in convective diurnal cycle with amplitude around 3: deep convections over land tend to occur in the afternoon instead of in the midnight, while it is not the case over ocean [*Yang & Slingo*, 2001; *Tian et al.*, 2004; *Liu et al.*, 2008].

Diurnal statistics of the two convective modes mentioned in Figure 4.3 are depicted in Figures 4.5 and 4.6. The two modes are divided as cumulus congestus with CTH of 7~9 km and deep convection with CTH of 13~14 km. Figure 4.5a (4.5b) shows the ratio of positive buoyancy (defined as positive CTB) for cumulus congestus at 1:30pm (1:30am) local time. Cumulus congestus are vigorously growing over most parts of the tropics at 1:30pm. At 1:30am, the situation is about the same except over land, which is highlighted by the ratio of the two. Spatial maps of the ratio of positive buoyancy for deep convection mode are plotted in Figure 4.6. Diurnal contrast over land is as obvious as the case of cumulus congestus. A notable difference from Figure 4.5 is that, over considerable part of oceans, the ratio of 1:30pm to 1:30am is larger, suggesting more occurrence of active growth of deep convection over oceans at 1:30pm than 1:30am. Over marine continent, both cumulus congestus and deep convection shows strong diurnal difference in ratios of positive buoyancy however the occurrence frequency in Figure 4.4b remains largely the same between 1:30am and 1:30pm.

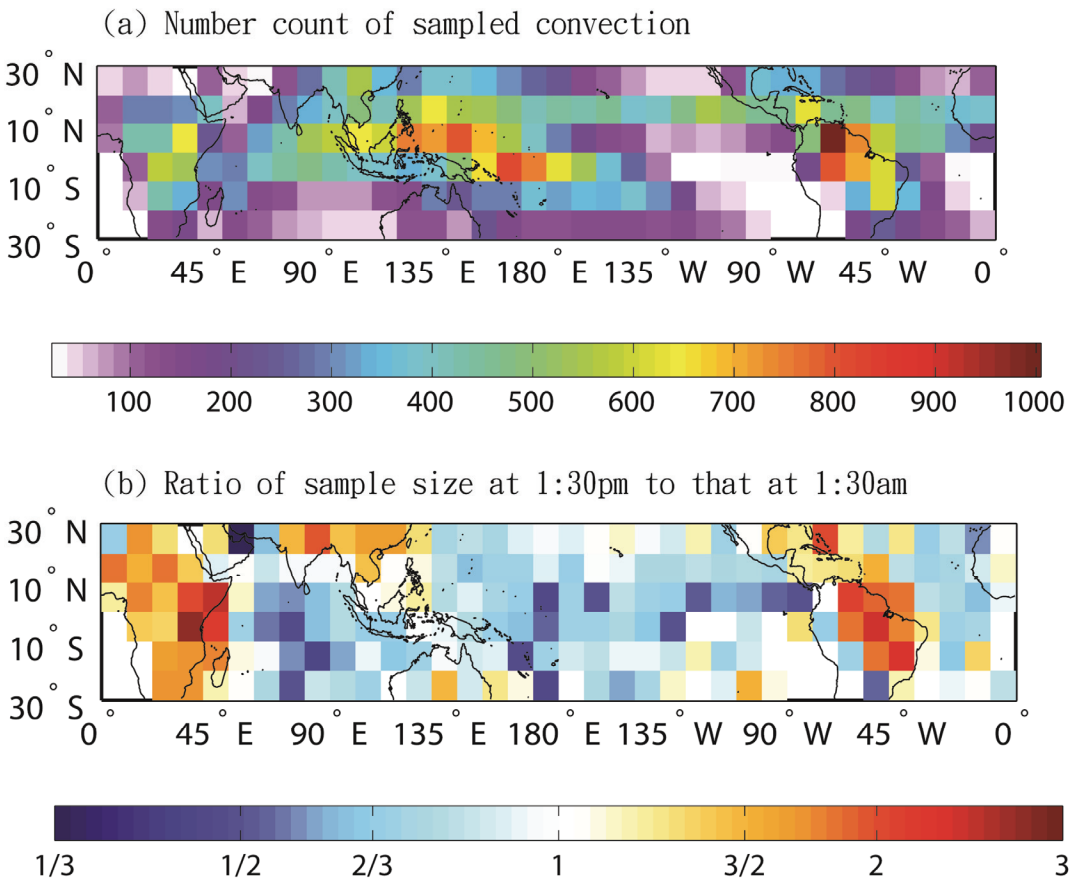

Figure 4.4 (a) Geographic distribution of total number of active deep convective clouds (including cumulus congestus) in 10^o by 10^o grid boxes observed by CloudSat during 2007-2010. (b) The ratio of number of occurrences at 1:30pm to at 1:30am.

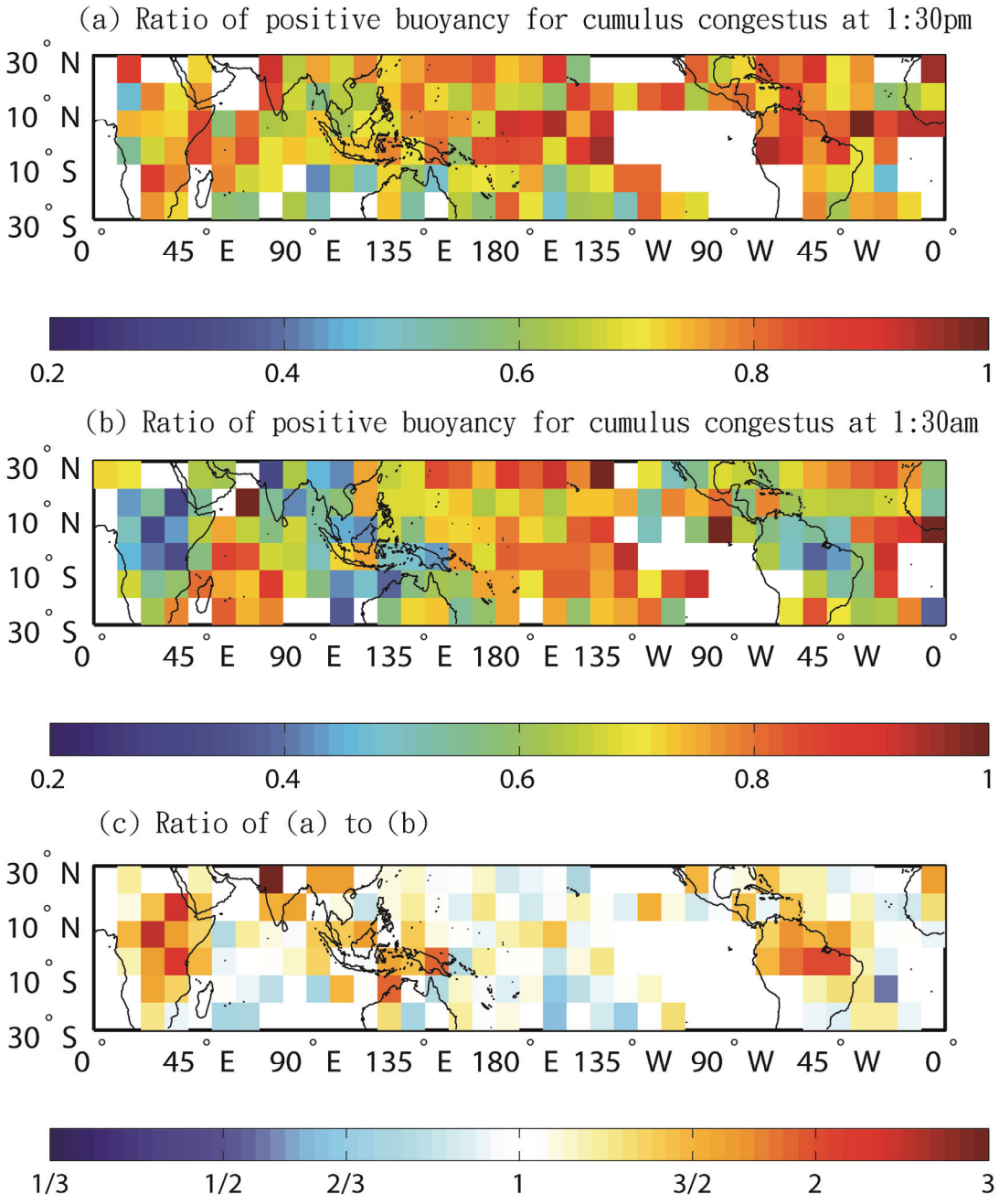

Figure 4.5 Geographic distribution of ratio of positive CTB for convective cloud with CTH between 7 km and 9 km (so-called cumulus congestus mode) in 10^o by 10^o grid boxes. The result is plotted for 1:30pm in (a) and 1:30am in (b). The ratio of (a) to (b) is shown in (c).

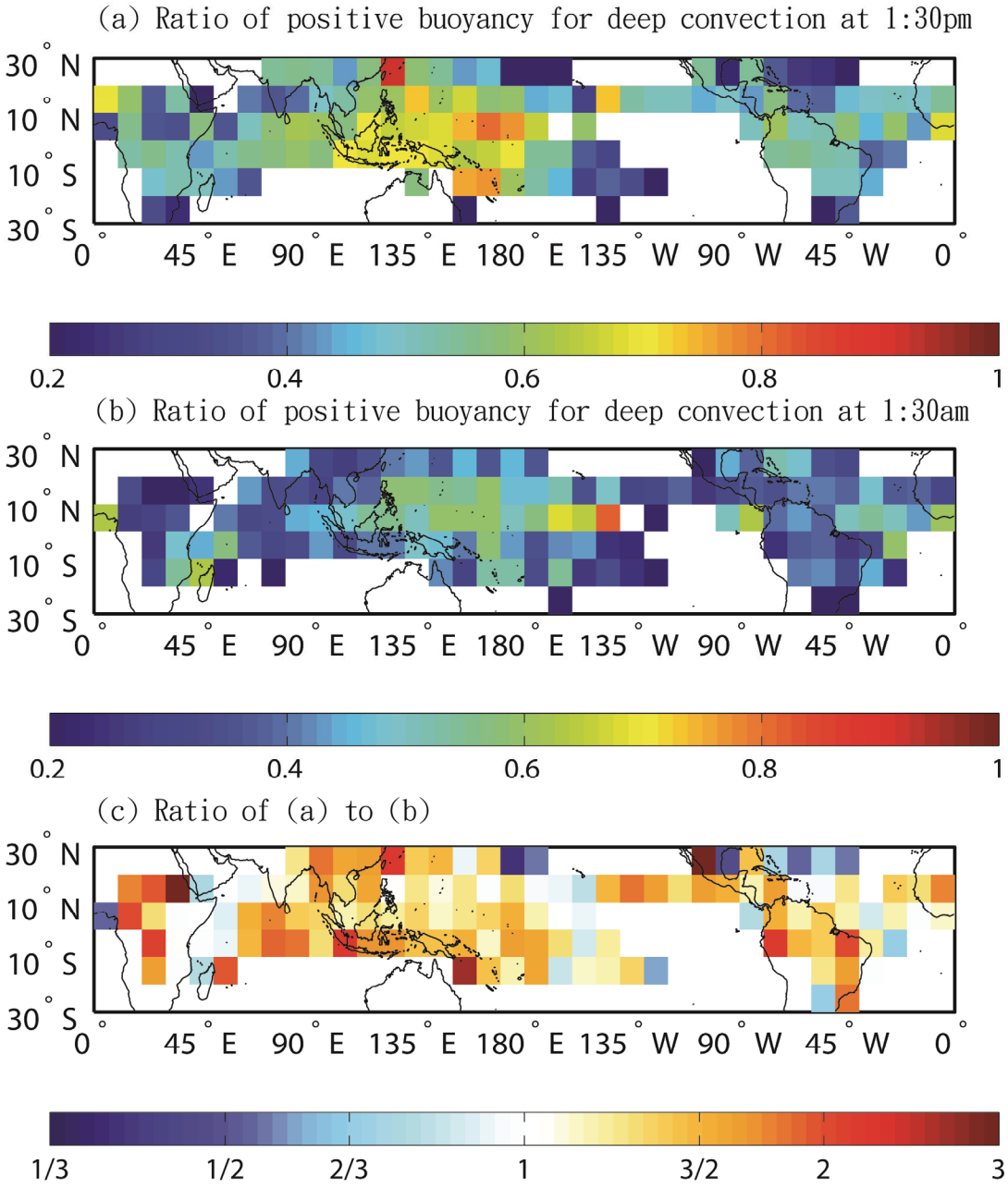

Figure 4.6 Geographic distribution of ratio of positive CTB for convective cloud with CTH between 13 km and 15 km (so-called deep convection mode) in 10^o by 10^o grid boxes. The result is plotted for 1:30pm in (a) and 1:30am in (b). The ratio of (a) to (b) is shown in (c).

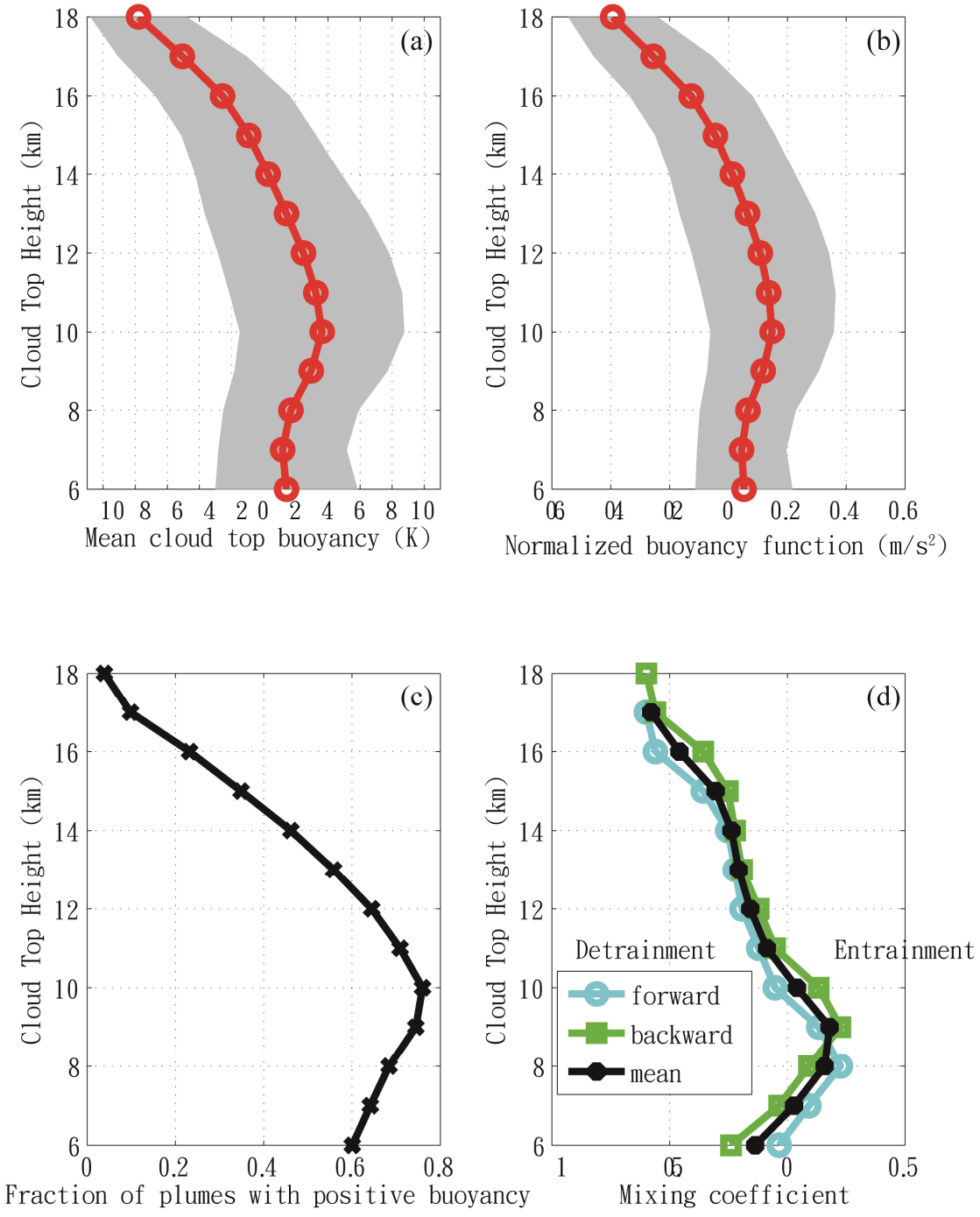

Figure 4.7. (a) Cloud top buoyancy as a function of cloud top height composited in 1-km layers. (b) normalized buoyancy function. (c) Fraction of plumes with positive buoyancy. (d) Mixing coefficient derived from (b).

4.3.2 Vertical Profile of cloud top buoyancy

Figure 4.7a shows the CTB derived from 2007-2010 CloudSat and MODIS observations as a function of CTH, which are averaged over the entire tropics and over each 1-km vertical layer. Shaded area represents the one-sigma uncertainty range. The CTB has a local maximum of 1.4 K at CTH of 6 km, then decreases to 1.2 K at 7 km and gradually increases to its maximum, 3.6 K, at 10km, and then monotonically decreases with CTH. The averaged CTB reaches neutral buoyancy (CTB=0) slightly above 14 km. Figure 4.7b normalizes CTB following

$$b(z) = \mathrm{g}\frac{CTB}{T_{env}(1+0.61q_{v\_env})} \tag{4.7}$$

Such normalized buoyancy is used later for comparison with modeling studies.

As in many applications of thermodynamics, we here take the ergodic hypothesis, i.e., assuming that buoyancy obtained at cloud top is the buoyancy for the fresh in-cloud air parcel when it reaches the same altitude of the cloud top. A helpful visualization is to imagine a convective tower constant sprouting of fresh in-cloud air (hereafter called "fountain-cloud"). Then, Figure 4.7a can be interpreted as the vertical profile of updraft parcel buoyancy for a representative tropical deep convective cloud from 6 km to 18 km. If so, the curvature of the CTB profile in Figure 4.7a implies the existence of two weak stable layers: the melting layer and the tropopause, which is consistent with our previous knowledge about the tropical stable layers in the free troposphere [*Zuidema*, 1998; *Johnson*, 1999].

Figure 4.7c shows the ratio of positive buoyancy as a function of CTH. The ratio has a maximum of 0.76 at 10 km and linearly decreases with CTH. Figure 4.7d show the

profiles of the mixing coefficients defined in *Folkins* [2009] from the thermodynamic perspective. The definition of mixing coefficient is,

$$\sigma_{backward} = \frac{b(\mathrm{i}) - \mathrm{b}(\mathrm{i}-1)}{b_{scale}} \tag{4.8a}$$

$$\sigma_{forward} = \frac{b(\mathrm{i}+1) - \mathrm{b}(\mathrm{i})}{b_{scale}} \tag{4.8b}$$

where σ is mixing coefficient, b_{scale} (=0.23 g/m^2) is the normalization factor from *Folkins* [2009]. The average of backward and forward results is shown in black in Figure 4.7d. The mixing coefficient can be interpreted as follows: In the updraft branch of a steady state, when an air parcel in the cloud experiences acceleration, by mass continuity ambient air must be entrained into cloud. When the air parcel decelerates, the cloud tends to detrain. Here, turbulent mixing is ignored so that detrainment and entrainment is governed solely by buoyancy vertical gradient.

The difference between Equation 4.8a and 4.8b lies in the forward difference and backward difference so a layer may have detrainment and entrainment at the same time like the level of 10 km. The weak detrainment at 6 km is consistent with model study [*Folkins*, 2009] and observation in during the Tropical Ocean Global Atmosphere Coupled Ocean–Atmosphere Response Experiment (TOGA COARE) field campaign [*Zuidema*, 1998]. Such weak detrainment at 6km can be explained by the melting layer. Cloud droplets do not readily freeze at 0^{o}C but can remain in liquid form at colder temperature in a "supercooled" state [*Rosenfeld & Woodley*, 2000]. Latent heat release due to the phase change is gradually released as indicated by the fraction of cloud droplets in liquid form (Figure 14 in *Korolev et al.* [2003]) which also implies that the

latent heat release rate varies with a number of factors, e.g., land-ocean contrast [*Yuan et al.*, 2010]. Comparing with Figure 14 in *Folkins* [2009] that is solely based on model simulation, Figure 4.7d strongly resembles the same pattern but the amplitude is 3~4 times larger, suggesting that the simulated convections in *Folkins* [2009] might not be as vigorous as the observed ones, which however is subject to the large uncertainty rage in Figure 4.7b.

The observation-derived mixing coefficient could shed light on entrainment/detrainment estimation. An updraft parcel of mass $m_{d,up}$ entrains a mass Δm_d of dry air from the background atmosphere when $\sigma > 0$ (increasing buoyancy) and detrains a mass Δm_d of dry air into the background atmosphere when $\sigma < 0$ (decreasing buoyancy). The change in mass Δm_d is calculated using σ by,

$$\sigma = \frac{\Delta m_d}{\Delta m_d + m_{d,up}} \tag{4.9}$$

Flying in Sun-synchronous orbits, A-Train measurements in the tropics are taken around 1:30 am and 1:30 pm local time. Although not sufficient to delineate the entire diurnal cycle, the measurement from the daytime (1:30 pm) and nighttime (1:30 am) overpasses can partially illustrate the diurnal differences. Figure 4.8 shows the mean cloud top buoyancy in the left panel and fraction of convective clouds with positive buoyancy in the right panel as a function of CTH, similar to Figure 4.7a and 4.7c but divided into four subgroups: daytime over land, daytime over ocean, nighttime over land, and nighttime over ocean. Figure 4.8 suggests that over land, statistics from 1:30am measurements are quite different from that at 1:30pm: both the mean CTB and the

averaged fraction of positively buoyant cases over land are much larger at 1:30pm than that at 1:30am. In contrast, the diurnal difference over the oceans is half of that over land beyond 10 km and significantly smaller below 10 km. This is consistent with current understanding of diurnal cycle of tropical convection [*Yang & Slingo*, 2001; *Tian et al.*, 2004; *Liu et al.*, 2008] and delineations of Figures 4.5 and 4.6. For both panels, the vertical profile over ocean is consistently close to the daytime profile over land, suggesting that convection over ocean is consistently more vigorous than nighttime convection over land and slightly less strong than the daytime ones. The sharp decrease of daytime land curve in right panel of Figure 4.8 at 6-km altitude is likely affected by the

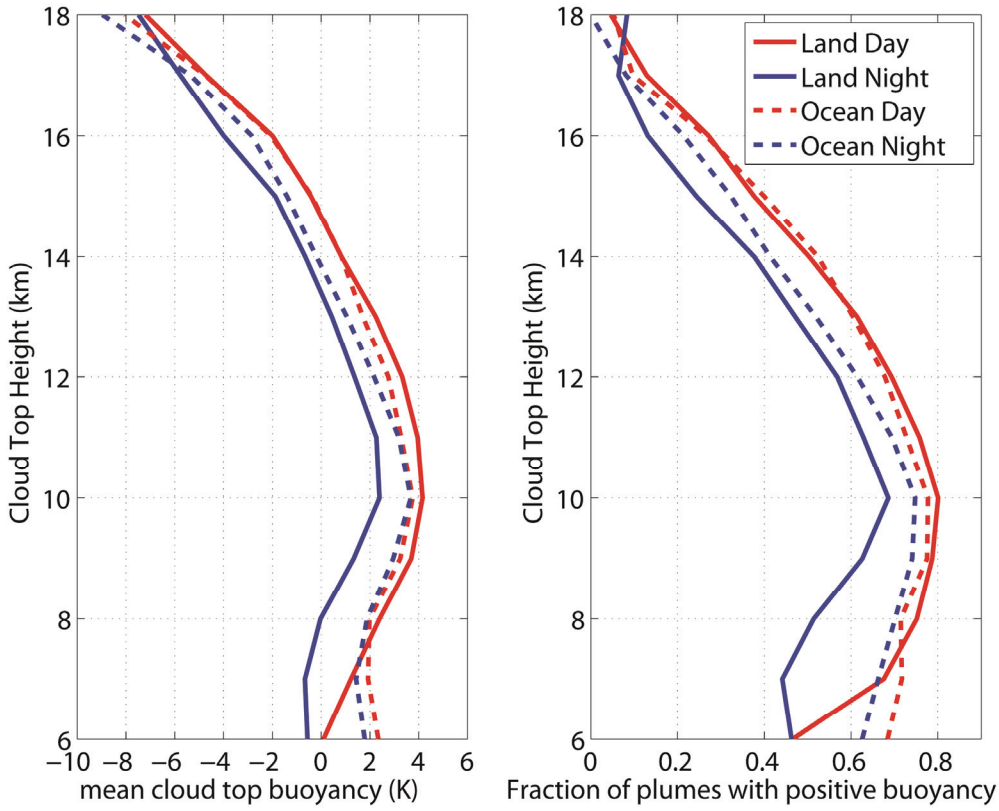

Figure 4.8. (Left) Similar to the Figure 4.7a except for four subgroups: daytime over land and ocean, nighttime over land and ocean. (Right) Similar to Figure 4.7c except for four subgroups.

small sample size at this level (Figure 4.3).

4.4 Estimation of vertical velocity using the cloud top buoyancy profile

4.4.1 Method description

Fountain-cloud assumption assumes cloud top of an active deep convection can indicate the inner thermodynamic condition. Thus cloud top vertical velocity can in principle be calculated based on vertical profile of cloud top buoyancy and other ancillary information. The method is based on *Gregory* [2001] and *Genio et al.* [2007]. A mathematical description of the method is as follows.

Starting from the vertical momentum equation, we have,

$$\frac{1}{2}\frac{\partial \overline{w}^2}{\partial z} = ag\overline{\left(\frac{T_v'}{\overline{T_v}} - l\right)} - b\delta\overline{w}^2 - \overline{w}^2\varepsilon \tag{4.10}$$

where l is liquid water mixing ratio, g is gravity, δ is detrainment rate, ε is entrainment rate, and *a* and *b* are constants. Here, l is assumed zero, which implies all condensates are removed upon formation. This assumption does not include the latent heat release during freezing because Equation 4.10 is a dynamic equation and phase change is not explicitly taken into account. Instead, the in-cloud virtual temperature profile as an input to the calculation has implicitly included the temperature change due to latent heat release. The entrainment rate (ε) could be parameterized as,

$$\varepsilon\overline{w}^2 = C_E ag\overline{\left(\frac{T_v'}{\overline{T_v}}\right)} \tag{4.11}$$

where C_E quantifies the influence of entrainment to cloud development and is 0.5 for shallow convection and 0.3 for deep convection [*Gregory*, 2001]. This parameterization assumes that entrainment dilute the in-cloud air and proportionally reduces buoyancy.

The detrainment rate is derived as follows. Starting from the mass continuity equation, we have,

$$-\rho\sigma\varepsilon\overline{w}+\rho\sigma\delta\overline{w}+\left(\frac{\partial\rho\sigma\overline{w}}{\partial z}\right)=0 \tag{4.12}$$

$$-\sigma\varepsilon M+\sigma\delta M+\left(\frac{\partial\sigma M}{\partial z}\right)=0 \tag{4.13}$$

where $M(=\rho\overline{w})$ is updraft mass flux. δ is set to a constant number of 2×10^{-4} m^{-1} throughout the convective layer until vertical velocity decreases with height, usually near cloud top, expression of which is to be derived later. Then we have,

$$\delta=\varepsilon-\frac{1}{M}\left(\frac{\partial M}{\partial z}\right) \tag{4.14}$$

From Equation 4.11, entrainment rate can be expressed as,

$$\varepsilon=C_E ag\left(\frac{\overline{T_v'}}{\overline{T_v}}\right)\Bigg/\overline{w}^2 \tag{4.15}$$

This method fails when $\overline{w}^2$ is small for example due to the encounter of tropopause and thus Equation 4.15 is likely to give an unreasonable large number of entrainment rates so to simplify the solution, entrainment is assumed negligible at the level where lower level moves faster than the immediate higher level. Below we try to derive the relationship between vertical velocity and detrainment rate.

$$\frac{M^{k-1}}{M^k}=C_\delta\frac{\overline{w}_{k-1}}{\overline{w}_k} \tag{4.17}$$

$$\frac{M^{k-1}-M^k}{M^k}=\frac{C_\delta\overline{w}_{k-1}-\overline{w}_k}{\overline{w}_k} \tag{4.18}$$

$$\frac{1}{M}\left(\frac{\partial M}{\partial z}\right) = -\delta = \frac{C_\delta \overline{w}_{k-1} - \overline{w}_k}{\overline{w}_k \Delta z} \tag{4.19}$$

So

$$\delta = \frac{\overline{w}_k - C_\delta \overline{w}_{k-1}}{\overline{w}_k \Delta z} \tag{4.20}$$

Note that here, $\overline{w}_{k-1}$ is one level lower than $\overline{w}_k$.

Finally, we arrive at the equation below. The first term on the right-hand side is the buoyancy term and the second is the drag term

$$\begin{aligned}
&\frac{1}{2}\frac{\partial \overline{w}^2}{\partial z} = \left(1 - C_E\right) ag\left(\overline{\frac{T_v'}{\overline{T}_v}}\right) - b\delta \overline{w}^2 \\
&\delta = \begin{cases} 2\times 10^{-4} m^{-1} & \overline{w}_{k-1} \le \overline{w}_k \\ \dfrac{\overline{w}_k - C_\delta \overline{w}_{k-1}}{\overline{w}_k \Delta z} & \overline{w}_{k-1} > \overline{w}_k \end{cases} \\
&a = 1/6 \\
&b = 2/3 \\
&C_E = 0.3 \\
&C_\delta = 0.8
\end{aligned} \tag{4.21}$$

4.4.2 Vertical velocity estimation and comparison with observations

Following Equation 4.21 and the mean cloud top buoyancy profile in Figure 4.7a (for convenience, reproduced in Figure 4.9a), Figure 4.9b shows the estimated vertical velocity of cloud top. Without *a priori* knowledge of the initial velocity condition at 5 km, three values, namely, 1, 3 and 5 m/s, are used to test the sensitivity of the model to the vertical velocity at 5 km. The result shows that, for three values, estimated vertical velocities quickly converge at 8 km and above. This is indeed consistent with Equation 4.21 that shows that updraft speed decreases faster when the updraft is strong and when buoyancy term is not strong enough to compensate the drag term.

The vertical velocity continues to increase to its maximum of 5 m/s at 12 km. This peak value is sensitive to the parameters in Equation 4.21. For example, under the assumption of no entrainment (i.e., C_E=0), which is likely in the case of inner core of a mesoscale convective system, the maximum velocity could be as large as 15 m/s. The vertical velocity then decreases as a result of the sharp decrease of CTB and the dependence of vertical accelerate on the detrainment rate, i.e., the stronger the vertical velocity, the sharper the decrease rate, and the larger the detrainment rate. Therefore, the vertical velocity of the cloud top quickly reduces to zero within 3 kilometers above. Figure 4.9b indicates that the level of neutral buoyancy is ~2 km higher than the level of maximum vertical velocity. The vertical velocity starts to decrease above 12 km when

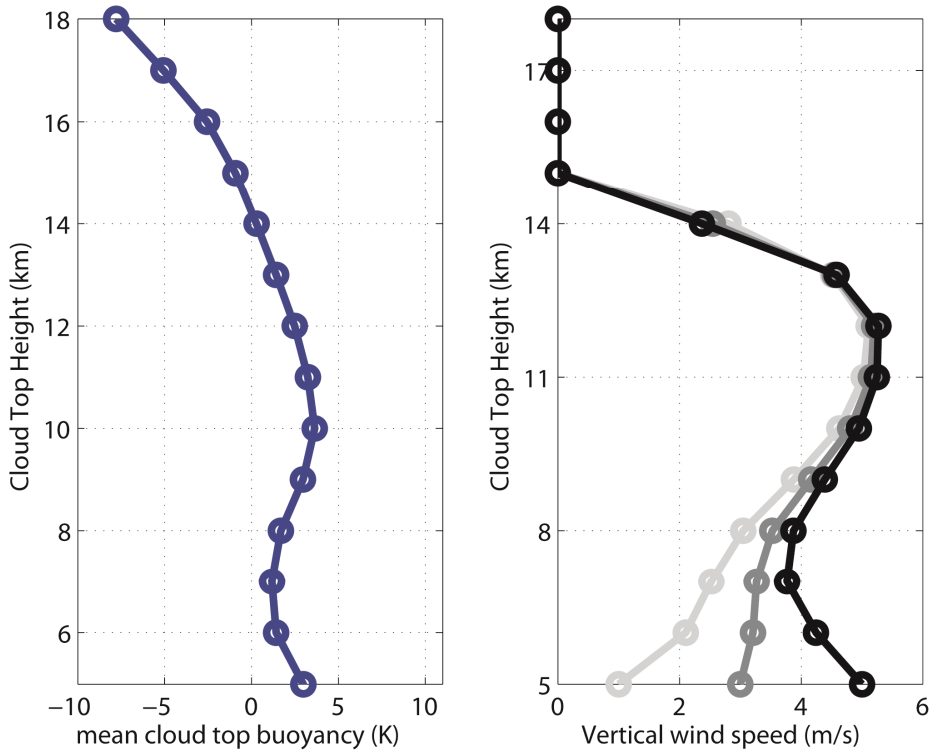

Figure 4.9. (left) the same profile as in Figure 4.7a. (right) Calculated vertical velocity with different initial velocity at the height of 5 km.

CTB is positive and >1 K. This is due to the negative sum of two terms on the right of Equation 4.21, which further highlights the role of drag and shows that positive CTB cannot guarantee positive upward acceleration. However, CTB of zero is nevertheless a good threshold to illustrate the buoyancy term in Equation 4.21 due to the lack of simultaneous measurement of cloud top vertical velocity.

As for other means of measuring cloud top vertical velocity, the most straightforward one is to use an airborne Doppler radar. Three mainstream platforms for such measurements are: a 3.2-cm wavelength tail (TA) Doppler radar onboard the National Oceanic and Atmospheric Administration (NOAA) WP-3D (P-3) aircraft [*Jorgensen*, 1984; *Marks and Houze*, 1987; *Aberson et al.*, 2006; *Reasor et al.*, 2009], a more advanced Electra Doppler Radar (ELDORA) operated by the National Center for Atmospheric Research (NCAR) [*Hildebrand et al.*, 1996, 1998; *Jorgensen et al.*, 1997; *Roux*, 1998; *Houze et al.*, 2006], and National Aeronautics and Space Administration (NASA) ER-2 Doppler radar (EDOP) which provides highest-quality vertical velocity estimates [*Heymsfield et al.*, 2010; *Guimond et al.*, 2010; *Cecil et al.*, 2010].

Using the P-3 TA radar in vertical incidence (~750-m along-track sampling), *Black et al.* [1996] found maximum vertical velocities between 10 and 26 m/s in seven intense Atlantic hurricanes. *Heymsfield et al.* [2010] compiled 13 vertical velocity profiles of deep convection in hurricanes using NASA ER-2 EDOP radar and found that the peak updraft speed was 13–14 m/s and always above 10-km level. *Guimond* [2010] likewise used NASA ER-2 Doppler radar and observed the deep convection during Hurricane Dennis (2005) and found that deep convective clouds had maximum updrafts of 20 m/s at 12~14 km height. Therefore, it has been observed that the

maximum vertical velocity in a deep convective cloud can be greater than 10 m/s and such maximum tend to occur above 10 km, both of which are consistent with the vertical velocity profile estimated here using satellite observations.

Observations in TOGA COARE, the Global Atmospheric Research Program (GARP) Atlantic Tropical Experiment (GATE), and other field experiments worldwide indicates that over the tropical oceans convective updrafts often have the minimum near the freezing level [*Zipser & LeMone*, 1980; *Lucas et al.*, 1994; *Igau et al.*, 1999]. This fact is also consistent with the profile in Figure 4.9 when the vertical velocity is large below freezing level.

With the deployment of geostationary satellite, cloud top vertical velocity can be derived from high temporal-resolution IR images before convective maturation. This approach takes advantage of the opaque cloud top and nearly constant lapse rate in the upper troposphere. A number of studies explore the potential of geostationary satellites in monitoring and predicting convective intensity [*Mecikalski et al.*, 2006; *Vila et al.*, 2008; *Zuidema et al.*, 2012]. For example, *Cintineo et al.* [2013] recently studied the convective microphysics during the developing convective intensification process using GOES-12 and GOES-13 imager data and obtained a maximum vertical velocity of 19~24 m/s, which is consistent with aforementioned radar measurements and our estimates.

Ground-based radar could also be used to infer the vertical development of convection. For example, *Uma et al.* [2012] has conducted observational study of the vertical velocity of deep convection over India subcontinent during dry and wet phase of the South Asia monsoon. Such in-situ ground-based study cannot give a thorough examination of the characteristics and possible mechanisms of vertical development of

convection due to the absence of information on the spatial distribution of convection and vertical temperature sounding. The vertical velocity profiles in Figure 3 of *Uma et al.* [2012] show that the vertical velocity increases linearly from 2 km to 6 km with a dent in the velocity profile at 7 km during the wet-phase of the monsoon; during the dry phase, the vertical velocity at 6 km can be as large as 3 m/s and the velocity decrease persists at 7 km. The vertical velocity levels off between 11 km and 13 km then decreases sharply to nearly zero, which is also consistent with our calculation. The observational result supports Figure 4.9 in that it captures the different scenarios with varying vertical velocity at 5 km but indicates that the parameters in Equation 4.21 may need further refinement.

In conclusion, the calculated vertical velocity profile based on the composite CTB profile largely agrees with direct observations of vertical velocity in three aspects: (1) a minimum velocity and a weak detrainment layer exist around the freezing level; (2) maximum vertical velocity is attained above 10 km; (3) the maximum vertical velocity can be greater than 15 m/s.

4.5 Further look on the fountain cloud assumption

4.5.1 Motivation

Although the calculation in previous section shows reasonable consistency with observation, its basis—the fountain cloud assumption—needs further scrutiny so we can understand to what extent properties inferred from cloud-top measurements can represent in-cloud features. In this section we use Goddard Cumulus Ensemble (GCE) model simulation to answer this question.

As in previous sections, here we focus on strong convective clouds with compact cloud tops, defined as CTF less than 4 km. We assume that there is a relationship between buoyancy for a convective cloud with CTH at a given level and the buoyancy of another convective cloud with larger vertical extent at the same level. This is based on the fact that vertical profiles of temperature and humidity govern the buoyancy profile from the thermodynamic perspective as shown by Equation 4.5 and 4.6. The difference are that the convective core is protected from the entrainment mostly at the boundary of the convective tower but the cloud top is directly exposed to the ambient air and cools itself by turbulent mixing and outgoing longwave radiation. However, the cloud top compactness lays the foundation of the fountain-cloud assumption because the selected clouds have fast evolving cloud tops with sprouting warm and moist air from inside the cloud. Therefore, the air at the cloud top has similar thermodynamic features as the in-cloud air to a certain degree and the bias between the two is expected to be a function of height.

A two-step method is proposed to track a deep convection event in the GCE model simulation. First, we use back-tracing method to single out a convective cloud with its complete life cycle. This is done by identify a strong deep convection case at its mature stage with CTH greater than 17 km and CTF less than 2 km. Then, a cost function is applied to identify the center of the convection and to trace back to its center one time step (6 minutes) before. Here, the cost function is defined as,

$$S = \frac{w\_\max}{STD(w\_\max)} \frac{CWP}{STD(CWP)} \exp(-\frac{r}{R}) \tag{4.22}$$

where STD stands for standard deviation, $w\_\max$ is the column maximum vertical velocity, CWP is cloud water path, r denotes the distance to the center of the convection,

and R is the radius of the convection. This function could well capture the updraft and the convective core with large water path. Mean horizontal wind is applied to correct horizontal drift of the convective center. This back-tracing method is repeated until the cloud top height is less than 4 km. The dissipating phase of convection is similarly traced.

Second, once the life cycle of convection is recorded, test particles are released at the earlier stage of the convection near the top of the boundary layer and are used for trajectory analysis. The buoyancy, vertical velocity and local air condition of each released particle are recorded and thus the in-cloud profile of each step could be reconstructed.

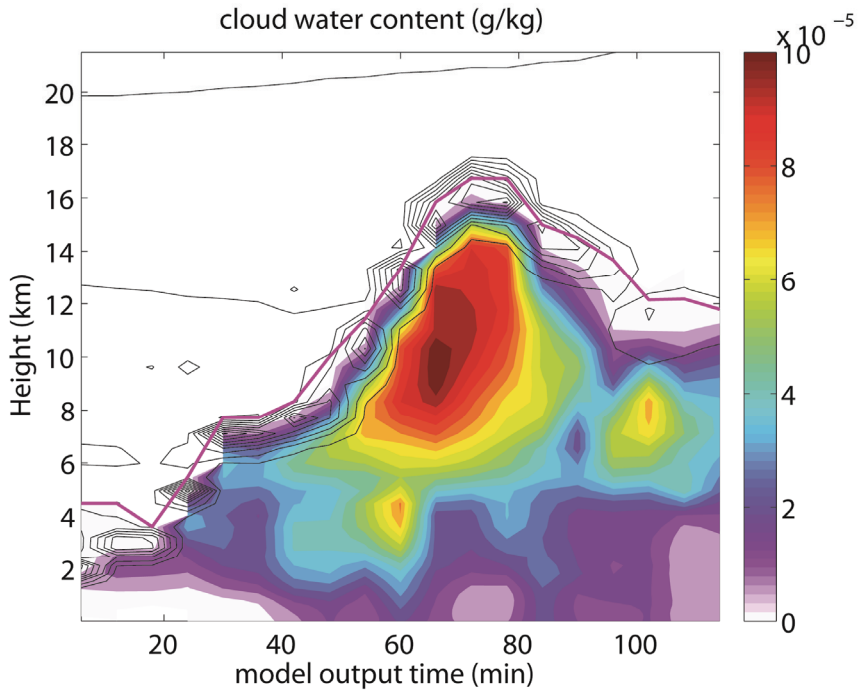

Figure 4.10. The color contour is modeled cloud water content and the line contour is short wave heating rate. The purple line is the cloud top height at each time step. Model output time interval is 6 minutes.

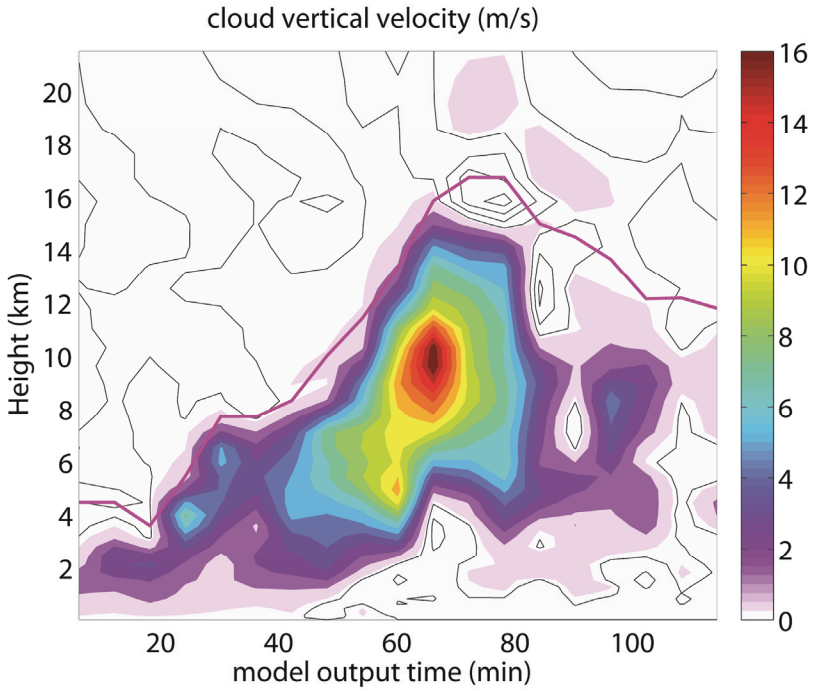

Figure 4.11. The vertical velocity is shown in color contour when upward and in line contour when downward. The purple line is still the cloud top level.

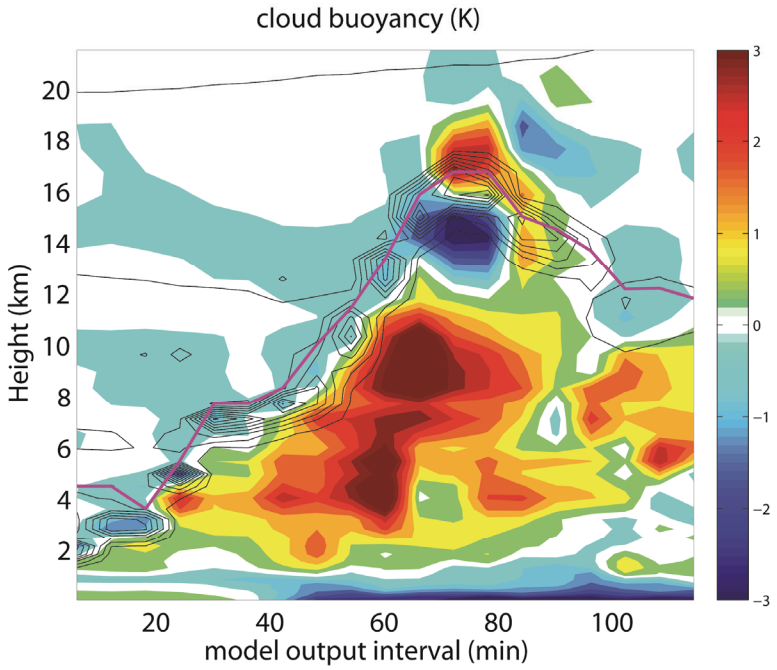

Figure 4.12. The cloud top buoyancy profile at each time step is shown in color contour. The line contour is short wave heating rate and the purple line indicates cloud top level. The cold air at the x-value of 12 results from a cold air intrusion due to strong horizontal wind.

4.5.2 Case analysis

Figure 4.10 shows the time-height cross section of a deep convection event identified using the back-tracking method. The color contour is cloud water content, the line contour is short wave heating rate, an indicator of cloud top height and cloud top fuzziness. The purple line is the cloud top height derived using simulated CloudSat radar reflectivity. Details of CTH identification in GCE simulation can be found in Chapter 3. At each time step, the CWC and short wave heating rate are consistent with each other in terms of the upper boundary of convective cloud. The step-to-step change of such upper boundary is consistent with that of CTH based on synthetic CloudSat radar reflectivity. The level of cloud top shows that convective vertical development slows down when cloud top reaches 7 km and in 10 mins afterwards, precipitation starts and the convection regain upward momentum. The vertical gradient of CWC delivers consistent information with the earlier argument in Section 4.2 that a tenuous cloud top of a convective cloud is associated with its dissipating phase. The short wave heating data likewise indicates that the penetration depth after 80 mins is larger than that before.

Figure 4.11 shows the cross section similar to Figure 4.10 except that the color contour being upward motion in vertical and the line contour the downward motion in vertical. The decrease of vertical velocity at the time step between 30 and 40 mins demonstrates in a straightforward way the slow-down of vertical convection development. The figure also indicates that the cloud obtains peak vertical velocity of ~16 m/s slightly above 10 km only 6 mins before its top reaches the highest altitude and two time steps prior to dominant downdraft at the cloud top.

Figure 4.12 displays buoyancy profile in color contour with the purple line and black contour lines being the same as in Figure 4.10. This figure basically supports conclusions drawn from Figure 4.11. The only exception is a cold air intrusion at 14 km at the time of 60 mins after the tracking starts. To get a mean in-cloud buoyancy vertical profile for the developing phase, the color-coded value is averaged for each layer from time zero to the time when cloud top reaches its maximum. The result is shown as the blue line in Figure 4.13. The red line is the buoyancy of an air parcel in the same convective case near the cloud top. The figure indicates that the two profiles are in the same order of magnitude and are close to each other at most altitudes. The cloud-top

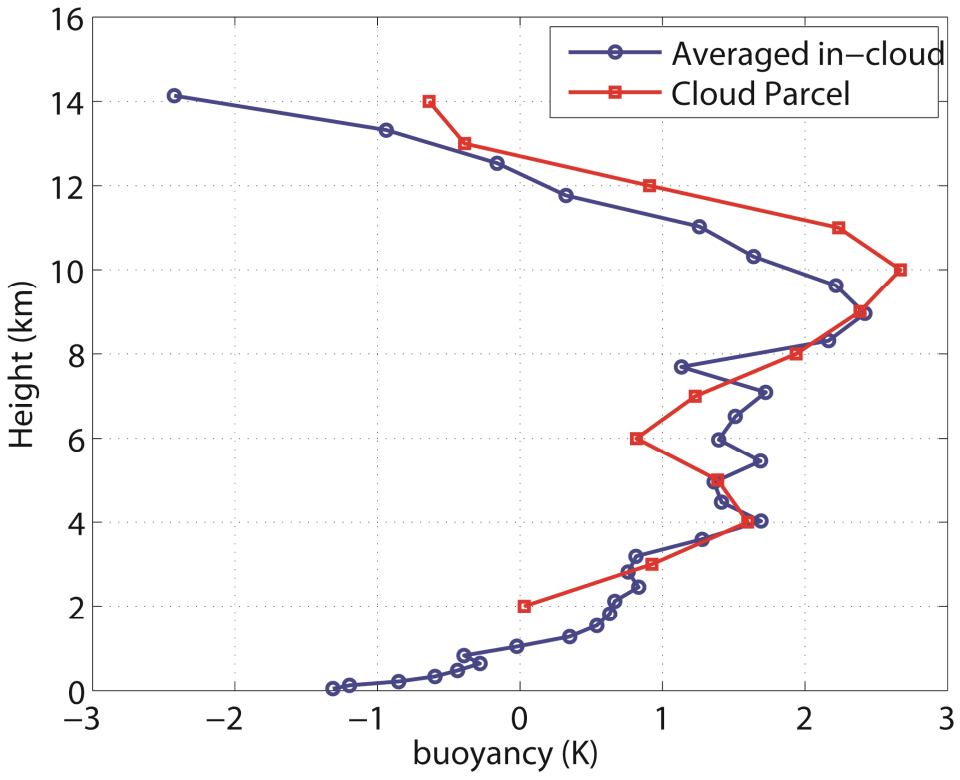

Figure 4.13. The blue line is the averaged in-cloud buoyancy during the developing phase of convection in Figure 4.12. The red line is buoyancy profile derived from parcel tracing method. The method to derive the red line is shown in Figure 4.14.

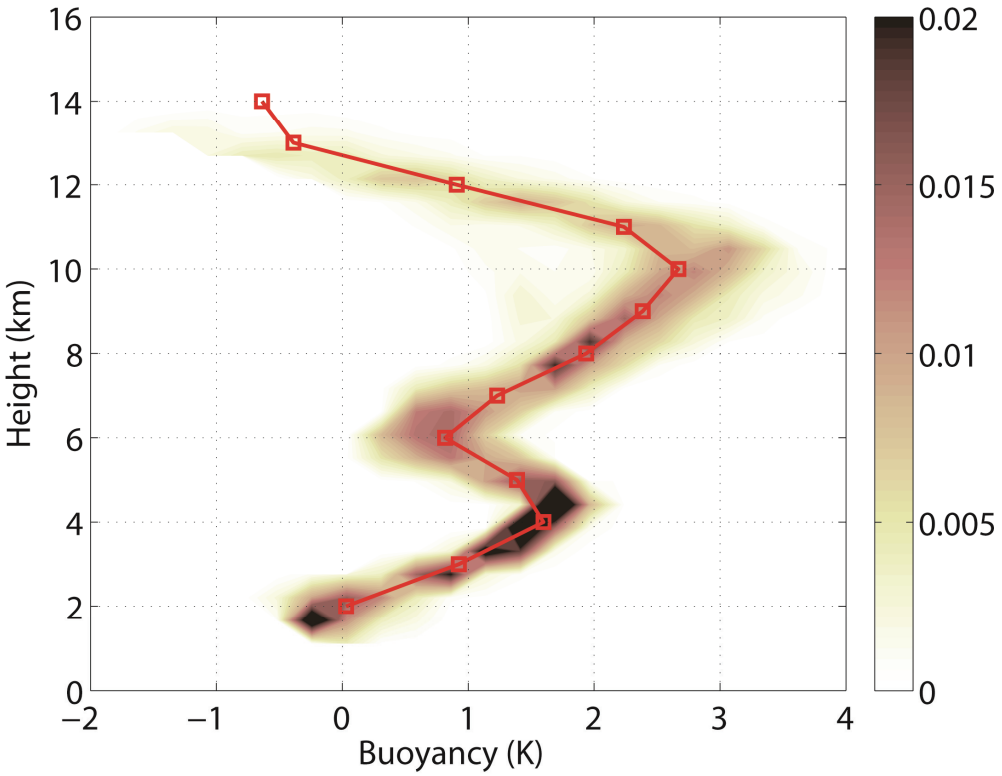

Figure 4.14. Cloud buoyancy profile of tracing particles. The buoyancy profile of each parcel is plotted in gray line and the red line is the 1-km layer averages.

buoyancy profile shows a dual-peak feature that is not obvious in the averaged in-cloud buoyancy profile. Based on Figure 4.12, it is likely that during the developing stage, the in-cloud updraft at 6 km is stronger than it at cloud top when the cloud top first reaches this level, which compensates the effect of freezing level and leads to multiple wiggles seen in the blue line between 4 km and 8 km.

The calculation method of the red curve in Figure 4.13 is given below. Air parcels are tagged at the level of 2~4 km at the first stage of the convective case. Only those reaching 13 km before the time of 72 mins are singled out to analyze their paths. There are totally 229 particles selected, accounting to 0.29% of the total. Due to the large time step in model simulation, the trajectory and the corresponding buoyancy information of

each selected particles are linearly interpolated into finer vertical grids. The shaded contour in Figure 4.14 shows the buoyancy distribution experienced by each particle during the ascent. The distribution is normalized so all colors add up to one. Different colors indicate the possibility that a particle is at a certain level with a certain amount of buoyancy. Therefore, the clusters at 2 and 4 km imply slow vertical velocity and less dispersion in the buoyancy state space. The red line is the mean of each 1-km layer of the shaded contour. If the profile is truncated from above 5 km, it clearly resembles the buoyancy profile in Figure 4.10.

4.6 Conclusions

This chapter further examines the cloud top buoyancy (CTB) statistics derived from Chapter 2 & 3 and provides a dynamic framework to link such CTB profile with dynamic variable, i.e., vertical velocity in this context. Out of 39,123 convective clouds sampled by CloudSat, 54.4% has relatively compact cloud tops with cloud top fuzziness less than 4 km and are used for the analysis. Spatial distributions of CTB as observed by CloudSat for cumulus congestus mode and deep convection mode are depicted and their diurnal differences are also discussed. The composite positive CTB statistics has features consistent with in-situ observations like the weak detrainment at the freezing level and shows great similarity with modeled counterparts. The CTB of cumulus congestus mode is more sensitive to diurnal and land-ocean differences than that of deep convection mode.

The buoyancy profile is used to derive vertical velocity profile using a diagnostic relations employed before by modelers. The results qualitatively agree with observations in several aspects, such as that the level of minimum vertical velocity at 6~7 km, the level of maximum vertical velocity at around 12 km, and the magnitude of maximum vertical

velocity. The cloud top velocity calculation is conducted based on the assumption that the cloud top condition is representative of in-cloud condition, so-called fountain cloud assumption. The validity of this assumption is examined using GCE model simulation. A back-envelope trajectory method is used to derive the Lagrangian view of simulated deep convection event such that in-cloud buoyancy at a given altitude can be compared with the CTB at the same altitude. The results suggest the in-cloud buoyancy and CTB are close to each other over many altitudes, lending a further support onto the merit of estimating vertical velocity from convective cloud top buoyancy measured by satellite observations such as CloudSat and MODIS.

4.7 Acknowledgements

The CloudSat data were obtained from the CloudSat Data Processing Center. The MODIS data were obtained from NASA Goddard DISC. The ECMWF interim data used in this study were obtained from http://data.ecmwf.int/data/. The GCE simulation result is provided by Dr. Xiping Zeng. This research is supported by the NASA MAP project under grant NNX09AJ46G awarded to the University of Michigan and the NASA CloudSat/CALIPSO Science Team under grant NNX10AM31G and SEAC4RS Science Team under grant NNX12AC13G awarded to the City University of New York (CUNY).

References

Aberson, S. D., M. L. Black, R. A. Black, R. W. Burpee, J. J. Cione, C. W. Landsea, and F. D. Marks Jr. (2006), Thirty years of tropical cyclone research with the NOAA P-3 aircraft, *Bull. Amer. Meteor. Soc.*, 87, 1039–1055.

Black, Micheal L., R. W. Burpee, F D. Marks (1996), Vertical Motion Characteristics of Tropical Cyclones Determined with Airborne Doppler Radial Velocities, *J. Atmos. Sci.*, 53, 1887–1909.

Cecil, Daniel J., Kevin R. Quinlan, Douglas M. Mach (2010), Intense Convection Observed by NASA ER-2 in Hurricane Emily (2005), *Mon. Wea. Rev.*, 138, 765–780.

Chahine, M. T., and et al. (2006), AIRS: Improving Weather Forecasting and Providing New Data on Greenhouse Gases, *Bull. Amer. Meteor. Soc.*, 87, 911–926.

Cintineo, John L., Michael J. Pavolonis, Justin M. Sieglaff, Andrew K. Heidinger (2013), Evolution of Severe and Nonsevere Convection Inferred from GOES-Derived Cloud Properties, *J. Appl. Meteor. Climatol.*, 52, 2009–2023.

Del Genio, A. D., M.-S. Yao, and J. Jonas (2007), Will moist convection be stronger in a warmer climate? *Geophys. Res. Lett.*, 34, L16703.

Emanuel, K. A., (1994), *Atmospheric Convection*, Oxford University Press, ISBN 0-19-506630-8.

Folkins, Ian (2009), A One-Dimensional Cloud Model with Trimodal Convective Outflow, *J. Climate*, 22, 6437–6455.

Gregory, D. (2001), Estimation of entrainment rate in simple models of convective clouds, *Q.J.R. Meteorol. Soc.*, 127: 53–72.

Guimond, Stephen R., Gerald M. Heymsfield, F. Joseph Turk (2010), Multiscale Observations of Hurricane Dennis (2005): The Effects of Hot Towers on Rapid Intensification, *J. Atmos. Sci.*, 67, 633–654.

Heymsfield, G. M., Lin Tian, Andrew J. Heymsfield, Lihua Li, Stephen Guimond (2010), Characteristics of Deep Tropical and Subtropical Convection from Nadir-Viewing High-Altitude Airborne Doppler Radar, *J. Atmos. Sci.*, 67, 285–308.

Hildebrand, P. H., et al. (1996), The ELDORA/ASTRAIA Airborne Doppler Weather Radar: High-Resolution Observations from TOGA COARE, *Bull. Amer. Meteor. Soc.*, 77, 213–232.

Hildebrand, Peter H. (1998), Shear-Parallel Moist Convection over the Tropical Ocean: A Case Study from 18 February 1993 TOGA COARE, *Mon. Wea. Rev.*, 126, 1952–1976.

Houze, R. A., et al. (2006), The Hurricane Rainband and Intensity Change Experiment: Observations and Modeling of Hurricanes Katrina, Ophelia, and Rita, *Bull. Amer. Meteor. Soc.*, 87, 1503–1521.

Igau, R. C., M. A. LeMone, and D. Wei (1999), Updraft and downdraft cores in TOGA COARE: Why so many buoyant downdraft cores? *J. Atmos. Sci.*, 56, 2232–2245.

Johnson, Richard H., Thomas M. Rickenbach, Steven A. Rutledge, Paul E. Ciesielski, Wayne H. Schubert (1999), Trimodal Characteristics of Tropical Convection, *J. Climate*, 12, 2397–2418.

Jorgensen, D. P. (1984), Mesoscale and Convective-Scale Characteristics of Mature Hurricanes. Part II. Inner Core Structure of Hurricane Allen (1980), *J. Atmos. Sci.*, 41, 1287–1311.

Jorgensen, D. P., M. A. LeMone, S. B. Trier (1997), Structure and Evolution of the 22 February 1993 TOGA COARE Squall Line: Aircraft Observations of Precipitation, Circulation, and Surface Energy Fluxes, *J. Atmos. Sci.*, 54, 1961–1985.

Korolev, A. V., Isaac, G. A., Cober, S. G., Strapp, J. W. and Hallett, J. (2003), Microphysical characterization of mixed-phase clouds, *Q.J.R. Meteorol. Soc.*, 129: 39–65.

Lucas, C., E. J. Zipser, and M. A. Lemone (1994), Vertical velocity in oceanic convection off tropical Australia, *J. Atmos. Sci.*, 51, 3183–3193.

Marks, F. D., and R. A. Houze Jr. (1987), Inner core structure of Hurricane Alicia from airborne Doppler radar observations, *J. Atmos. Sci.*, 44,1296–1317.

Mecikalski, John R., Kristopher M. Bedka (2006), Forecasting Convective Initiation by Monitoring the Evolution of Moving Cumulus in Daytime GOES Imagery, *Mon. Wea. Rev.*, 134, 49–78.

National Oceanic and Atmospheric Administration, National Aeronautics and Space Administration, and United States Air Force (1976), *U.S. Standard Atmosphere*, NOAA-S/T 76–1562.

Rao, T. Narayana, K. N. Uma, T. Mohan Satyanarayana, D. Narayana Rao (2009), Differences in Draft Core Statistics from the Wet to Dry Spell over Gadanki, India (13.5°N, 79.2°E), *Mon. Wea. Rev.*, 137, 4293–4306.

Reasor, P. D., M. D. Eastin, and J. F. Gamache (2009), Rapidly intensifying Hurricane Guillermo (1997). Part I: Low-wavenumber structure and evolution, *Mon. Wea. Rev.*, 137, 603–631.

Rosenfeld, D., W. Woodley (2000), Deep convective clouds with sustained suppercooled liquid water down to -37.5^{o}C, *Nature*, 405, 440-442.

Roux, F. (1998), The oceanic mesoscale convective system observed with airborne Doppler radars on 9 February 1993 during TOGA-COARE: Structure, evolution and budgets. Quart, *J. Roy. Meteor. Soc.*, 124, 585–614.

Thompson, R. M., S. W. Payne, E. E. Recker, and R. J. Reed (1979), Structure and properties of synoptic-scale wave disturbances in the intertropical convergence zone of the eastern Atlantic, *J. Atmos. Sci.*, 36, 53-72.

Uma, K. N., K. Kishore Kumar, Siddarth Shankar Das, T. N. Rao, T. M. Satyanarayana (2012), On the Vertical Distribution of Mean Vertical Velocities in the Convective Regions during the Wet and Dry Spells of the Monsoon over Gadanki, *Mon. Wea. Rev.*, 140, 398–410.

Vila, Daniel Alejandro, Luiz Augusto Toledo Machado, Henri Laurent, Inés Velasco (2008), Forecast and Tracking the Evolution of Cloud Clusters (ForTraCC) Using Satellite Infrared Imagery: Methodology and Validation, *Wea. Forecasting*, 23, 233–245.

Zipser, E. J., and M. A. LeMone (1980), Cumulonimbus vertical velocity events in GATE. Part II: Synthesis and model core structure, *J. Atmos. Sci.*, 37, 2458–2469.

Zuidema, P., Z. Li, R. Hill, L. Bariteau, B. Rilling, C. Fairall, W. A. Brewer, B. Albrecht and J. Hare (2012), On trade-wind cumulus cold pools, *J. Atmos. Sci.*, 69, pp. 258-277.

Zuidema, P. (1998), The 600–800-mb Minimum in Tropical Cloudiness Observed during TOGA COARE, *J. Atmos. Sci.*, 55, 2220–2228.

Chapter 5

Black carbon in the stratosphere by overshooting convection and its detection: a preliminary modeling-based study

5.1 Introduction

The planetary boundary layer (PBL) is well mixed due to its turbulent nature. It is rich in water vapor as well as anthropogenic products like carbon monoxide, sulfur, and black carbon. Transport of trace gases and aerosols from the troposphere to the stratosphere has profound implications for stratospheric chemistry, radiative balance, as well as climate change. As a result, it has been always a focused theme in the study of climate change [*Stocker et al.*, 2013]. For example, once transported into the lower stratosphere (LS), water vapor can perturb the local chemical balance and radiation budget [*Oinas et al.*, 2001; *Shindell*, 2001; *Forster and Shine*, 2002; *Zhong and Haigh*, 2003; *Manoj et al.*, 2006; *Thomas et al.*, 2007; *Solomon et al.*, 2010; *Satheesh et al.*, 2013] and the effect can even propagate upward to the middle stratosphere [*Mote et al.*, 1996].

Aerosols such as black carbon (BC) can also be lifted to the LS [*Pueschel*, 1996] and, once in the LS, can play important role in regional and global climate systems (e.g., *Gao et al.* [2008]). The reasons are threefold. First, aerosols participate in gaseous chemical reactions. One notable example is the contribution to ozone destruction. Earlier laboratory studies have shown that ozone deposition on aerosol surfaces could provide large surface area for heterogeneous reaction of ozone destruction, the rate of which is faster than that of homogenous chemical reactions [*Schurath and Naumann*, 1998; *Disselkammp et al.*, 2000]. This laboratory study has been confirmed by observational studies in cases of volcanic eruption [*Hofmann and Solomon*, 1989], polar stratospheric cloud [*Tilmes et al.*, 2008], and aircraft exhaust [*Berkowitz et al.*, 2000]. Second, the absorbing aerosol such as BC absorbs in both short wave and long wave thus could change the radiative heating in the LS and likely warm the ambient atmosphere in the LS. Since the reaction rate of ozone destruction positively depends on temperature [*Kamm et al.*, 1999], a slightly warming stratosphere would accelerate ozone depletion reaction. Third, the stratosphere is a stable reservoir and the lifetime of aerosol in the LS can be much longer than that in the troposphere, further prolonging its influence in the stratosphere.

Since the sources of aerosol emissions are far below the stratosphere, aerosol concentrations in the stratosphere are strongly influenced by transport mechanisms. Two venues of entering the stratosphere are (1) gradual ascending following the large-scale circulation and (2) overshooting deep convection (ODC). A number of studies have demonstrated that the transportation by ODC is prominent over India subcontinent, where BC emission also happens to be significant. About 75% of the total summer water vapor

transport into the tropical stratosphere may occur over the South Asian monsoon regions [*Gettelman et al.*, 2004]], contributing to >25% of the water vapor in the middle stratosphere [*Bannister et al.*, 2006]. *Fu et al.* [2006] suggests moist convection over Asian monsoon is a primary mechanism that transports water vapor and carbon monoxide into the LS. *Randel et al.* [2010] identifies the transport of air masses by deep convection from the PBL during the Asian monsoon and deep into the LS using satellite observations of hydrogen cyanide (HCN), an atmospheric pollutant produced in biomass burning. Recent studies find that the tropical tropopause layer over the south Asia region is thinnest (1-2 km) during the Asian monsoon season [*Thampi et al.*, 2012; *Uma et al.*, 2012]. Therefore, the strong convection embedded in the Asian monsoon circulation, coupled with the thinning of the tropical tropopause layer, provides an effective pathway for aerosols originated from the PBL of India subcontinent to enter the stratosphere [*Thampi et al.*, 2012; *Uma et al.*, 2012]. In this chapter, we want to explore this issue further using a state-of-the-art climate-chemistry-aerosol model, paying attention to Indian region and possible detection strategy of such BC transported by ODC events. Before we proceed on this topic, below we will present a general background description about BC.

5.1.1 Black carbon in the climate system

Among all types of aerosols, BC is the dominant absorber for visible and near-IR light even though it normally makes up only a small fraction of the total mass of suspended aerosols [*Lindberg et al.*, 1975, 1993]. Several studies have attempted to quantify the direct radiative forcing of airborne BC to the climate system [*Haywood and Shine*, 1995; *Haywood et al.*, 1997; *Schult et al.*, 1997; *Haywood and Ramaswamy*, 1998;

Myhre et al., 1998; *Penner et al.*, 1998; *Jacobson*, 2000, 2001a, 2001b; *Bond et al.*, 2013]. These studies also established the important role of BC in radiative balance of the climate system. For example, *Jocaboson* [2001a] indicates that heating of the atmosphere due to absorption of solar radiation by BC exerts a direct global warming forcing that may be comparable to the forcing of the greenhouse gas methane. The most recent IPCC report shows that the mean climate radiative forcing of BC is 0.4 W/m^2, comparable to that of methane (0.48 W/m^2) [*Stocker et al.*, 2013].

When deposited onto snow and sea-ice, BC can reduce reflectance due to the much larger absorption coefficients of BC than ice [e.g., *Warren and Wiscombe*, 1980]. This mechanism is of interest as BC can alter the melting timing and spatial coverage of snow and ice, which implies that polar climate systems are especially vulnerable to BC deposition. For example, it has been demonstrated that BC can contribute to the warming in the Arctic and to the observed abrupt glacier retreat [*Flanner et al.*, 2007, 2012, 2013; *Lee et al.*, 2013; *McConnell et al.*, 2007; *Painter et al.*, 2013, *Bond et al.*, 2011, 2013; *Kaspari et al.*, 2011; *Lee et al.*, 2013; *Zhou et al.*, 2012].

BC has two unique properties that make it easy to be lifted to the LS by ODC. First, BC is usually small in size and with porous surface. Second, the scavenging efficiency of BC is ~30%, less than half of the value of large particles [*Pruppacher and Klett*, 1978]. Therefore, in an ODC transport event, BC can be efficiently transported to the LS. *Fromm et al.* [2005] has observed a pyro-cumulonimbus event in the midst of a boreal forest fire and attributed the five-fold increase in lower stratosphere aerosol burden to specific pyro-cumulonimbus cells.

5.1.2 Measuring airborne BC

Quantification of the radiative effect of BC has long been suffering from uncertainties in BC measurement. BC concentration is most commonly measured optically by the change in light transmittance, reflection caused by particles [*Gundel et al.*, 1984; *Hansen et al.*, 1984], or absorption [*Heintzenberg*, 1982; *Hitzenberger et al.*, 1996]. For example, the laboratory measurement is currently conducted using aethalometer [*Hansen et al.*, 1983; *Kirchstetter and Novakov*, 2007].

In-situ measurements usually rely on high-altitude balloons [*Babu et al.*, 2011] and airplanes flying in the LS [*Moteki et al.*, 2012], which offers a glimpse of BC abundance in the atmosphere but are limited by its temporal and spatial coverage. There have been a small numbers of field campaigns to measure the vertical profiles of BC mixing ratios in a larger region and with longer duration. For example, the Aerosol Radiative Forcing over India (ARFI) aircraft/high altitude balloon campaigns [*Satheesh et al.*, 2008], Arctic Research of the Composition of the Troposphere from Aircraft and Satellites (ARCTAS; *Jacob et al.* [2010]), Aerosol, Radiation, and Cloud Processes affecting Arctic Climate (ARCPAC; *Warneke et al.* [2010]), Aerosol Radiative Forcing in East Asia (A-FORCE; *Oshima et al.* [2012]) and HIAPER Pole-to-Pole Observations (HIPPO1; *Schwarz et al.* [2010]) campaigns. Despite of the sampling limitations, these observations have demonstrated great potential in model diagnostics of the scavenging and vertical dispersion of BC [*Koch et al.*, 2009].

In addition to in-situ measurements, remote sensing techniques have also been used taking advantage of the scattering and absorbing features of different aerosols in the

visible and NIR bands. However, such measurement methods usually do not specifically retrieve black carbon but rather aerosols in general. For example, the NASA-Jet Propulsion Laboratory ozone lidar [*McDermid et al.*, 1995] detects aerosols using scattering ratio at 355 and 387 nm up to upper stratosphere (~40 km) with fine vertical resolution. Ground-based radiation techniques, such as sun-sky photometer performance by Aerosol Robotic Network (AERONET) [*Dubovik et al.*, 2002] and Sky Radiometer Network (SKYNET) [*Nakajima et al.*, 2007], could routinely measure column-integrated absorption aerosol optical depth (AAOD). CALIPSO mission [*Winker et al.*, 2010] can retrieve backscattered signal at 532 nm and 1064 nm and polarization signal at 532 nm in its nadir view. The aerosols classification [*Omar et al.*, 2009] is made possible by analysis of backscatter difference which help differentiate cloud particles and aerosols of different sizes and by analysis of polarization data which distinguish spherical and non-spherical particles like for liquid aerosols and solid aerosols. However, because low BC concentration in the stratosphere and thus low signal-to-noise ratio on individual profiles in the nadir view, averaging is required [*Vernier et al.*, 2009] and observation of BC of an individual case in the stratosphere is difficult.

Additionally, measurements of stratospheric aerosol are carried out using solar occultation method. The use of solar occultation probing allows measuring the atmospheric transmission and then to retrieve stratospheric aerosol extinction profiles with high vertical resolution [*Lenoble et al.*, 1984; *Ernst et al.*, 2012]. It has been used by instrument series of the SAM (Stratospheric Aerosol Measurement) [*McCormick and Trepte*, 1986], the SAGE (Stratospheric Aerosol and Gas Experiment) [*McCormick and Veiga*, 1992], and POAM (Polar Ozone and Aerosol Measurement) [*Lumpe et al.*, 1997].

The disadvantages of measurement technique are two-fold. First, the limb-view radiance measurements are twice per orbit at most during sunsets and sunrises. Therefore, the repeating pattern does not allow frequent measurement over a specific region like India subcontinent in the following sections. Second, the solar radiance measurements are likely to be contaminated by stray light. Mie scattering is strong in the visible band and sunlight from the surface reflection may ultimately get into the sensor's field of view through multiple scattering. This method, however, is not optimal for BC retrieval. The reasons are that the majority of the stratospheric aerosols are sulfuric acid [*Schwarz et al.*, 2008; *Murphy et al.*, 2013] and that their extinction profiles are not distinguishable from BC extinction profile.

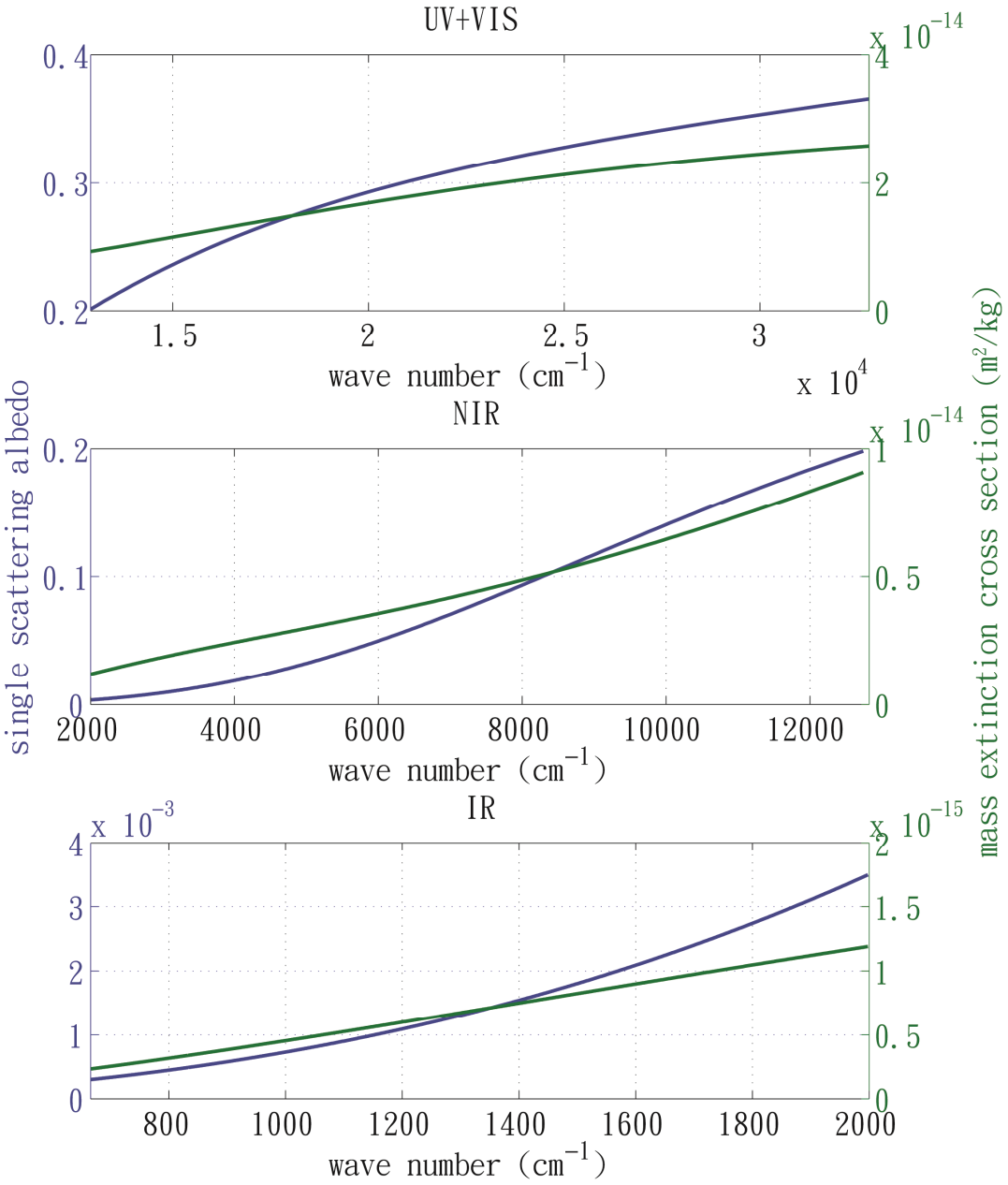

Figure 5.1 The single scattering albedo (blue) and mass extinction cross section (green) of black carbon in (a) the ultraviolet (UV) and visible band, (b) near infra-red (NIR) band, and (c) infra-red (IR) band.

5.1.3 The rationale for this exploratory study

Given the limitations of current measurements, in this exploratory study we take modeling approach: we carried out OSSE (observing system simulation experiments) using a state-of-the-art climate-chemistry model and used the output from such simulation experiments as surrogates of reality. The questions that we want to address using such surrogate data are:

(1) In what manner does BC get into the LS?

(2) In the vertical direction, is it possible to attribute BC transport to ODC?

(3) How to remotely detect BC?

The next section describes the climate-chemistry model that we used, the simulation that we carried out, and the evaluation of relevant model performance. Section 5.3 presents a proposed method for observing BC in the lower stratosphere. The applicability of the method is then further discussed in section 5.4.

5.2 Model and its performance

5.2.1 Model description

This study uses simulation by the Geophysical Fluid Dynamics Laboratory (GFDL) coupled chemistry-climate model, atmospheric model version 3 (AM3) [*Donner et al.*, 2011], as the surrogate of real atmosphere. AM3 is the successor of the GFDL AM2 model [*Anderson et al.*, 2004] with significant improvements in physics, dynamics, cloud and precipitation processes, vertical resolutions of the stratosphere, and climate-chemistry coupling. Finite-volume dynamical core [*Lin*, 2004] is applied on a cubed-

sphere grid [*Putman and Lin*, 2007] for its grid uniformity and overall accuracy. The number of vertical layers has doubled from 24 layers in the AM2 to 48 layers in the AM3, with both increased vertical resolutions in the stratosphere and higher upper boundary. The full details of standard AM3 model configuration are available in *Donner et al.* [2011] and references there-in.

AM3 calculates the mass distribution and optical properties of aerosols based on their emission, chemical reactions, transport, and dry and wet removal. The transport processes include advection, convection, and eddy diffusion by turbulence. Anthropogenic and biomass burning emissions of sulfur dioxide, black carbon, and organic carbon are from *Lamarque et al.* [2010]. Cloud scavenging of aerosol species is calculated following *Giorgi and Chameides* [1985]. The fully on-line aerosols calculation in the AM3 is the major difference from its predecessors, which used prescribed aerosol concentrations computed from another off-line chemical transport model [*Delworth et al.*, 2006]. AM3 uses different emissions inventories and optical properties from the AM2. It also includes internal mixing and couples wet deposition to cloud microphysics. Two fundamental aerosol properties in the AM3, aerosol optical depth and coalbedo (ratio of absorption optical depth to total optical depth), have been compared with AERONET observations [*Holben et al.*, 2001; *Dubovik et al.*, 2002; *Sato et al.*, 2003] to show improvement compared to the AM2 simulation. It has been shown (Figure 3c and 3d in *Donner et al.* [2011]) that the AM3 outperform AM2 in simulating environment in dusty, polluted as well as biomass burning regions.

In this study, we use the standard version of AM3 forced by observed SST from 2000 to 2012. Its horizontal resolution after mapping from cubed-sphere grid back to

latitude-longitude grid is about $2^{o}\times2.5^{o}$. 3-hourly instantaneous output of a variety of variables has been archived and used in our analysis.

5.2.2 Model performance of climatology simulation

Since the focus of the investigation is the transportation by ODC in the tropics, the simulated tropical ODC needs to be evaluated first. The method to detect ODC in the AM3 model is as follows. For each grid at each output time step, the tropopause is defined as the level where lapse rate first becomes less than 2 K/km (the thermodynamic definition of tropical tropopause). Then ODC is identified if the convective mass flux is positive at the tropopause. Figure 5.2 compares occurrence frequency of simulated ODC against the tropical ODC statistics compiled by *Takahashi and Luo* [2014] using CloudSat observations from 2006 to 2011. Both simulated and observed ODC events are concentrated within regions known for frequent occurrence of deep convections. The model agrees well with the observations on both the spatial map and the frequency statistics.

The amount of BC transported to the LS is strongly influenced by both frequency of ODC and BC concentration at the surface. Thus it is instructive to look at the map of BC concentration at different pressure levels in different seasons (Figure 5.3). Most overshooting convection take place over tropical oceans where the PBL air is relatively clean. As Figure 5.3 suggests, BC concentration near the surface is high in tropical Africa and South America during seasons of active biomass burning of forests and savannas and in the populous marine continent. Outside the deep tropics, India and China have large BC concentration near the surface. At 500 hPa, BC concentration over land in northern

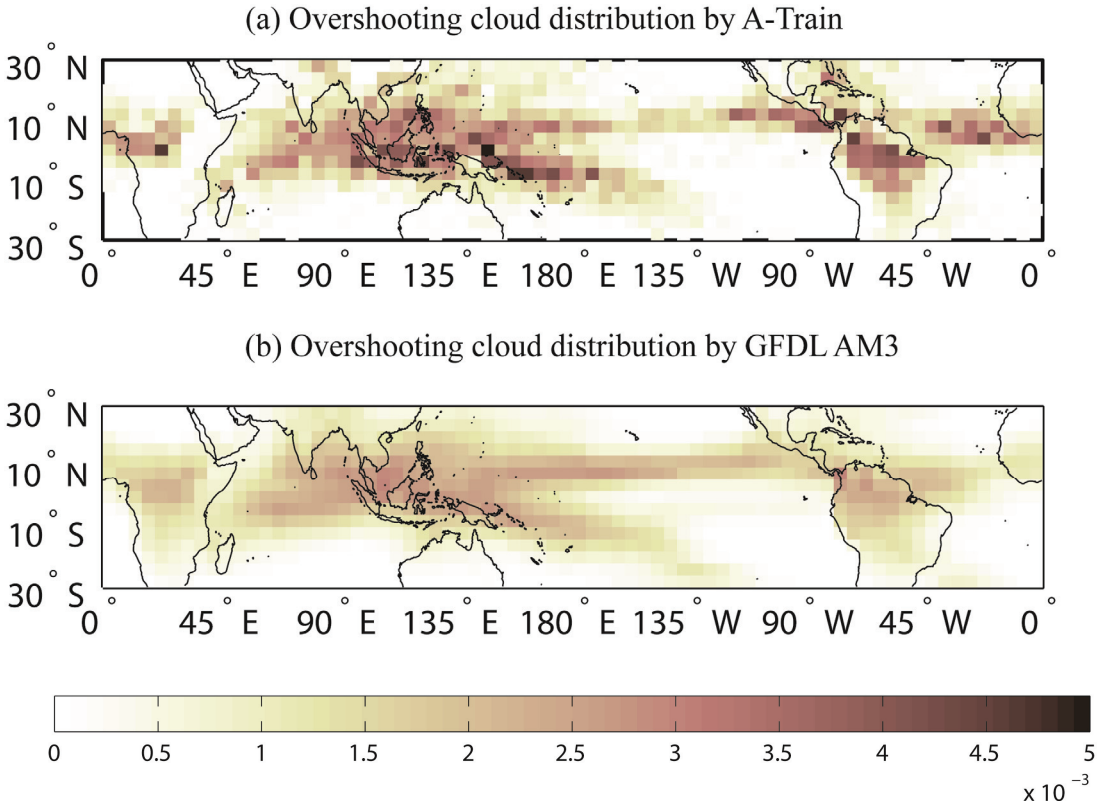

Figure 5.2 Occurrence frequency of overshooting convection over the tropics in $4^{o}\times5^{o}$ grids in latitude and longitude. The color-coded number indicates the fraction of overshooting convection events of all ODCs in each grid box. All fractions on the map add up to unity. (a) Based on observations by CloudSat and CALIPSO. (b) Based on the 3-hourly output of the AM3 simulation.

hemisphere shows a stronger seasonal variation compared with that at 925 hPa, implying seasonal change of vertical transport.

The simulated seasonal variation of BC at 100 hPa worth some discussions. In boreal summer (JJA), the most noticeable feature at 100 hPa is the dichotomy separated by ITCZ. This feature should be caused by the northward and southward branches of Hadley circulations, which nearly prohibits the mixings between two branches. The maximum simulated BC concentration is over Indian subcontinent. Recent studies [*Fu et al.*, 2006; *Randel et al.*, 2006; *Park et al.*, 2007, 2008] show that anticyclone persistent

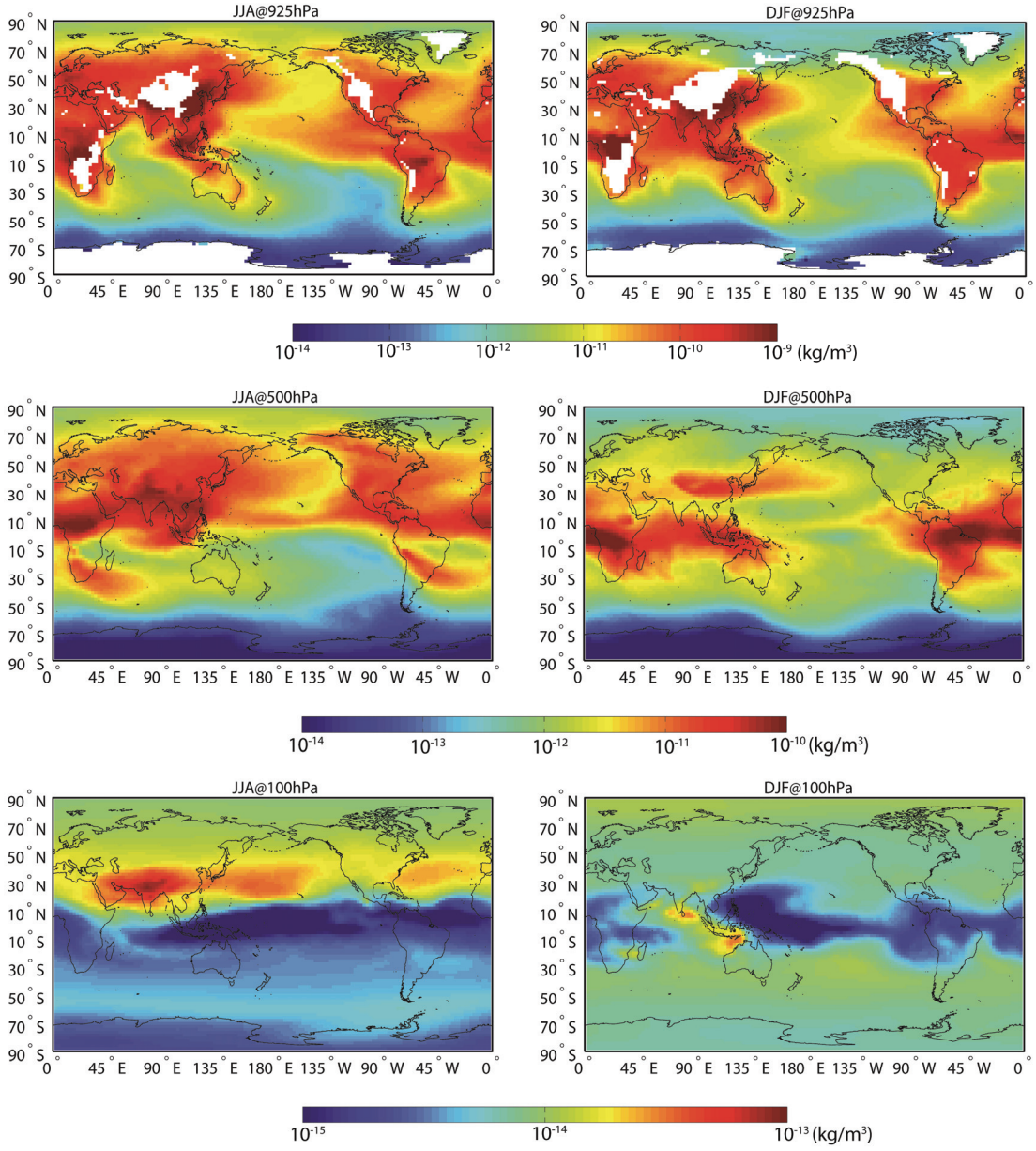

Figure 5.3 Global distribution of black carbon simulated by the GFDL AM3 model at 925 hPa, 500 hPa, and 100 hPa. The left panels are for boreal summer and the right for boreal winter. Note different color scales are used for different pressure levels.

over large portion of Asia during boreal summer confines the pollution in the upper troposphere, slows down the dispersion process, and thus contributes to the prolonged local BC maximum. This is likely also the reason for this simulated BC maximum at 100 hPa over India. The BC concentration over China is larger than that over India at the planetary boundary layer. Therefore, the difference between BC concentrations at 100 hPa over India and over China during boreal summer points to the influence of South Asian monsoon and orographic effect of the Tibetan Plateau. In boreal winter (DJF), the dichotomy vanishes and the maximum of simulated BC at 100 hPa moves southward to the south end of India subcontinent and maritime continents. Therefore, frequent ODC events, high BC ground emission, and upper-level anticyclone in the troposphere in the boreal summer makes India an ideal place for vertical transports of BC into the LS by the ODC events. In this study, we will focus on this area, specifically, 15~25^{o}N and 73.75~86.25^{o}E.

Water vapor is also transported into the LS in the same manners as the BC. Since water vapor measurements are much more widely available than BC measurement, the performance of the GFDL AM3 model on tropical troposphere-stratosphere exchange can be evaluated by comparing simulated and observed time-dependent behaviors of water vapor. The water vapor enters the tropical LS through the tropical tropopause with a strong seasonal dependence and such seasonal dependence propagates upward into the middle stratosphere, usually known as the "tape recorder" effect [*Mote et al.*, 1996]. Figure 5.4 shows the time-height cross section of water vapor anomalies averaged over Indian subcontinent from 2005 to 2012 as observed by Microwave Limb Sounder (MLS) aboard NASA Aura satellites [*Schoeberl et al.*, 2006; *Waters et al.*, 2006] and as

simulated by the GFDL AM3 model. For visualization, mean is removed for each level and normalization with respect to standard deviation is applied such that different layers have the same scale of anomalies. The oxidization of methane at ~10 hPa [*le Texier et al.*, 1988] contributes to local water vapor concentration increase thus the effect of transportation is most prominent between 100 hPa and 30 hPa. The observation of water vapor concentration near the tropopause shows a clear seasonal cycle with minimum in winter and maximum in summer, which mainly a direct result of the tropopause temperature variation [*Mote et al.*, 1996]. The water vapor positive anomaly slowly propagates upward and it takes around one year to reach 30 hPa, equivalent to ~0.23 mm/s and consistent with the tropical mean Brewer-Dobson circulation vertical speed [*Brewer*, 1949; *Flury et al.*, 2013]. Figure 5.4b shows that the model reasonably captures the same seasonal cycle at 100 hPa (i.e., ~tropical tropopause) as observed by the Aura MLS. The model also reasonably agrees with the MLS observations on the upward propagation speed.

It would be instructive to also look at the tape-recorder effect of BC transport and contrast it with the water vapor tape-recorder effect. Figure 5.5(a) shows the time-height cross section of BC anomalies over the same region. In the troposphere, positive BC anomalies are concentrated in a handful short periods in the boreal summer, highlighting the importance of deep convection in the summer monsoon season for vertical transport of the BC. Once transported into the stratosphere, BC quickly disperses horizontally and is transported upward as well by large-scale motion. The upward transport effects for water vapor and BC in the stratosphere are highlighted in Figure 5.5(b). Comparing with the constant upward transport speed for water vapor, BC shows a large spectrum of

vertical transport speed. It takes the positive BC anomaly at 100 hPa as less as about half year to propagate to 30 hPa – twice the speed of that of water vapor and as large as roughly a year which is the same to water vapor transport. It is likely due to efficient short wave heating by BC and BC is carried upward by surrounding warmed air parcels. This is supported by *de Laat et al.* [2012] who postulates that biomass burning is responsible to BC to free atmosphere (~10 km) and strong short wave absorption and the consequent warming result in the consequent dry convection through a study of BC transport during Australian bush fires. Besides the difference in speed, the vertical transports of the two species also show phase difference. BC positive anomaly at 100 hPa takes place usually after the peak of the specific humidity positive anomaly, indicating a phase lag of 2~3 months. There is a minimum of BC concentration between 2011 and 2012 which seems anti-correlated with strong positive anomaly of water vapor took place. Since the transport of water vapor is strongly influenced by the strength and frequency of deep convection and the surface BC emission is growing, the anti-correlation implies a negative feedback that limits the amount of BC transported to the stratosphere. The reason is likely that stronger convection carries larger amount of BC upward however has larger wet deposition efficiency. Therefore, the amount of BC that reaches the stratosphere can be expressed as,

$$BC_{LS} = C_1 * BC_{PBL} * \eta * (1 - \gamma_{wet}) + C_2 \tag{5.1}$$

where η is a parameter representing convective strength and γ_{wet} is wet-deposition effficiency, C_1 and C_2 are constants.

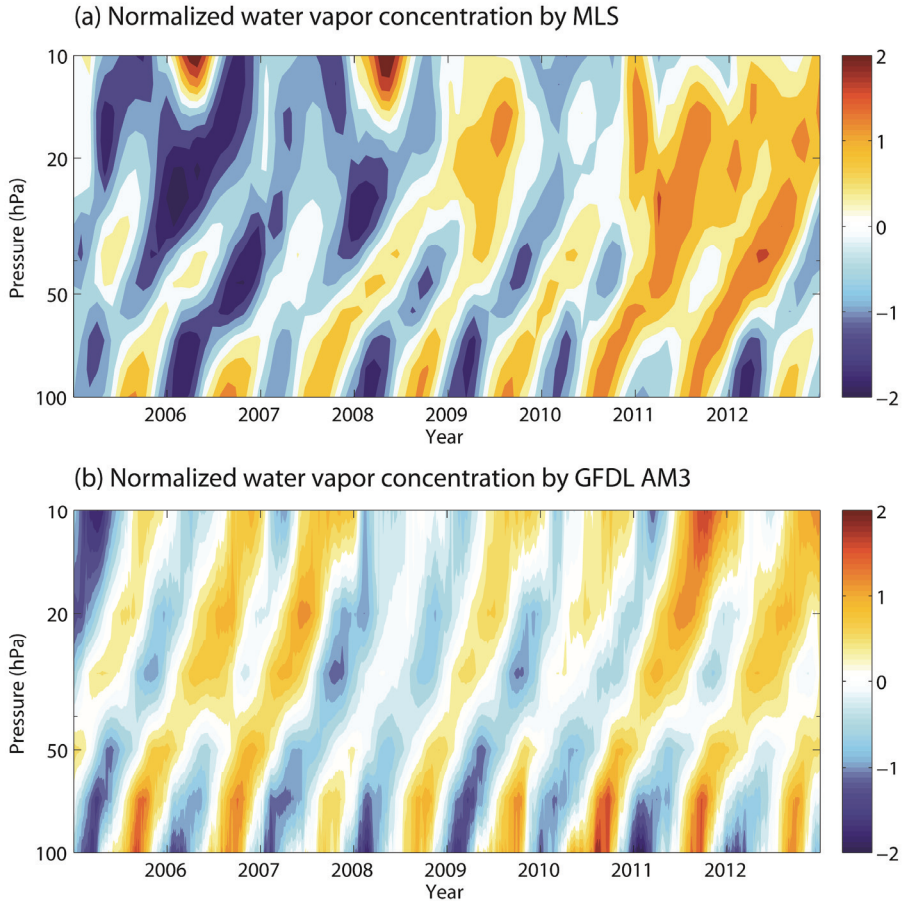

Figure 5.4 Time-height cross section of water vapor anomalies over India subcontinent. (a) from Aura MLS observation (b) from the GFDL AM3 simulation. The anomalies at each pressure level are normalized by standard deviation.

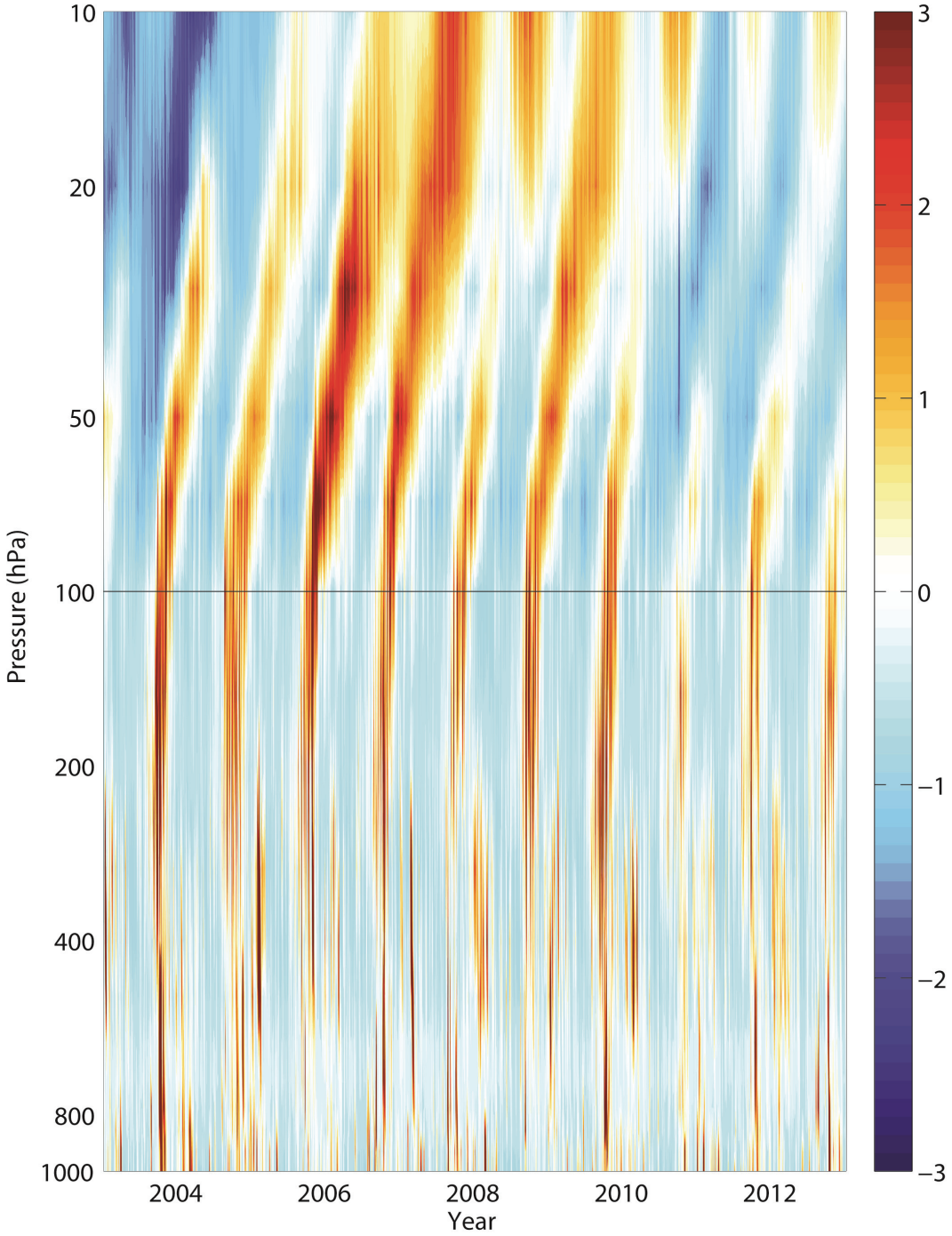

Figure 5.5 (a) Similar to Figure 5.4 except for black carbon in the troposphere and stratosphere. The level of 100 hPa is highlighted using a horizontal black line.

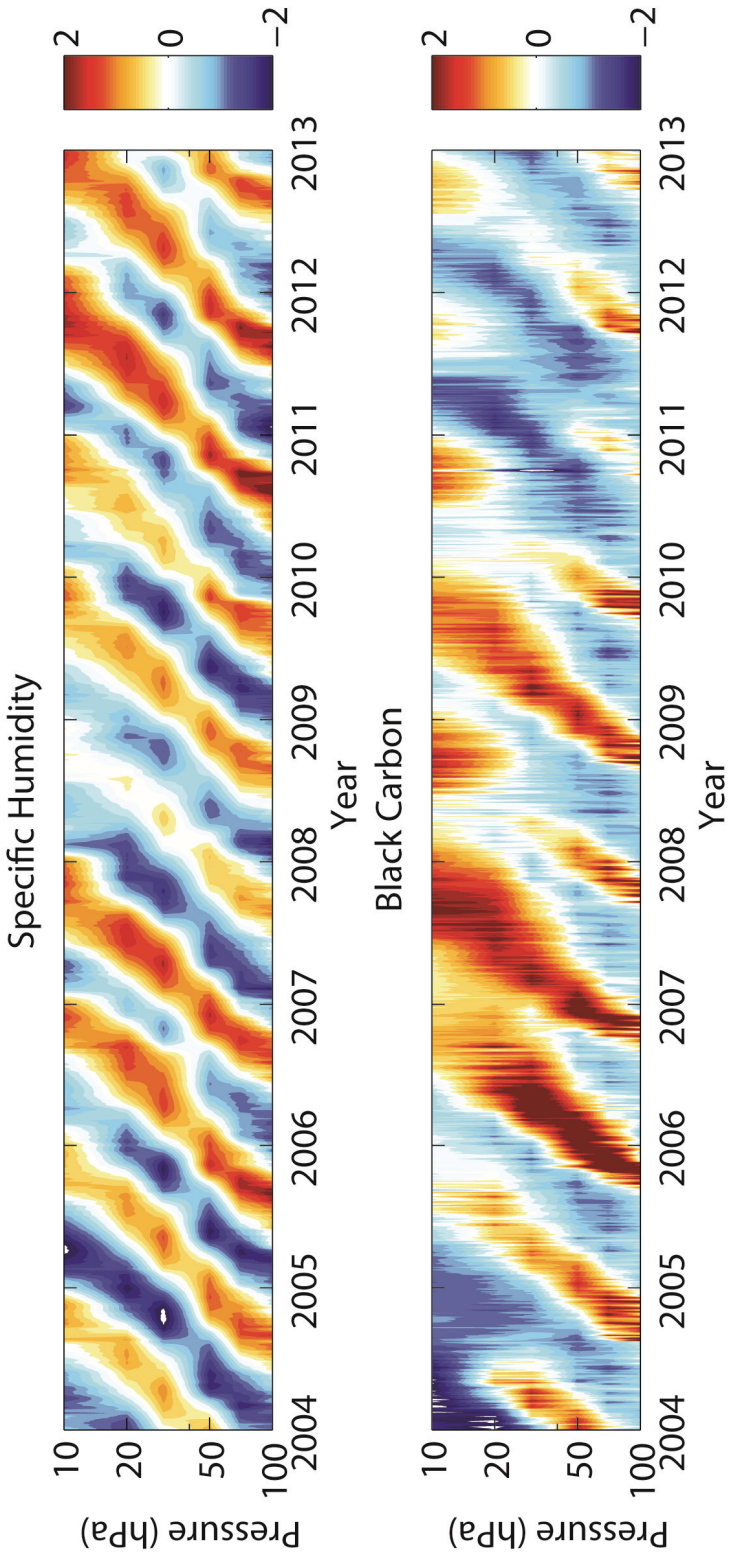

Figure 5.5 (b) Similar to Figure 5.4 but for normalized specific humidity and black carbon concentration in the stratosphere from 2004 to 2012.

5.2.3 Model simulation of vertical transport: a case study

Figure 5.6 and 5.7 presents a case study of simulated ODC event and transportation of BC into the LS. The reference time zero is when convective mass transport peaks at the level of 100 hPa. Snapshots from 6 hours prior to reference time to 18 hours after it are plotted in sequence for every 3 hours. Circles on the plot denote the grid box that the ODC occurs. Convective mass transport starts to increase since 3 hours prior to the time zero and reaches maximum at time zero, and then quickly dissipates in following 3 hours (Figure 5.7). The BC concentration 6 hours before the reference time is used as a reference concentration and BC concentration in the following steps are plotted in percentage change relative to the reference concentration (Figure 5.6). The simultaneous BC concentration remains roughly constant at 70 hPa where ODC occurs until time zero, when it quickly becomes 330% larger than the reference value within the next 3 hours. The newly lifted BC then drifts gradually westward along wind direction and, 18 hours after time zero, the increased BC concentration west to the ODC source is still visible.

The 3-h time lag between the BC increase at 70 hPa and convective signal at 100 hPa indicates a mean vertical speed of ~0.185 m/s which is two orders of magnitude larger than that of the large scale circulation and could only be explained by ODC. Figure 5.6 indicates that BC quickly disperses 3 hours after local concentration maximum and within one day, it has been already widely spread. These features are what need to be taken into account for detecting such BC increases due to ODC events. Given the small concentration of BC in the stratosphere, limb-view detection would be favored than nadir-view detection for relatively larger optical signals.

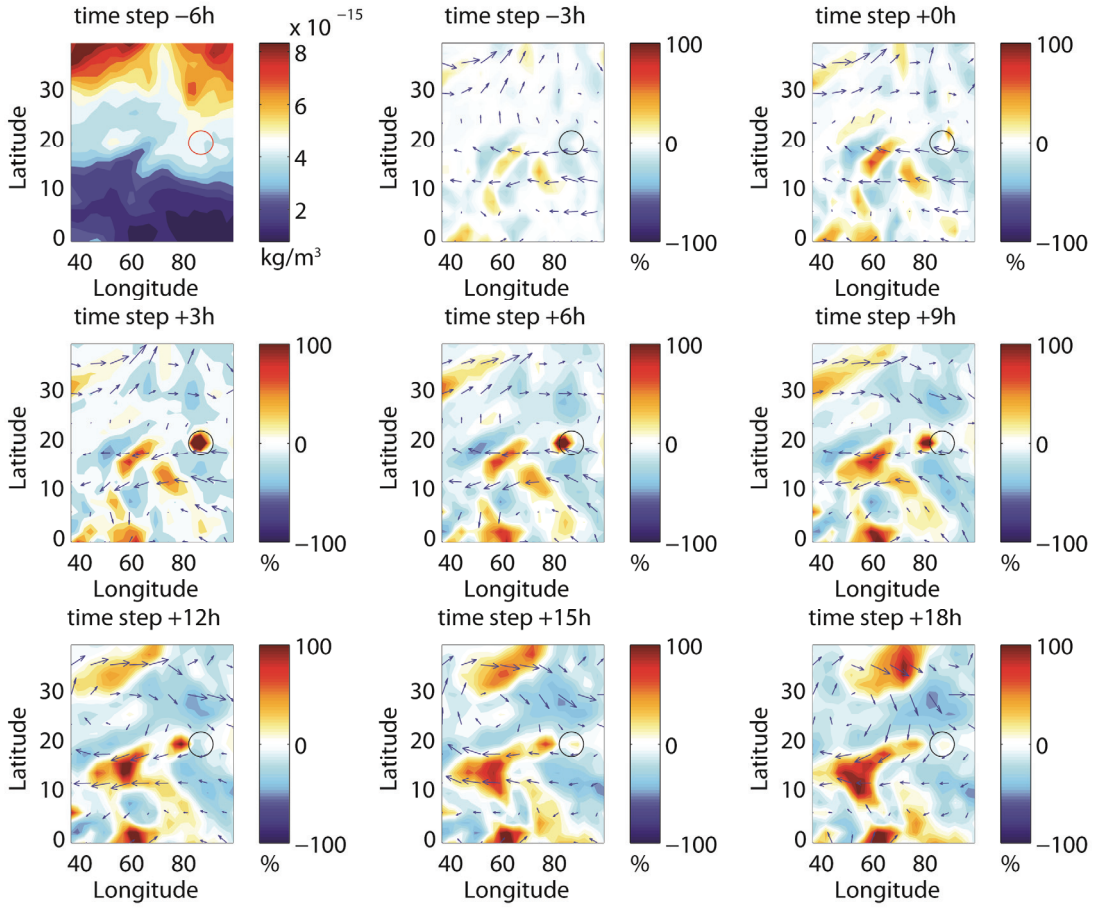

Figure 5.6 Snapshots of 70-hPa BC concentrations over Indian subcontinent when an ODC event happens at time zero. The concentration at -6 hours is plotted in absolute value. Other snapshots are plotted as relative changes with respect to the reference state at -6 hours. Open circle in each plot indicates the grid box where overshooting convection takes place.

5.3 Methodology and strategy of forward simulation

The forward radiative transfer model used in this OSSE is Moderate Transmission Code (MODTRAN) version 4.3.1 [*Berk et al.*, 1999]. It is a widely used atmospheric radiative transfer model in remote sensing community with flexible configurations of atmospheric profiles as well as viewing geometries. In this study, MODTRAN calculation is carried out at its 1 cm^{-1} spectral interval through the IR and NIR regions.

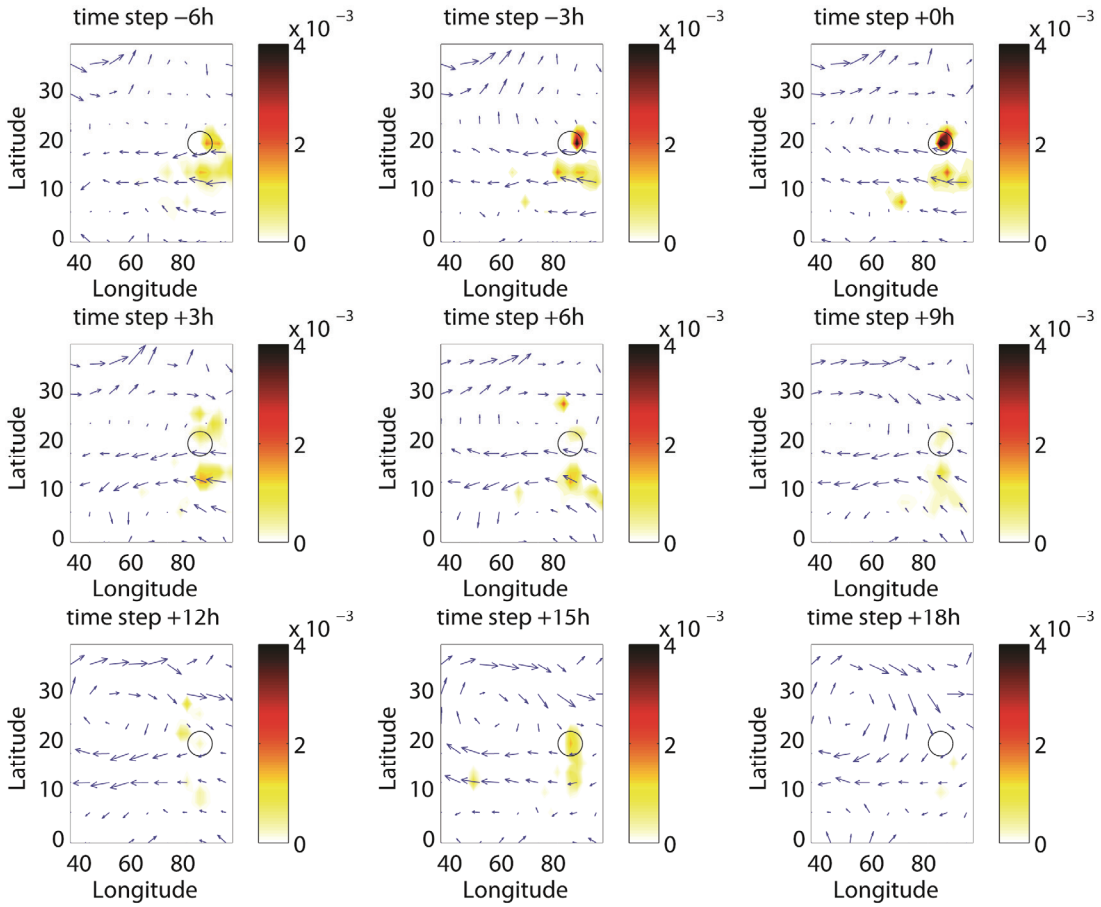

Figure 5.7 Similar to Figure 5.6 but for the 100-hPa convective mass flux in the unit of kg/m^2/s. All snapshots are plotted in the absolute value.

Inputs to MODTRAN include the AM3–simulated vertical profiles of temperature, ozone, specific humidity, BC concentration as well as BC radiative properties (Figure 5.1). MODTRAN default profiles of other absorbing gases in the tropics are used. MODTRAN is configured for limb-view geometry without solar radiance with outputs of spectral radiance and optical thickness from 700 cm^{-1} to 2000 cm^{-1}. The reason of such configuration is discussed in the following section.

5.4 Possible satellite retrieval method

Section 5.1 reviews current laboratory and in-situ methods of measuring BC and stratospheric aerosols in general as well as their limitations. In this section, we explore a different approach method to measure BC concentration in the LS using IR limb sounding.

Based on the aforementioned discussion, three factors need to be taken into account for such method. First, BC concentration is very small and decreases exponentially with altitude. Second, there are other optically active compositions such as water vapor and clouds, the optical path of which can easily dominate that of BC. Third, unlike gas spectroscopy, the spectroscopy of BC does not exhibit obviously spectral features (Figure 5.1) that quickly change with frequency and can be utilized for retrievals. Fourth, BC extinction profile is not separable from solar occultation radiance measurement.

All factors imply that limb-sounding method in the infrared window region with tangent height (the lowest level of the limb view) in the LS would be an optimal choice. The factors that makes this possible includes, (1) limb view in the stratosphere is less affected by the radiative processes in the troposphere (especially clouds), (2) the stratosphere is fairly clean without local sources of solid particles, (3) the atmosphere is transparent in the window region with limited water vapor continuum absorption, (4) BC is a strong absorber across the spectrum and efficient emitter in the infrared. In following discussion, we use the limb-view geometry with a tangent height at 16.6 km (~100 hPa for a typical tropical profile over Indian continent) with wavenumber from 700 cm^{-1} to

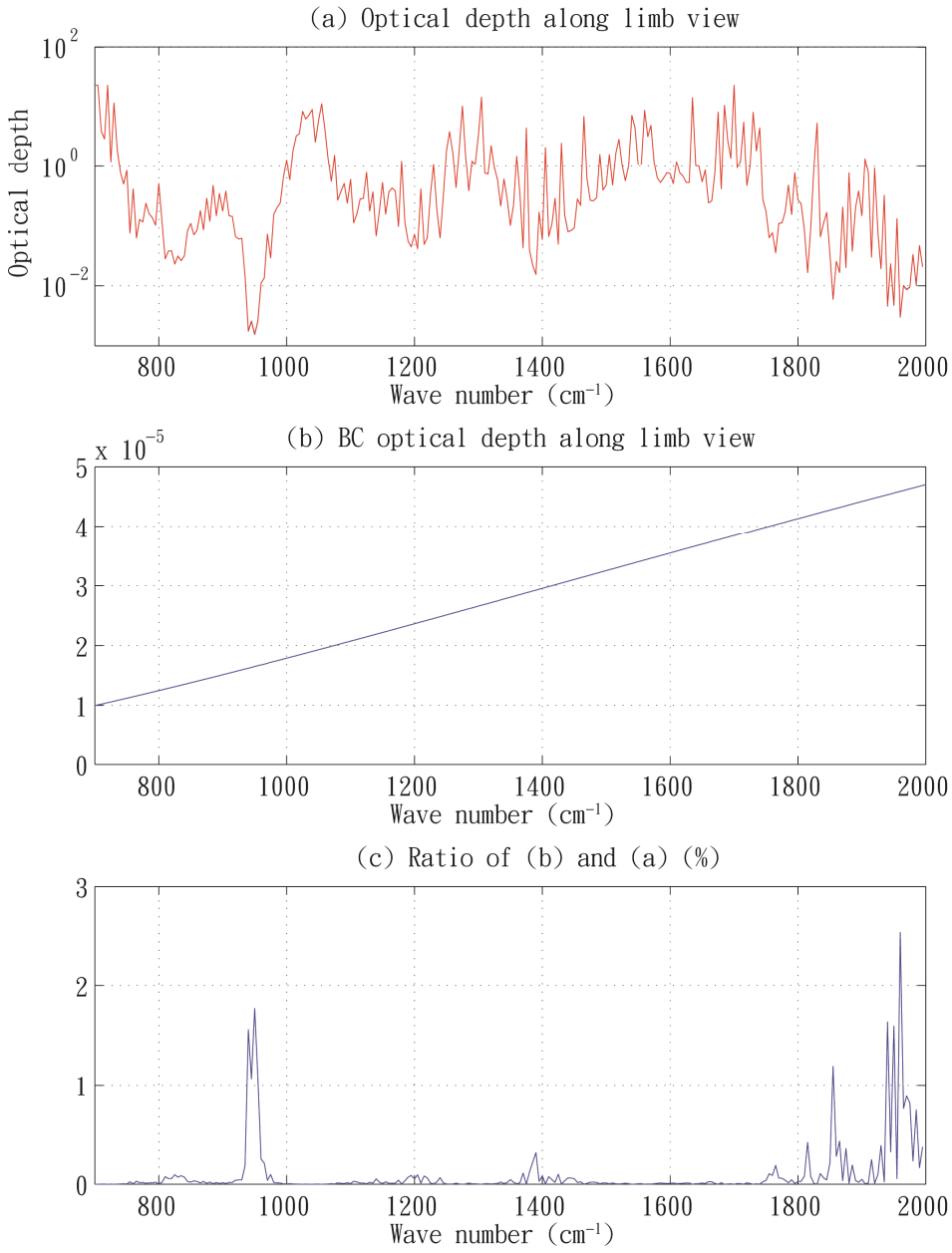

Figure 5.8 (a) the optical thickness along the limb view with tangent height of 16.6 km for the infrared band. (b) the black carbon optical thickness along limb view. (c) the fraction of total optical thickness perturbation induced by black carbon in percentage.

2000 cm^{-1}. The method is applied without the presence of the Sun in order to exclude the influence of solar radiance in the infrared band.

Figure 5.8a shows the simulated optical thickness along the limb-viewing path in the atmospheric window region without any BC. Apparently, the atmosphere is most transparent at the wave number of 940 cm^{-1} with optical thickness of around 10^{-3}. A typical AM3 output profile with large BC concentration in the stratosphere is then used to calculate BC optical thickness along the designed limb view. The ratio of the two reflects the relative change of optical thickness along the viewing path due to the existence of BC. A local maximum of ~2% is obtained at 940 cm^{-1}. The peak with wavenumber greater than 1800 cm^{-1} is strongly influenced by water vapor continuum absorption and is not as transparent as 940 cm^{-1}, therefore, is not taken into consideration.

However, at 940 cm^{-1}, the radiance measurement is also weakly affected by water continuum emission, which is determined by water vapor abundance and temperature. To circumvent this issue, one possible solution is to find another channel in the window region that has such large water vapor continuum emission and absorption that BC absorption, if any, can be ignored. The radiance in this "reference" channel can then be used to normalize radiance at 940 cm^{-1}. The rationale is that, if temperature or water vapor abundance change, it would lead to similar percentage change in both channels. But if BC is transported into the LS by the ODC event, it would influence 940 cm^{-1} in noticeable way but not for the "reference" channel.

By carrying out MODTRAN simulations using large amount of profiles from the AM3 simulation and correlating the simulated radiance in each window channel with the

BC concentration, we found that 1210 cm^{-1} is the channel least affected by the BC concentration and sensitive to only water vapor continuum not other trace gas absorptions. Thus we define the ratio of radiance (RoR) as

$$RoR = \frac{\mathrm{I}(\nu_1 = 940\,\mathrm{cm}^{-1})}{\mathrm{I}(\nu_2 = 1210\,\mathrm{cm}^{-1})} \tag{5.2}$$

where as usual *I* stands for spectral radiance.

We carry out a sensitivity study to confirm the relationship between RoR and BC. Using a set of mean profiles of temperature, ozone and BC are used as reference states, we vary the BC concentrations between 16.6 km (~100 hPa) and 18.7 km (~70 hPa) artificially by a factor varying from 0.1 to 50. RoR is then derived through MODTRAN calculation and is plotted against the BC concentration at 16.6 km (black dots in Figure 5.9). The slope of the curve indicates that RoR is most sensitive to BC when BC is greater 10^{-13} kg/m^3 and least sensitive when BC concentration is smaller than 10^{-14} kg/m^3. Therefore, we tentatively set the threshold of the detection limit be 10^{-14} kg/m^3. The simulation cases with BC concentration above this value are highlighted with red cycles and they follow a nice linear relationship with R^2 being nearly one. Note that the y-axis value is in log-scale for illustration purpose.

Sensitivity tests of the influence of temperature and water vapor concentration to the linear relationship are likewise carried out. The blue solid (dashed) line in Figure 5.9 is derived with varying BC concentration in similar manner as for the black dots except with 50% less (more) water vapor between 16.6 km and 18.7 km than the reference state. This is to take the (de)hydration process by ODC in the LS into consideration. Similarly,

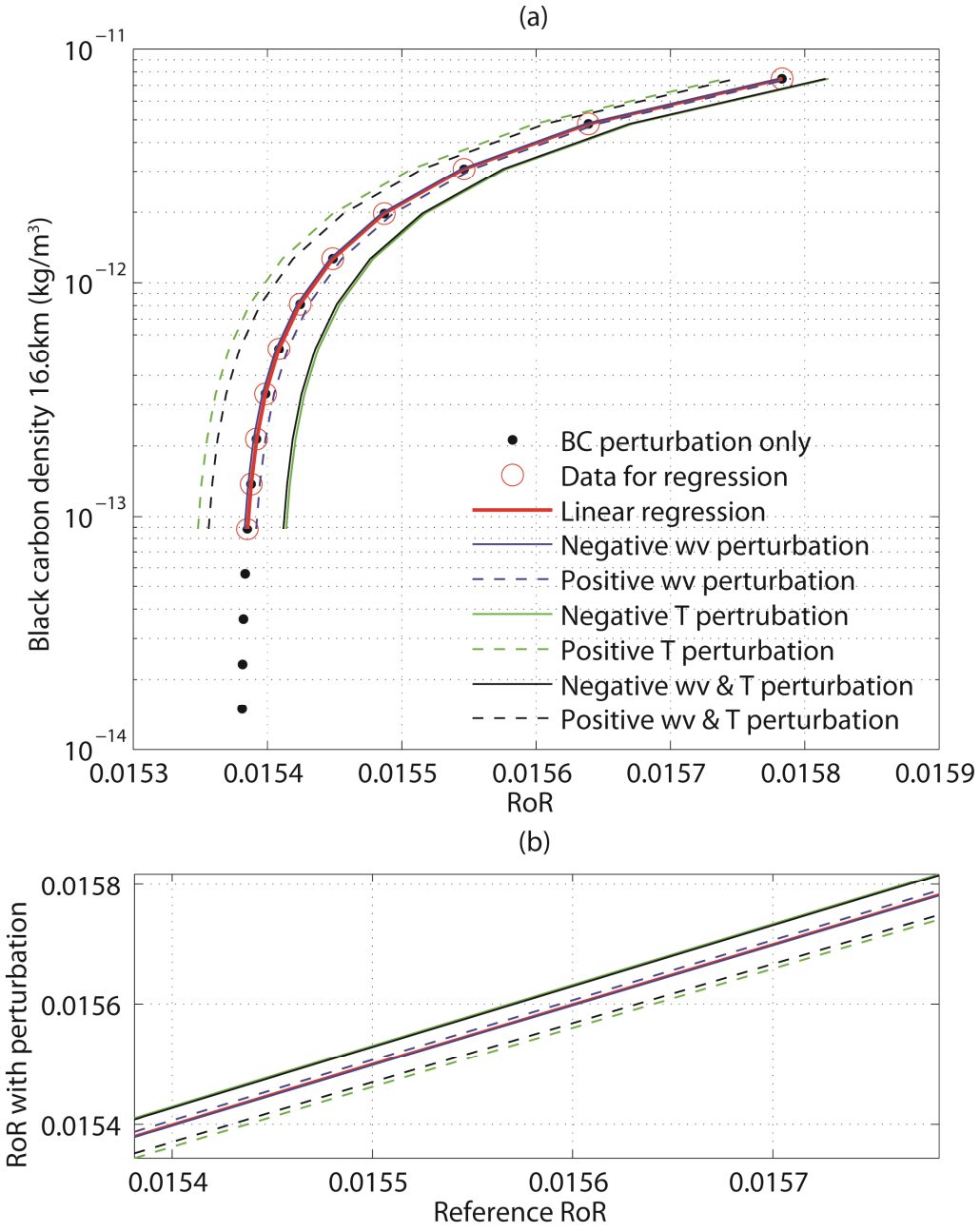

Figure 5.9 (a) Ideal test case of the relationship between BC concentration at 16.6 km and the ratio of radiance between 940 and 1210 cm^{-1}. The red cycles indicates the data point used for regression and the regression result is the red line. Sensitivity test for temperature (T) and water vapor (wv) are conducted with solid and dashed lines of negative and positive perturbation, respectively. The blue lines indicate additional 50% change of water vapor between 16.6 and 18.7 km only. The green lines are cases with 1-K temperature perturbation. The black lines are with both kinds of perturbation. (b) The simulation results with perturbed profiles are plotted against the one using reference atmospheric state. The regression line (red) is plotted against itself for comparison purpose.

the green solid (dashed) line shows the profile with temperature of the stratosphere (100~1 hPa) perturbed to 1 K warmer (cooler). The simulation with perturbed water vapor or temperature or the two combined are plotted against the one using reference atmospheric state (black dots in Figure 5.9a) in Figure 5.9b.

Sensitivity test indicates that stratospheric temperature and water vapor concentration perturbation within reasonable ranges would linearly shift the linear relationship between BC and RoR and preserve the slope of the linear profile. Additionally, temperature change shows stronger influence than water vapor change in the LS. Noteworthily, the effect of water vapor and temperature perturbation are independent to each other since the black lines shift the profile numerically equivalent to the sum of the shift of the two independent perturbations. For example, the difference of shift between the red solid line and black dashed line is the sum of the shift between the blue/green dashed lines and the red line.

To further illustrate the influence of stratospheric temperature and water vapor in the LS to the linear relationship, a 2-D lookup table of the change of intercept is constructed and is color-coded in Figure 5.10. The value indicates the difference in RoR given the same amount of BC in the stratosphere with different ambient condition (i.e., stratospheric temperature and specific humidity). Therefore, the amount of shift for each calculation in the future can be obtained from the look-up table using the change in ambient condition from the reference state. The reference vertical mean temperature from 100 hPa to 1 hPa is 211.45 K and the layer mean specific humidity between 16.6 and 18.7 km is 2.43×10^{-6} kg/m^3. This figure largely confirms the independence between the influence of stratospheric temperature and water vapor in the LS. We notice that the

influence of stratospheric temperature change shows a non-monotonic pattern with a minimum when the stratosphere is 2 K warmer. Because temperature directly changes the extinction coefficient of water vapor continuum, we suspect that the pattern results from the difference in the water vapor continuum extinction coefficient in the two wave numbers, which will be verified in further analysis.

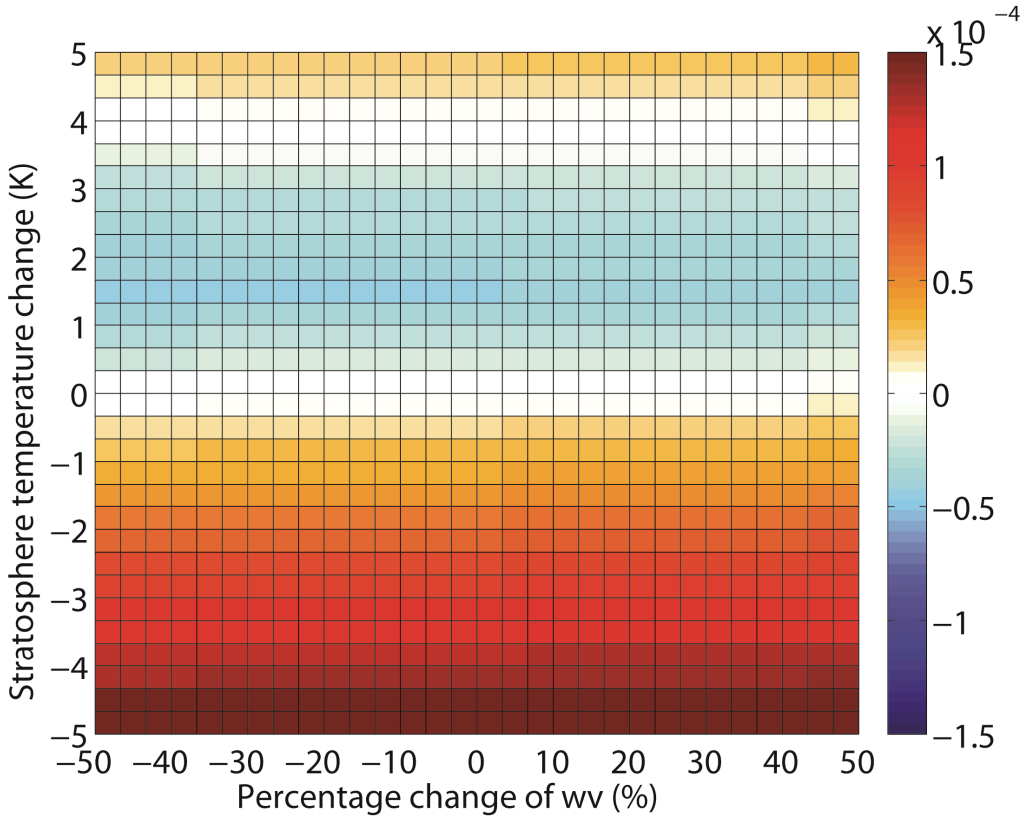

Figure 5.10 Color-coded lookup table of the intercept deviation from the linear relationship derived from the reference state.

5.5 Applicability of the method

For each day during the simulation year of 2000 and 2001, the case with maximum BC concentration at 16.6 km over the region of interest is identified as a sample and its vertical profile of temperature, specific humidity, ozone, and BC are fed into MODTRAN. The time series of BC at 16.6 km, radiance at 940 and 1210 cm^{-1} simulated by MODTRAN, and their ratio (RoR) are plotted together in Figure 5.11a and 5.11b. The radiance time series show no similarities with the BC time series. In contrast, RoR closely follows the seasonal pattern of BC and responds well to the extreme cases. This confirmed the aforestated argument that the RoR makes the signal from BC emission stands out.

Based on Figure 5.9, there exists a linear relationship between BC and RoR, expressed as,

$$BC = a(RoR + dRoR) + b \tag{5.3}$$

where a (=1.856×10^{-8} kg/m^3) and b (=-2.855×10^{-10} kg/m^3) are obtained from the regression result in Figure 5.9. dRoR denotes the shift of pattern due to ambient temperature and humidity change and is obtained using the look-up table in Figure 5.10. Because the relationship is based on the thermal emission of BC, it is beyond the algorithm detection limit when BC concentration is considerably small. Therefore, the algorithm detection limit set to 10^{-14} kg/m^3 (Figure 5.9). The horizontal resolution of the method is obtained based on the corresponding weighting function of the limb-view radiance measurement at 940 cm^{-1} which sharply decreases beyond the height of 18.7 km. A simple calculation shows that the detection method is most sensitive to the area within

160 km (~1.5 degrees) from the tangent point of the limb view, indicating that transportation by large convective systems is easier to be identified. When BC at 16.6 km is obtained, a vertical profile of BC can be then constructed assuming that BC decreases exponentially with altitude in the stratosphere.

The retrieval method is first tested to BC profiles over the Sahara desert (19~25^{o}N, 18.75~26.25^{o}E) where BC in the LS is one order of magnitude smaller than that over Indian subcontinent and then to BC profiles 2012~2013 over Indian subcontinent. Figure 5.12 and 5.13 demonstrates that Equation 5.3 performs consistently with temporal and geographical change. However, there are sizeable amount of false detection of sporadic event in boreal spring and the method consistently overestimate the BC concentration around the 270th day of each year. This implies some of the variability is not captured in the linear model. For example, preliminary results show that when ambient warming and cooling are not uniform in the stratosphere, the shift of pattern in Figure 5.9 slightly differs.

The advantage of this detection method is the sensitivity to the small amount of BC by virtue of the high transparency in the window region. Compared with solar occultation, the limb view can cover a sizeable portion of the horizon, providing a straightforward way to globally monitoring BC reservoir at the lower stratosphere and BC transport by ODC across the tropopause especially over India.

This chapter is a proof-of-idea study, providing a possibility to retrieval BC concentration at lower stratosphere and potentially shed light on mass transport. However, this attempt is intrinsically vulnerable to a number of uncerntainties. To name a few,

when a vertical profile is input into MODTRAN, it is assumed that it is uniform around the Earth because MODTRAN is not capable to take in all the profiles along the viewing path. Besides, a large uncertainty comes from clouds. The radiative relationship used in this chapter will be different when convective clouds present at 16.6 km which is, however, very infrequent. Even the cloud top stops below 16.6 km, its presence would also possibly alter the relationship. The effect is to be interpreted and quantified in future study.

5.6 Conclusions

This chapter introduces the mass transport of overshooting deep convection (ODC), through which PBL air is carried to the tropopause and into the LS. Two of species within the air, water vapor and black carbon, are able to strongly perturb the chemical and radiative balance in the stratosphere. The transport of water vapor into the stratosphere is well documented and is shown to largely modulated by the temperature of the tropopause. In contrast, BC transport is strongly associated with tropospheric BC concentration and the frequency of ODC. A global survey shows that the effect of ODC transport of BC to the LS is most significant over Indian subcontinent during summer. The vertical transport of BC in the stratosphere is shown to be as large as twice the transport of water vapor, which is speculated to be the result of efficient shortwave heating.

The transportation mechanism of ODC to the stratosphere has been speculated in several literatures. However, no observational evidence has been published, which is due to the difficulty of BC measurement in noisy background. This chapter proposes to use an

IR limb-viewing method with tangent height of 16.6 km. The ratio of the radiance profiles at 940 cm^{-1} and 1210 cm^{-1} is shown to linearly correlate with BC at 16.6 km. The atmosphere at 940 cm^{-1} along the limb view is so transparent that the radiance profile captures the emission from BC when its concentration at 16.6 km is greater than 10^{-14} kg/m^3. The signature of water vapor continuum in the at 940 cm^{-1} radiance profiles is minimized by normalization using radiance profiles at 1210 cm^{-1}, which makes the signal of BC identifiable. An emprical relationship between BC and RoR are derived and with consideration of the influence of ambient temperature and humidity changes. The method is then tested in different locations and times and has shown consistent performances in capturing seasonal cycles and cases with large BC concentration. Further model refinement is needed in future study to reduce false detection especially in boreal spring.

5.7 Acknowledgements

The GFDL AM3 data set is generated by Dr. Xianglei Huang. The 5-year tropical overshooting convection observed by A-Train satellites is provided by Dr. Johnny Luo. The AIRS MLS data set is obtained through the Atmospheric Composition Data and Information Services Center (ACDISC) at http://disc.gsfc.nasa.gov/acdisc.I would like to thank Dr. Xiuhong Chen for helpful discussions and instructions in setting up the radiative transfer model. This research is supported by the NASA MAP project under grant NNX09AJ46G awarded to the University of Michigan.

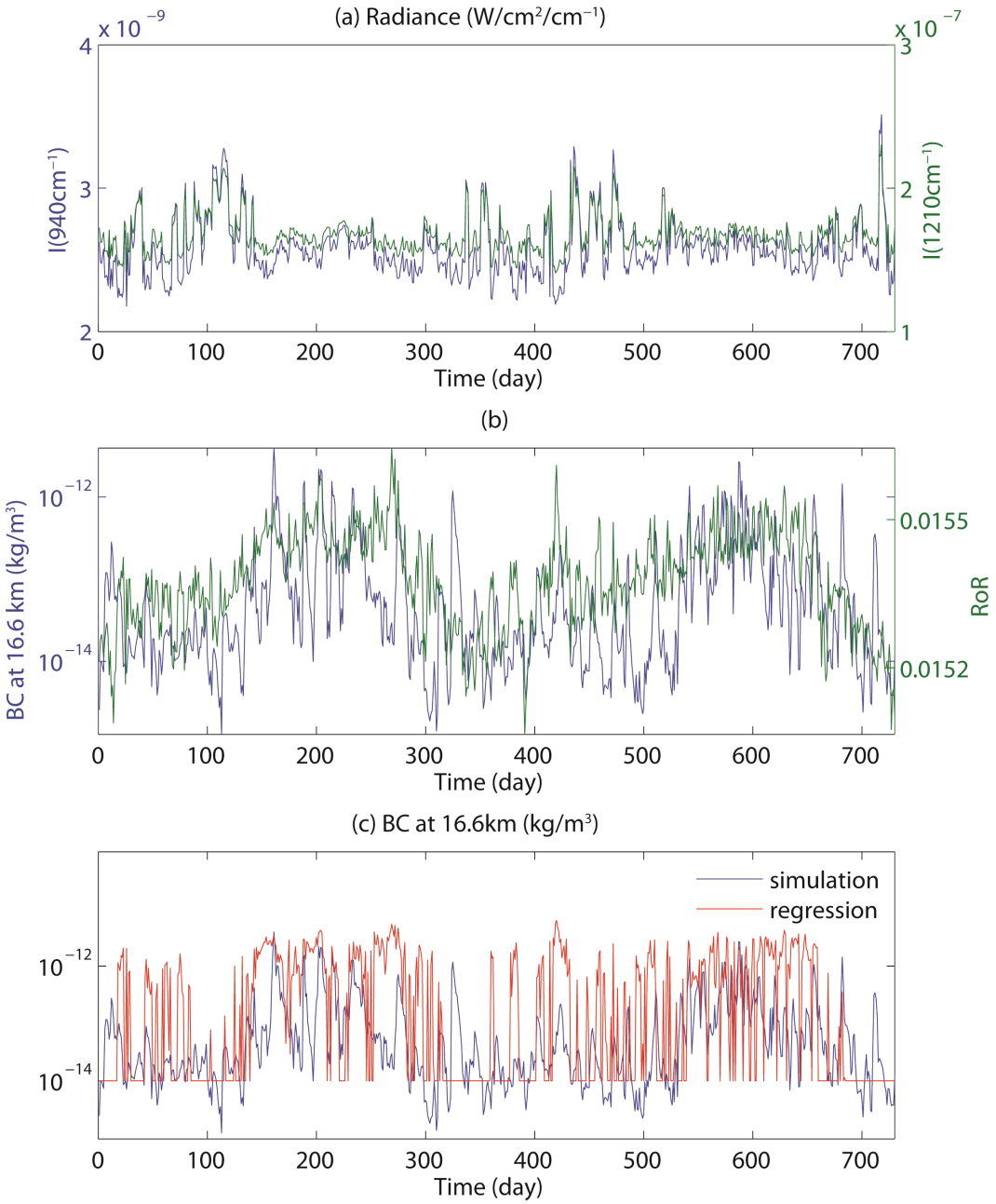

Figure 5.11 (a) time series of radiance measurement at two selected wave numbers. Time step starts from the first day of 2000. (b) The blue line is the black carbon concentration at 16.6 km and the green line the simulated RoR for profiles over India in the year of 2000~2001. The regression result is the red line and is applied to estimated black carbon concentration in (c).

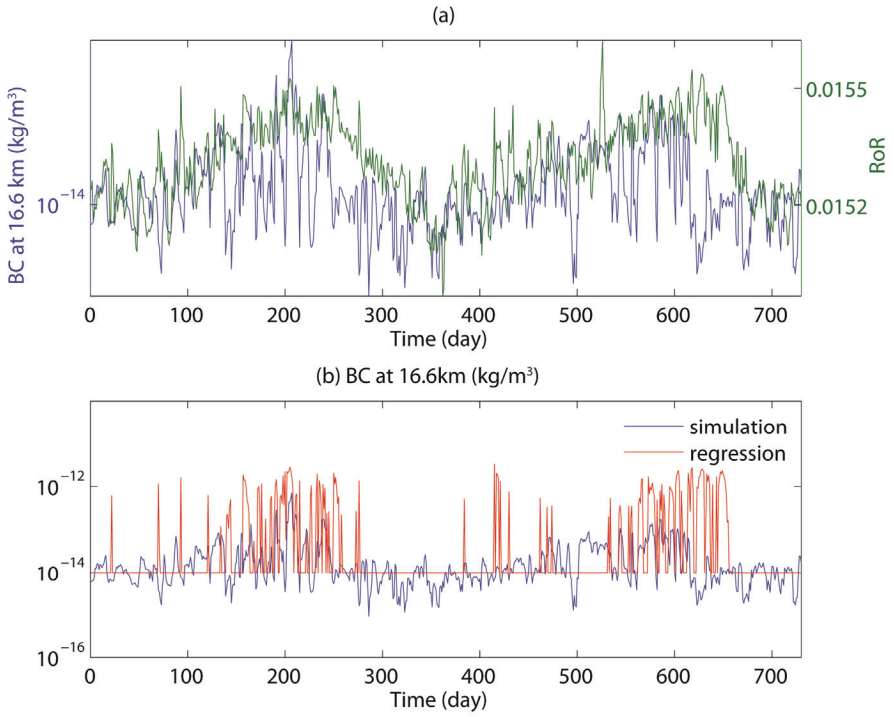

Figure 5.12 Similar to Figure 5.11 but for profiles over Sahara desert in the year of 2000~2001.

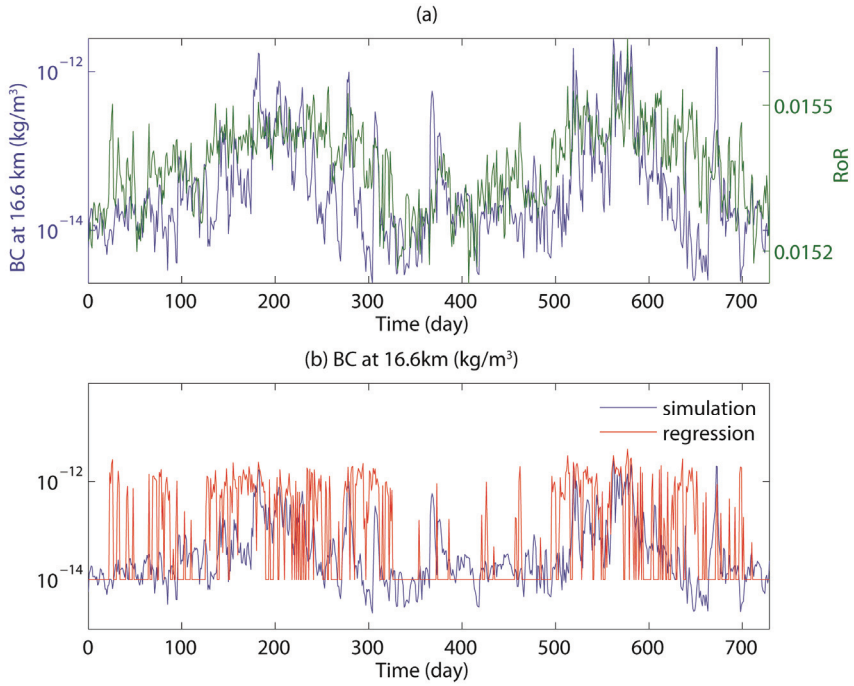

Figure 5.13 Similar to Figure 5.11 but for profiles over India for the year of 2012~2013.

References:

Ackerman, A.S., O.B. Toon, D.E. Stevens, A.J. Heymsfield, V. Ramanathan, E.J. Welton (2000), Reduction of tropical cloudiness by soot, *Science*, 288, pp. 1042–1047.

Anderson, J. L., et al. (2004), The new GFDL global atmosphere and land model AM2–LM2: Evaluation with prescribed SST simulations, *J. Climate*, 17(24), 4641–4673, doi:10.1175/JCLI-3223.1.

Anderson, J. G., D. M. Wilmouth, J. B. Smith, and D. S. Sayres (2012), UV dosage levels in summer: Increased risk of ozone loss from convectively injected water vapor, *Science*, 337, 835–839, doi:10.1126/science.1222978.

Babu, S. S., K. K. Moorthy, R. K. Manchanda, P. R. Sinha, S. K. Satheesh, D. P. Vajja, S. Srinivasan, and V. H. A. Kumar (2011), Free tropospheric black carbon aerosol measurements using high altitude balloon: Do BC layers build "their own homes" up in the atmosphere? *Geophys. Res. Lett.*, 38, L08803, doi:10.1029/2011GL046654.

Bannister, R. N., O'neill, A., Gregory, A. R. and Nissen, K. M. (2004), The role of the south-east Asian monsoon and other seasonal features in creating the 'tape-recorder' signal in the Unified Model, *Q.J.R. Meteorol. Soc.*, 130: 1531–1554. doi: 10.1256/qj.03.106.

Berk, A., G. Anderson, P. Acharya, J. Chetwynd, L. Bernstein, E. Shettle, M. Matthew, and S. Adler-Golden (1999), *MODTRAN4 User's Manual*, Air Force Res. Lab., Hanscom AFB, Mass.

Berkowitz, C.M., et al. (2000), Evidence of nighttime ozone depletion through heterogeneous chemistry, *Atmos. Environ.*, 35 (2000), pp. 2395–2404

Bohren, C. F. & Huffman, D. R. (1983), *Absorption and Scattering of Light by Small Particles*. New York: Wiley.

Bond, T. C., C. Zarzycki, M. G. Flanner, and D. M. Koch (2011), Quantifying immediate radiative forcing by black carbon and organic matter with the Specific Forcing Pulse, Atmos, *Chem. Phys.*, 11, 1505-1525, doi:10.5194/acp-11-1505-2011.

Bond, T. C., et al. (2013), Bounding the role of black carbon in the climate system: A scientific assessment, *J. Geophys. Res.*, 118, 5380-5552, doi: 10.1002/jgrd.50171.

Brewer, A. W. (1949), Evidence for a world circulation provided by measurements of helium and water vapor distribution in the stratosphere, *Q. J. R. Meteorol. Soc.*, 75, 351–363.

Chung, S. H., and J. H. Seinfeld (2002), Global distribution and climate forcing of carbonaceous aerosols, *J. Geophys. Res.*, 107(D19), 4407, doi:10.1029/2001JD001397.

Cormier, J. G., J. T. Hodges, and J. R. Drummond (2005), Infrared water vapor continuum absorption at atmospheric temperatures, *J. Chem. Phys.*, 122(11).

de Laat, A.T.J. de Laat, D.C. Stein Zweers, R. Boers, O.N.E. Tuinder (2012), A solar escalator: observational evidence of the self-lifting of smoke and aerosols by absorption of solar radiation in the February 2009 Australian Black Saturday plume, *J. Geophys. Res.*, 117, p. D04204

Delworth, T. D., et al. (2006), GFDL's CM2 global coupled climate models. Part I: Formulation and simulation characteristics, *J. Climate*, 19,643–674.

Disselkammp, R.S., et al. (2000), Ozone loss in soot aerosols, *J. Geophys. Res.*, 105, 9767–9771

Donner, Leo J., et al. (2011), The Dynamical Core, Physical Parameterizations, and Basic Simulation Characteristics of the Atmospheric Component AM3 of the GFDL Global Coupled Model CM3, *J. Climate*, 24, 3484–3519.

Dubovik, Oleg, Brent Holben, Thomas F. Eck, Alexander Smirnov, Yoram J. Kaufman, Michael D. King, Didier Tanré, Ilya Slutsker (2002), Variability of Absorption and Optical Properties of Key Aerosol Types Observed in Worldwide Locations, *J. Atmos. Sci.*, 59, 590–608.

Ernst, F., von Savigny, C., Rozanov, A., Rozanov, V., Eichmann, K.-U., Brinkhoff, L. A., Bovensmann, H., and Burrows, J. P. (2012), Global stratospheric aerosol extinction profile retrievals from SCIAMACHY limb-scatter observations, *Atmos. Meas. Tech. Discuss.*, 5, 5993-6035.

Flanner, M. G., C. S. Zender, J. T. Randerson, and P. J. Rasch (2007), Present day climate forcing and response from black carbon in snow, *J. Geophys. Res.*, 112, D11202, doi:10.1029/2006JD008003.

Flanner, M. G., X. Liu, C. Zhou, J. E. Penner, and C. Jiao (2012), Enhanced solar energy absorption by internally-mixed black carbon in snow grains, *Atmos. Chem. Phys.*, 12, 4699-4721, doi:10.5194/acp-12-4699-2012.

Flanner, M. G. (2013), Arctic climate sensitivity to local black carbon, *J. Geophys. Res.*, 118, 1840-1851, doi:10.1002/jgrd.50176.

Flury, T., Wu, D. L., and Read, W. G. (2013), Variability in the speed of the Brewer–Dobson circulation as observed by Aura/MLS, *Atmos. Chem. Phys.*, 13, 4563-4575, doi:10.5194/acp-13-4563-2013.

Fromm, M., R. Bevilacqua, R. Servranckx, J. Rosen, J. P. Thayer, J. Herman, and D. Larko (2005), Pyro-cumulonimbus injection of smoke to the stratosphere: Observations and impact of a super blowup in northwestern Canada on 3–4 August 1998, *J. Geophys. Res.*, 110, D08205, doi:10.1029/2004JD005350.

Fu, R., et al. (2006), Short circuit of water vapor and polluted air to the global stratosphere by convective transport over the Tibetan Plateau, *Proc. Natl. Acad. Sci. U. S. A.*, 103, 5664–5669.

Haywood, J. M., and K. P. Shine (1995), The effect of anthropogenic sulfate and soot aerosol on the clear sky planetary radiation budget, *Geophys. Res. Lett.*, 22, 603–605.

Holton, J. R., Haynes, P. H., McIntyre, M. E., Douglass, A. R., Rood, R. B., and Pfister, L. (1995), Stratosphere-troposphere exchange, *Rev. Geophys.*, 33, 403–439.

Houze, R.A., and A. K. Betts (1981), Convection in GATE, *Rev. Geophys.*, 19, 541–576.

Gao, R. S., S. R. Hall, W. H. Swartz, J. P. Schwarz, J. R. Spackman, L. A. Watts, D. W. Fahey, K. C. Aikin, R. E. Shetter, and T. P. Bui (2008), Calculations of solar shortwave heating rates due to black carbon and ozone absorption using in situ measurements, *J. Geophys. Res.*, 113, D14203, doi:10.1029/2007JD009358.

Gettelman, A., D. E. Kinnison, T. J. Dunkerton, and G. P. Brasseur (2004), Impact of monsoon circulations on the upper troposphere and lower stratosphere, *J. Geophys. Res.*, 109, D22101, doi:10.1029/2004JD004878.

Giorgi, F., and W. L. Chameides (1985), The rainout parameterization in a photochemical model, *J. Geophys. Res.*, 90, 7872–7880.

Gundel, L. A., R. L. Dod, H. Rosen, and T. Novakov (1984), The relationship between optical attenuation and black carbon concentration for ambient and source particles, *Sci. Total Environ.*, 26, 197–202.

Hansen, A.D.A., H. Rosen, T. Novakov (1984), The aethalometer — An instrument for the real-time measurement of optical absorption by aerosol particles, *Sci. Total Environ.*, 36, 191-196.

Haywood, J. M., and V. Ramaswamy (1998), Global activity studies of the direct forcing due to anthropogenic sulfate and black carbon aerosols, *J. Geophys. Res.*, 103, 6043–6058.

Heintzenberg, J. (1982), Size-segregated measurements of particulate elemental carbon and aerosol light absorption at remote arctic locations, *Atmos. Environ.*, 16, 2461–2469.

Hitzenberger, R., U. Dusek, and A. Berner (1996), Black carbon measurements using an integrating sphere, *J. Geophys. Res.*, 101(D14), 19,601–19,606.

Hofmann, D.J., S. Solomon (1989), Ozone destruction through heterogeneous chemistry following the eruption of El Chichon, *J. Geophys. Res.*, 94, pp. 5029–5041.

Holben, B. N., et al. (2001), An emerging ground-based aerosol climatology: Aerosol optical depth from AERONET, *J. Geophys. Res.*, 106(D11), 12067–12097.

Jacob, D. J., et al. (2010), The Arctic Research of the Composition of the Troposphere from Aircraft and Satellites (ARCTAS) mission: Design, execution, and first results, *Atmos. Chem. Phys.*, 10, 5191–5212.

Jacobson, M. Z. (2000), A physically-based treatment of elemental carbon optics: Implication for global direct forcing of aerosols, *Geophys. Res. Lett.*, 27, 217–220.

Jacobson, M. Z. (2001a)Strong radiative heating due to the mixing state of black carbon in atmospheric aerosols, *Nature*, 409, 695–697.

Jacobson, M. Z. (2001b), Global direct radiative forcing due to multicomponent anthropogenic and natural aerosols, *J. Geophys. Res.*, 196,1551–1568.

Kamm, S., et al. (1999), The heterogeneous reaction of ozone with soot aerosol, *Atmos. Environ.*, 33, 4651–4661

Kaspari, S. D., M. Schwikowski, M. Gysel, M. G. Flanner, S. Kang, S. Hou, and P. A. Mayewski (2011), Recent increase in black carbon concentrations from a Mt. Everest ice core spanning 1860–2000 AD, *Geophys. Res. Lett.*, 38, L04703.

Kirchstetter T. W., T. Novakov (2007), Controlled generation of black carbon particles from a diffusion flame and applications in evaluating black carbon measurement methods, *Atmospheric Environment*, 41, 9,1874-1888.

Koch, D., et al. (2009), Evaluation of black carbon estimations in global aerosol models, *Atmos. Chem. Phys.*, 9, 9001–9026.

Lamarque, J.-F., and Coauthors, (2010), Historical (1850–2000) gridded anthropogenic and biomass burning emissions of reactive gases and aerosols: Methodology and application, *Atmos. Chem. Phys. Discuss*., 10, 4963–5019.

le Texier, H., Solomon, S. and Garcia, R. R. (1988), The role of molecular hydrogen and methane oxidation in the water vapour budget of the stratosphere, *Q.J.R. Meteorol. Soc.*, 114: 281–295.

Lee, Y. H., et al., (2013), Evaluation of preindustrial to present-day black carbon and its albedo forcing from Atmospheric Chemistry and Climate Model Intercomparison Project (ACCMIP), *Atmos. Chem. Phys.*, 13, 2607-2634.

Lenoble, J., Pruvost, P., and Brogniez, C. (1984), SAGE satellite observations of stratospheric aerosols from Mount St. Helens eruption: a two wavelength analysis, *J. Geophys. Res.*, 89, 11666– 11676.

Lin, S. J. (2004), A "vertically Lagrangian" finite-volume dynamical core for global models, *Mon. Weather Rev.*, 132(10), 2293–230.

Lindberg, J. D., R. E. Douglass, and D. M. Garvey (1999), Atmospheric particulate absorption and black carbon measurement, *Appl. Opt.*, 38,2369–2376.

Lindberg, J. D. (1975), The composition and optical absorption coefficient of atmospheric particulate matter, *Opt. Quantum Electron.*, 7, 131-139.

Lindberg, J. D., R. E. Douglass, and D. M. Garvey (1993), Carbon and the optical properties of atmospheric dust, *Appl. Opt.*, 32, 6077-6081.

Liou, K. N., Y. Takano, Q. Yue, and P. Yang (2013), On the radiative forcing of contrail cirrus contaminated by black carbon, *Geophys. Res. Lett.*, 40, 778–784.

Lumpe, J. D., Bevilacqua, R. M., Hoppel, K. W., Krigman, S. S., Kriebel, D. L., Randall, C. E., Rusch, D. W., Brogniez, C., Ramananaherosa, R., Shettle, E. P., Olivero, J. J., Lenoble, J., and Pruvost, P. (1997), POAM II retrieval algorithm and error analysis, *J. Geophys. Res.*, 102, 23593–23614.

Manoj M. J., et al. (2006), On the influence of stratospheric water vapor changes on the tropospheric circulation, *Geophys. Res. Lett.*, 33, 9.

McConnell, J. R., R. Edwards, G. L. Kok, M. G. Flanner, C. S. Zender, E. S. Saltzman, J. R. Banta, D. R. Pasteris, M. M. Carter, and J. D. W. Kahl (2007), 20th Century industrial black carbon emissions altered Arctic climate forcing, *Science*, 317, 1381-1384.

McCormick, M. P. and Trepte, C. R. (1986), SAM II measurements of Antarctic PSC's and aerosols, *Geophys. Res. Lett.*, 13, 1276–1279.

McCormick, M. P. and Veiga, R. E. (1992), SAGE II measurements of early Pinatubo aerosols, *Geophys. Res. Lett.*, 19, 155–158.

McDermid, I. S., T. D. Walsh, A. Deslis, and M. L. White (1995), Optical systems design for a stratospheric lidar, *Appl. Opt.*, 34, 6201–6210.

Menon, S., J. Hansen, L. Nazarenko, Y.F. Luo (2002), Climate effects of black carbon aerosols in China and India, *Science*, 297, pp. 2250–2253.

Mote, P. W., K. H. Rosenlof, M. E. McIntyre, E. S. Carr, J. C. Gille, J. R. Holton, J. S. Kinnersley, H. C. Pumphrey, J. M. Russell III, and J. W. Waters (1996), An atmospheric tape recorder: The imprint of tropical tropopause temperatures on stratospheric water vapor, *J. Geophys. Res.*, 101(D2), 3989–4006.

Moteki, N., Y. Kondo, N. Oshima, N. Takegawa, M. Koike, K. Kita, H. Matsui, and M. Kajino (2012), Size dependence of wet removal of black carbon aerosols during transport from the boundary layer to the free troposphere, *Geophys. Res. Lett.*, 39, L13802.

Murphy, D. M., Froyd, K. D., Schwarz, J. P. and Wilson, J. C. (2013), Observations of the chemical composition of stratospheric aerosol particles, *Q.J.R. Meteorol. Soc.*, doi: 10.1002/qj.2213.

Myhre, G., F. Stordal, K. Restad, and I. S. A. Isaksen (1998), Estimation of the direct radiative forcing due to sulfate and soot aerosols, *Tellus*, 50B,463–477.

Nakajima, T., et al. (2007), Overview of the Atmospheric Brown Cloud East Asian Regional Experiment 2005 and a study of the aerosol direct radiative forcing in East Asia, *J. Geophys. Res.*, 112, D24S91.

Oinas, V., A. A. Lacis, D. Rind, D. T. Shindell, J. E. Hansen (2001), Radiative cooling by stratospheric water vapor: Big differences in GCM results, *Geophys. Res. Lett.*, 28, 14.

Omar, Ali H., et al. (2009), The CALIPSO Automated Aerosol Classification and Lidar Ratio Selection Algorithm, *J. Atmos. Oceanic Technol.*, 26, 1994–2014.

Oshima, N., et al. (2012), Wet removal of black carbon in Asian outflow: Aerosol Radiative Forcing in East Asia (A-FORCE) aircraft campaign, *J. Geophys. Res.*, 117, D03204.

Painter, T. H., M. G. Flanner, G. Kaser, B. Marzeion, R. A. VanCuren, and W. Abdalati (2013), End of the Little Ice Age in the Alps forced by industrial black carbon, *Proc. Natl. Acad. Sci.*, 110, 15216-15221, 10.1073/pnas.1302570110.

Park, M., W. J. Randel, A. Gettelman, S. Massie, J. Jiang (2007), Transport above the Asian summer monsoon anticyclone inferred from Aura Microwave Limb Sounder tracers, *J. Geophys. Res.*, 112, D16309.

Park, M., et al. (2008), Chemical isolation of the Asian monsoon anticyclone observed in Atmospheric Chemistry Experiment (ACE-FTS) data, *Atmos. Chem. Phys.*, 8, 757.

Penner, J. E., C. C. Chuang, and K. Grant (1998), Climate forcing by carbonaceous and sulfate aerosols, *Clim. Dyn.*, 14, 839–851.

Piers M. de F. Forster, K. P. Shine (2002), Assessing the climate impact of trends in stratospheric water vapor, *Geophys. Res. Lett.*, 29, 6

Pruppacher, H.R., J.D., Klett (1978), *Microphysics of Clouds and Precipitation*, D. Reidel, p. 714.

Pueschel, R.F. (1996), Stratospheric aerosols: Formation, properties, effects, *Journal of Aerosol Science*, 27, 3, 383-402, 0021-8502.

Putman, W. M., and S. H. Lin (2007), Finite-volume transport on various cubed-sphere grids, *J. Comput. Phys.*, 227(1), 55–78.

Randel, W. J., F. Wu, H. Vomel, G. E. Nedoluha, and P. Forster (2006), Decreases in stratospheric water vapor after 2001: Links to changes in the tropical tropopause and the Brewer-Dobson circulation, *J. Geophys. Res.*, 111, D12312.

Randel, W. J., et al. (2010), Asian monsoon transport of pollution to the stratosphere, *Science*, 328, 611–613.

Salawitch, R. J., D. K. Weisenstein, L. J. Kovalenko, C. E. Sioris, P. O. Wennberg, K. Chance, M. K. W. Ko, and C. A. McLinden (2005), Sensitivity of ozone to bromine in the lower stratosphere, *Geophys. Res. Lett.*, 32, L05811.

Satheesh, S. K., K. K. Moorthy, S. S. Babu, V. Vinoj, and C. B. S. Dutt, (2008), Climate implications of large warming by elevated aerosol over India, *Geophys. Res. Lett.*, 35, L19809.

Satheesh, S.K., K. Krishna Moorthy, J. Srinivasan (2013), New Directions: Elevated layers of anthropogenic aerosols aggravate stratospheric ozone loss?, *Atmospheric Environment*, 79, 2013, 879-882.

Schoeberl, F., et al. (2006), Overview of the EOS Aura Mission, *IEEE Trans. Geosci.Remote Sens.*, 44, 1066–1074.

Schult, I., J. Feichter, and W. F. Cooke (1997), Effect of black carbon and sulfate aerosols on the global radiation budget, *J. Geophys. Res.*, 102,30,107–30,117.

Schurath, U., K.-H. Naumann (1998), Heterogeneous processes involving atmospheric particulate matter, *Pure Appl. Chem.*, 70, p. 1353

Schwarz, J. P., et al. (2010), Global-scale black carbon profiles observed in the remote atmosphere and compared to models, *Geophys. Res. Lett.*, 37, L18812.

Shindell, D. T. (2001), Climate and ozone response to increased stratospheric water vapor, *Geophys. Res. Lett.*, 28, 1551–1554.

Solomon, S., K. Rosenlof, R. Portmann, J. Daniel, S. Davis, T. Sanford, and G.-K. Plattner (2010), Contributions of stratospheric water vapor to decadal changes in the rate of global warming, *Science*, 327(5970), 1219–1223.

Stocker, T.F., et al. (2013), *Climate Change 2013: The Physical Science Basis*. Chapter 4, Clouds and Aerosols (IPCC, Cambridge Univ. Press, 2013).

Takahashi, H., and Z. J. Luo (2014), Characterizing tropical overshooting deep convection from joint analysis of CloudSat and geostationary satellite observations, *J. Geophys. Res. Atmos.*, 119, 112–121, doi:10.1002/2013JD020972.

Thampi, B.V., et al. (2012), Semitransparent cirrus clouds in the upper troposphere and their contribution to the particulate scattering in the tropical UTLS region, *J. Atmos. Sol. Terr. Phys.*, 74, pp. 1–10

Thomas F. H., et al. (2007), Observations of deep convective influence on stratospheric water vapor and its isotopic composition, *Geophys. Res. Lett.*, 34, 4.

Tilmes, S., R. Müller, R. Salawitch (2008), The sensitivity of polar ozone depletion to proposed geoengineering schemes, *Science*, 320, 1201–1204.

Warren, S., and W. Wiscombe (1980), A model for the spectral albedo of snow. II: Snow containing atmospheric aerosols, *J. Atmos. Sci.*, 37, 2734–2745.

Winker, D. M., et al. (2010), The CALIPSO Mission: A Global 3D View of Aerosols and Clouds, *Bull. Amer. Meteor. Soc.*, 91, 1211–1229.

Uma, K.N., et al. (2012), On the vertical distribution of mean vertical velocities in the convective regions, *Mon Weather Rev.*, 140, pp. 398–410

Vernier, J. P., et al. (2009), Tropical stratospheric aerosol layer from CALIPSO lidar observations, *J. Geophys. Res.*, 114, D00H10, doi:10.1029/2009JD011946.

Warneke, C., et al. (2010), An important contribution to springtime Arctic aerosol from biomass burning in Russia, *Geophys. Res. Lett.*, 37, L01801.

Waters, J. W., et al. (2006), The Earth Observing System Microwave Limb Sounder (EOS MLS) on the Aura satellite, *IEEE Trans. Geosci. Remote Sens.*, 44, 1075–1092.

Zhong W. and J. D. Haigh (2003), Shortwave radiative forcing by stratospheric water vapor, *Geophys. Res. Lett.*, 30, 3.

Zhou, C., J. E. Penner, M. G. Flanner, M. M. Bisiaux, R. Edwards, and J. R. McConnell (2012), Transport of black carbon to polar regions: Sensitivity and forcing by black carbon, *Geophys. Res. Lett.*, 39, L22804.

Chapter 6

Summary and Future work

6.1 Summary

The tropical deep convection has been examined in this study using A-Train satellite data, the state-of-the-art CRM and GCM simulation, in assistance with ECMWF ERA-interim reanalysis. The focus is on how to synergistically use multiple satellite data and on how this could update our current understandings of the tropical deep convection.

The start of this research examines a common issue in satellite remote sensing of cloud, i.e., incorrect collocation of the satellite footprints due to different sensor viewing angles targeting the same elevated object. A case study using CloudSat and MODIS indicates that this issue matters for studying convective clouds with small horizontal sizes, e.g. cumulus. This so-called parallax error is corrected using the method mentioned in Chapter 2 that takes both target elevation and sensor viewing geometries into account.

Generalization of this parallax correction method is applicable to other instruments on different platforms and is demonstrated using two popular combinations of satellite measurements. The method is then applied to satellite measurement of cloud top temperature in the year of 2008. The statistical results of cloud top temperature indicate that parallax correction could significantly improve cloud top temperature estimation and the improvement increases with cloud top height, confirming that parallax correction is important for studies of deep convection.

Cloud top temperature estimation not only relies on correct collocation but also cloud top fuzziness. To account for cloud top fuzziness, the study provides a new method to estimate the physical cloud top temperature by taking advantage of the in-cloud detection ability of CloudSat radar, the high sensitivity to thin cirrus cloud of CALIPSO lidar as well as the state-of-the-art radiative transfer simulation models. The unique combination of CloudSat and CALIPSO provides a complete vertical profile of cloud water content and, moreover, includes thin cirrus clouds that is critical in infrared radiative transfer but is beyond the detection limit of CloudSat alone. A state-of-the-art radiative transfer model, PCRTM, simulates the 11-μm radiative properties of the cloud including brightness temperature and vertical profiles of transmittance from which vertical profiles of optical depths and weighting functions are derived. The level where weighting function peaks is emission level. Chapter 3 proposes an empirical relationship that links the distance between CTH and emission level to the cloud top fuzziness. This relationship indicates a linear relationship between the two variables and independence beyond a threshold. Based on this algorithm, brightness temperature simulation perfectly matches collocated MODIS measurement. This result significantly contributes to studies

of cloud top features. The reasons are (1) previous studies using passive remote techniques only are not capable to distinguish active and dissipating convection and this study demonstrates the necessity of taking convective development phase into considerable; (2) previous parameterization of cloud top emission level in the infrared band is linearly converted from that in the visible band and this study directly calculates the radiative properties in the infrared band.

Based on the techniques in Chapter 2 and 3, cloud top temperature is derived and then interpreted in more physically meaningful variable – cloud top buoyancy. Cloud top buoyancy indicates the phase of convective development with large positive value in developing phase and negative value in dissipating phase. The global distribution of cloud top buoyancy is studied with respect to land and ocean, measurement time, cumulus congestus and deep convection. We conclude that convective cases are more frequent over land at 1:30pm and over ocean at 1:30am, that cumulus congestus is sensitive to both land-ocean contrast and diurnal difference and deep convection show strong diurnal difference over both land and ocean. Under the fountain-cloud assumption, the vertical profile of cloud top buoyancy is interpreted as buoyancy profile of a rising air parcel. The vertical velocity of the imaginary air parcel is then derived. The calculation agrees with direct vertical velocity observation in the value and altitude of peak velocity and the existence of a weak detrainment layer around mid-troposphere.

Strong deep convection is able to overshoot through tropopause and thus transport aerosols such as black carbon into the lower stratosphere. Recently, this topic has been given a lot of attention due to the potentially strong destructive effect of black carbon to stratospheric ozone. The study shows that the transportation event is most prominent over

India during summer Asian monsoon, because of highly polluted lower troposphere and large-scale ascent that favors deep convection. This study suggests the potential major role of overshooting deep convection in transporting black carbon across the tropopause using a state-of-the-art GCM model simulation. To directly measure such process, an infrared limb-viewing method is proposed to measure black carbon concentration at 16.6 km. The radiance at the most transparent wavenumber in IR window channel, 940 cm^{-1}, is used to capture the signal from black carbon. In this radiance profile, the contribution of radiance from water vapor is minimized by normalization using the radiance profile at 1210 cm^{-1} which is sensitive to water vapor continuum only. The signal of black carbon thus stands out as the radiance signal of water vapor varies proportionally in both wave numbers. The study shows that the ratio of radiance linearly correlates to the black carbon concentration at 16.6 km. The study also shows that the large-scale condition influences the method in a linear manner and is taken into consideration through a look-up table.

6.2 Future work

The parallax correction significantly improves the accuracy in deep convection study even for those satellites flying in close formation. This correction method will be useful given current acknowledgement of satellite synergy and future satellite constellations like A-Train. Besides, parallax may be useful in the cloud remote sensing. For example, we noticed that 11-μm brightness temperatures of the same cloud top but of different viewing zenith angles could strongly resemble the idealized arc of the split-window method (Figure 3 in *Stephens and Christian* [2007] and the references therein) and thus could be useful to the measurement of cloud top particle size. Because this

method is of only one frequency, the potential benefit of this method is its wide applicability on geostationary satellites which all have 11-μm channel with fine horizontal resolution of 1 km. The physical reasoning is that the measured brightness temperature depends on the optical depths of cloud that is the product of absorbing mass density and mass extinction coefficient and distance along the viewing path. Splitting window method uses two near wavelengths, i.e. 10.8 and 12 μm, with different extinction coefficient. The parallax method uses only 11-μm brightness temperatures and takes advantage of different viewing distance, which is theoretically equivalent to the conceptual idea of the split-window method since the effect of extinction coefficient and distance of calculation is inseparable. Further quantitative analyses are needed to strictly establish the relationship and to use geostationary satellite data to derive cloud top microphysics. MODIS measurement would provide valuable dataset for algorithm verification.

The understanding drawn on cloud top buoyancy is mostly at the theoretical level. Rigorous validation is necessary using direct observations. Possible datasets that can be used for such purposes include, but are not limited to, continuous ARM ground radar observations that keep track of the vertical development of convection, field campaigns that measure convective vertical velocity as well as its thermodynamic features, geostationary imagery with high temporal resolution in the infrared window channel, and multi-angle imaging spectroradiometer (MISR) measurements which observe the same cloud from different angles within a short time period.

The BC retrieval method in Chapter 5 is based a linear correlation between BC in the lower stratosphere and the ratio of two radiance profiles. Tested using model

simulation as surrogate of real atmosphere, this method consistently captures the seasonal cycle and responds well to large BC concentrations. However, this method shows insufficient performance in capturing all the variability of the black carbon concentration change, which possibly results from the simplification of the problem at the preliminary phase of the study. Further research is needed to test the applicability of the method and to refine the method. The conclusion drawn on GFDL AM3 model will be further tested using other global climate models especially those with full-fledged chemistry module.

Reference:

Stephens, G. L., Christian D. K. (2007), The Remote Sensing of Clouds and Precipitation from Space: A Review, *J. Atmos. Sci.*, 64, 3742–3765.